LIQUID METAL DEALLOYING IN MULTICOMPONENT SYSTEMS – TOWARDS NEXT-GENERATION METAL COMPOSITES

by
Bernard Gaskey

A dissertation submitted to Johns Hopkins University in conformity with the
requirements for the degree of Doctor of Philosophy

Baltimore, Maryland
May 2018

Abstract

Liquid metal dealloying (LMD) is an emerging process for making metal composites and porous metal materials by selectively dissolving components of a parent alloy in a bath of a dissimilar metallic melt. As some fraction of the parent alloy dissolves into the liquid, the remaining solid components can be selected such that they rearrange, forming a complex structure and allowing dissolution to continue. This leads to the formation of a porous network of the solid component, with the empty space filled by solidified liquid in the final composite. Subsequently removing one phase by chemical etching reveals a porous metal structure.

In this thesis, the mechanisms of LMD and the interaction between processing methods, structural geometry, and length scale are studied in detail. We show that the thermodynamic driving force for LMD can be carefully tuned to select the final structure of the solid network that forms by changing the composition of the molten metal bath. We analyze the kinetics of the LMD process to quantify the rate of dealloying and the rate that features coarsen post-dealloying. Applying fundamental insights gained from these results, we design a dealloying system where a chemical reaction in the liquid metal forms an additional intermetallic phase within the porous network during dealloying. Finally, we present a method for making dealloyed metal coatings with superior hardness on a nickel alloy substrate, where eutectic melting at the interface between coating and substrate leads to a dealloying reaction that strengthens both materials.

Porous metals and composites made by LMD are promising for a range of applications due to the wide range of chemistries and morphologies available. This thesis seeks to address the gap in fundamental understanding of LMD mechanisms to rapidly advance the discovery, study, and application of a new generation of functional metal composites.

Advisor: Prof. Jonah Erlebacher

Readers: Prof. Jonah Erlebacher, Prof. Mingwei Chen

Acknowledgements

Many people contributed directly to the research detailed here, and to other work that was not included in this thesis. I hope they know who they are. First, I would like to recognize the contributions of everyone in the Erlebacher group during my time as a PhD student. Ian McCue began and continues to contribute to our study of liquid metal dealloying. Prof. Alain Karma and his students Dr. Pierre-Antoine Geslin and Longhai Lai provided phase field simulations of dealloying. Alyssa Chuang, Aliya Carter, and Bijan Varjavand performed some alloy preparation and liquid metal dealloying experiments. Bijan Varjavand wrote and maintained image processing code to determine ligament sizes. Bryan Crawford performed nanoindentation experiments and other mechanical testing. Plasma spray powder was provided by Oerlikon Metco and plasma spray equipment from JHU Applied Physics Lab was used for coating preparation. This experiment would not have been feasible without help from Dr. Michael Brupbacher and Mark Buchta. Dr. Thomas Brooks provided important insight for image processing code to analyze ligament shapes. Niobium capacitors were fabricated and tested by Alyssa Chuang. All of this work has been ably supported by the staff and faculty of the Materials Science department at Johns Hopkins.

I would like to acknowledge the financial support that enabled this research provided by the National Science Foundation Division of Materials Research through award number 1402726 and the Department of Energy via award DE-SC0008686.

Table of Contents

List of Table

List of Figures

1 Introduction

Dealloying is a process of selective corrosion of one or more atomic components of an alloy, leaving the remaining components behind. It can be used as a processing tool to form porous structures by careful selection of the starting alloy and processing parameters. Dealloyed materials and the mechanisms of dealloying have been studied for several decades, where the dealloying process is performed by dissolution of a less-noble component metal of an alloy in an aqueous electrolyte either by chemical corrosion or by application of an electrical potential. More recently, the field has been generalized by the discovery of liquid metal dealloying (LMD) wherein a molten metal bath replaces the aqueous dealloying medium. LMD has some advantages over conventional electrochemical dealloying that make it a promising technique for the fabrication of new porous metal materials and metal composites with a wide range of potential compositions, properties, and applications.

LMD still has several hurdles to overcome before it is a commercially viable processing technique. This thesis aims to address several of these hurdles, first by providing a theoretical basis for the unique mechanisms microstructure evolution during LMD, and then by applying this understanding to develop several new classes of LMD materials with a range of interesting properties.

The remainder of this introductory chapter will discuss the development and mechanistic understanding of electrochemical dealloying, including details of morphology formation during dealloying and structural coarsening that occurs in dealloyed materials. It will then discuss significant differences between electrochemical dealloying and LMD.

Chapter 2 provides a detailed introduction to the LMD technique, focusing on experimental techniques used to fabricate the materials used throughout this work. Using titanium tantalum binary alloys dealloyed in a copper melt, this chapter describes the kinetics of the LMD process, which are found to be governed primarily by liquid phase diffusion. LMD can form a greater variety of morphologies than electrochemical dealloying based on the selection of the starting alloy, and this phenomenon is related to the composition of the starting alloy.

In Chapter 3, the tunability of morphological evolution during LMD is extended by addition of a second element to the molten metal bath. Without this addition, the morphology of the LMD microstructure depended only on the composition of the starting alloy. Changing the bath composition provides a new way to access interesting structures with a greater variety of starting alloys. Particularly, connected bicontinuous structures can be formed from a much wider range of binary alloy compositions than was previously possible.

Chapter 4 analyzes coarsening of dealloyed niobium-titanium-silicon materials in detail. All dealloyed materials coarsen after formation because of the high surface energy associated with the large exposed surface area of the ligaments. In LMD, this is complicated by the nature of dissolution in molten metals. In particular, ligaments can coarsen either by surface diffusion of the solid species, or by diffusion of a small fraction of the same species dissolving in the molten metal, which causes rapid coarsening during the dealloying process and leads to a different distribution of ligament sizes in the final sample.

In Chapter 5, three-phase composites containing an additional intermetallic compound are formed in a single step by LMD of niobium-titanium-silicon ternary alloys in molten Cu in such a way that niobium silicide precipitates simultaneously form in the porous structure along with the more usual bicontinuous morphology. Previously, porous metals formed by LMD were susceptible to detached grain boundaries that cause the structure to fall apart, but in this case removing the copper phase leaves a porous composite where the silicide crystals reinforce the grain boundaries to make structurally robust polycrystalline porous Nb.

Chapter 6 looks at the role of LMD in forming hard coatings on nickel alloys. The coatings are formed by depositing an alloy layer on the surface of a Ni-alloy substrate such that, upon heating, a dealloying reaction takes place driven by eutectic melting at the interface between the two dissimilar alloys. The resulting liquid drives phase separation both in the substrate and precursor coating to form a final dealloyed region with constituent elements from both alloys, but possessing much higher hardness than either the substrate or precursor coating.

To conclude this thesis, Chapter 7 describes some promising new LMD material systems including porous Si, possible applications for the porous Nb composites described in Chapter 5, and a method to apply the coating technique from Chapter 6 to form additively manufactured composite parts. It ends with some thoughts about the progress made in this work and the outlook for the future of LMD.

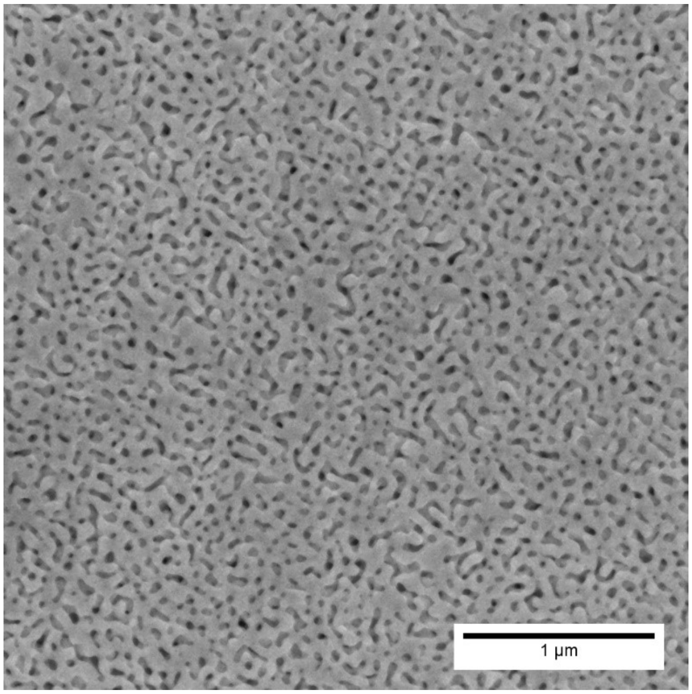

Figure 1-1: A scanning electron micrograph of a nanoporous gold (np-Au) surface made by dealloying $Ag_{65}Au_{35}$ alloy in nitric acid.

1.1 Electrochemical Dealloying

The concept of dealloying has been well known for more than a century but, in the context of corrosion, has been regarded primarily as a materials phenomenon to be avoided. Dezincification of brasses had been studied as early as the Civil War period [1], and even subtle effects like the addition of 1% Sn to Cu/Zn brasses (admiralty brasses) were well characterized. By the late 1960s, the mechanism behind dezincification was under study, with Pickering [2] first performing rigorous mechanistic studies on Au-based alloy systems. In the 1970s, Forty [3] used advances in electron microscopy to provide the first detailed look at the microstructures formed by the dealloying process. The seminal work by these two researchers led to the modern study of dealloying as a platform for materials processing.

Dealloyed materials are often prototyped by nanoporous gold (np-Au), which is fabricated by the dissolution of Ag from Ag-rich Ag-Au alloys, but many other alloy systems have been the subject of intense study (**Figure 1-1**). Of particular relevance, high-surface-area precious metal catalysts such as np-Pt are finding applicability for a wide range of reactions and are being actively integrated into cutting-edge devices such as low Pt-loading fuel cells. Studies motivating the Materials Genome Initiative suggest that the typical time period between the discovery of a new materials and its entrance into the marketplace is approximately 20 years (see http://www.mgi.gov). It is interesting from our perspective that the first paper elucidating the correct fundamental model for porosity evolution and advocating for the utility of dealloyed nanoporous metals in functional applications was published approximately 17 years ago [4]. Significant advances have been made on dealloyed materials since 2001 by an ever-growing international community of researchers, and we expect that nanoporous metals will find their way into the marketplace in the very near future. The field of dealloying and dealloyed materials has grown quite large. A review of the field, including historical perspectives that touch on pre-Columbian archaeology [5] and early concepts of surface thermodynamics [6], can be found in Reference [7].

The working model of porosity evolution has been introduced elsewhere [8] and is briefly summarized here. The primary driving force is that, at electrochemical potentials above a composition-dependent critical potential V_C, dissolvable atoms are easily solvated and removed from low-coordination sites such as step edges [9], and these surface sites are rapidly passivated with the remaining more noble species. Thus, the rate-limiting step of nanoporosity evolution is the dissolution of an atom from a high-coordination site such as a terrace [10], which leads to the creation of a terrace vacancy that then grows laterally into a vacancy cluster as near neighbors are subsequently dissolved. The more noble, nondissolving species tend to diffuse with the receding step edge rather than be left as thermodynamically unfavorable adatoms [9], a kind of interfacial uphill diffusion (adatoms moving from low-concentration areas to high-concentration areas) mathematically describable by Cahn-Hilliard diffusion kinetics usually associated with spinodal decomposition. This effect is assisted by the rapid surface diffusion of noble metals in aqueous environments containing common anions [11], [12]. The temperature dependence of the dissolution currents has been measured for np-Au in ionic liquids, and the activation barrier associated with dealloying corresponds well in magnitude to dissolution from terrace sites [10].

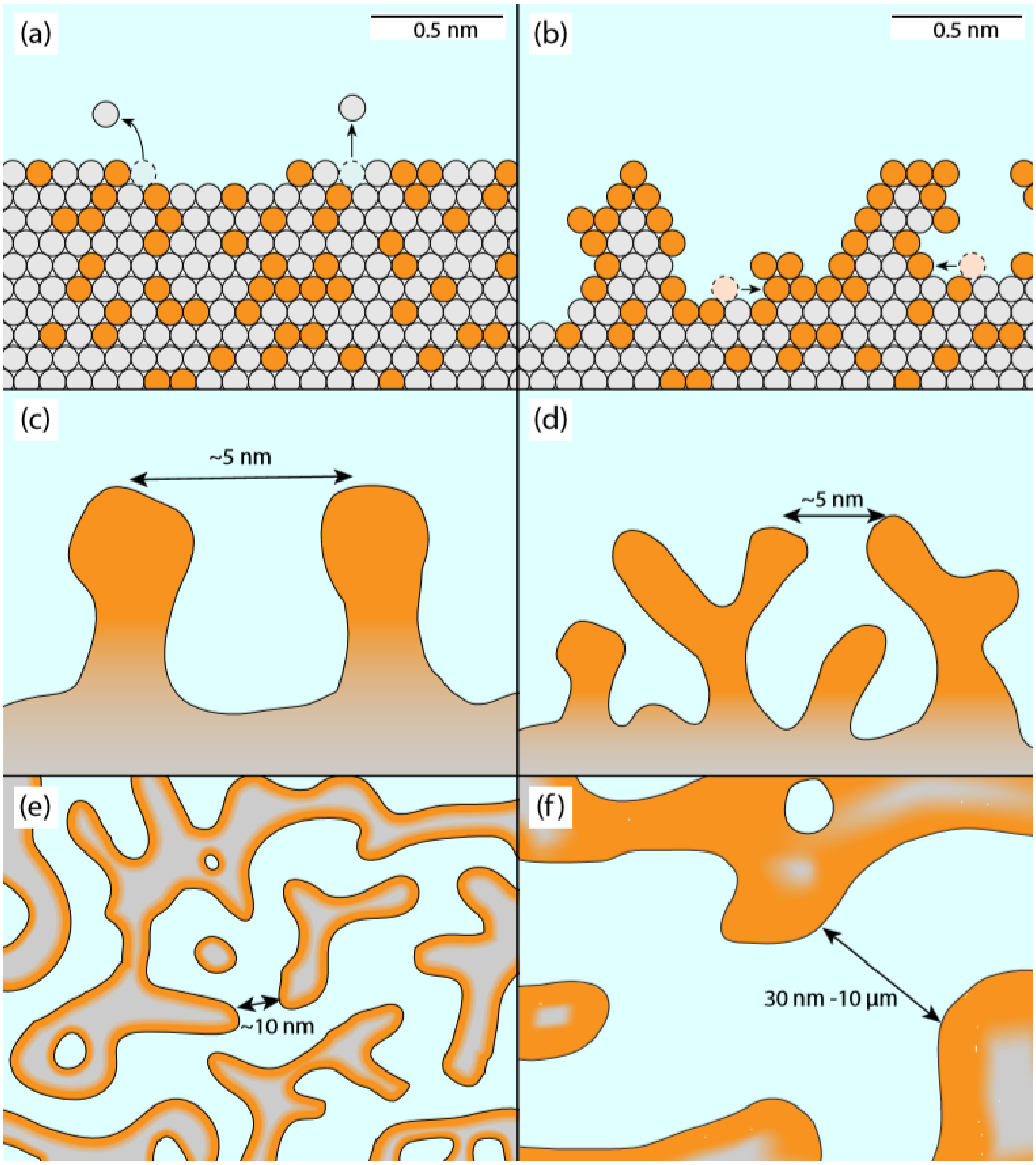

Figure 1-2: Working model for porosity evolution in dealloying in the Ag-Au alloy system (Ag, gray; Au, orange). (a) The rate-limiting step is the formation of terrace vacancies, which then grow into lateral vacancy clusters. (b) As dissolution proceeds layer by layer, surface diffusion passivates low-coordination sites with Au, leading to surface roughening. (c, d) As dealloying continues, there is insufficient Au to totally passivate the increasing surface area, leading to undercutting and bifurcation of ligaments. (e) The result of this process is a bicontinuous porous structure in which ligaments have Au-rich surfaces and Ag-rich interiors. (f) As coarsening increases the length scale of the initial structure, residual Ag atoms are exposed and dissolved, leaving a final structure with much reduced Ag content.

As the dealloying process continues, new atoms of the dissolving species are exposed to the electrolyte around the base of the noble metal clusters formed during earlier dissolution and surface rearrangement. However, the noble metal–passivated mounds have base perimeters that grow in diameter as dealloying proceeds. Eventually, not enough noble metals atoms are provided to passivate them effectively, allowing them to be undercut. This process bifurcates the pores, leading to an increase in the surface area and allowing porosity evolution to proceed into the bulk of the precursor alloy. This process is outlined schematically in **Figure 1-2**. One might predict that, at some point, transport of dissolved cations out of the porous layer would become rate limiting. However, in practice, this diffusion rate is nearly ten orders of magnitude faster than interface diffusion and electrolyte diffusion has never been observed to be rate limiting.

Historically, the description of dealloying has been characterized by two parameters: the parting limit X_P, defined as the fraction of the dissolving species below which dealloying does not proceed, and V_C, below which interface mass transport is much faster than the dissolution rate. X_P and V_C were defined early in the development of dealloying theory [13], but the understanding of both concepts has been refined in the last decade.

Sieradzki et al. [14] were the first to connect X_P to geometric percolation of the nonnoble atoms through the bulk of the material in the dealloying of Ag-Au. To dealloy a material, there is a geometric minimum criterion requiring the nonnoble atoms to be connected. For Ag-Au, a face centered cubic alloy, the percolation threshold is approximately 19-at% Ag, but in practice X_P is approximately 55-at% Ag. A more nuanced geometric interpretation was recently introduced by Newman and coworkers, wherein the percolation pathway of nonnoble atoms must be sufficiently wide to solvate a dissolving atom with anions [15]. This high-density percolation idea predicts an X_P of ~60-at% Ag, quite close to that seen experimentally. V_C, originally a purely empirical construct, is typically defined as the potential for which the dissolution current rises above a specific (low) value. The structural implication is that below V_C there is interlayer transport of noble metal atoms, allowing them to passivate the surface. This transport is a consequence of capillary forces acting to smoothen the surface more rapidly than the dealloying process roughens it. A function of alloy composition, V_C typically decreases with decreasing nonnoble composition. However, as the composition varies toward 100% nonnoble composition, V_C does not converge to the reversible dissolution potential for that element, as would be expected, and is instead typically a few hundred millivolts higher [16].

1.2 Coarsening

Nanoporous metals are always thermodynamically metastable because of their large surface areas. Thus, in an environment in which surface atoms are sufficiently mobile, the length scale of porosity tends to increase over time as atoms move from smaller to larger ligaments. One challenge associated with the utilization of nanoporous metals in engineering applications is their propensity to coarsen in the application environments, greatly limiting their usable lifetimes. However, although coarsening is an

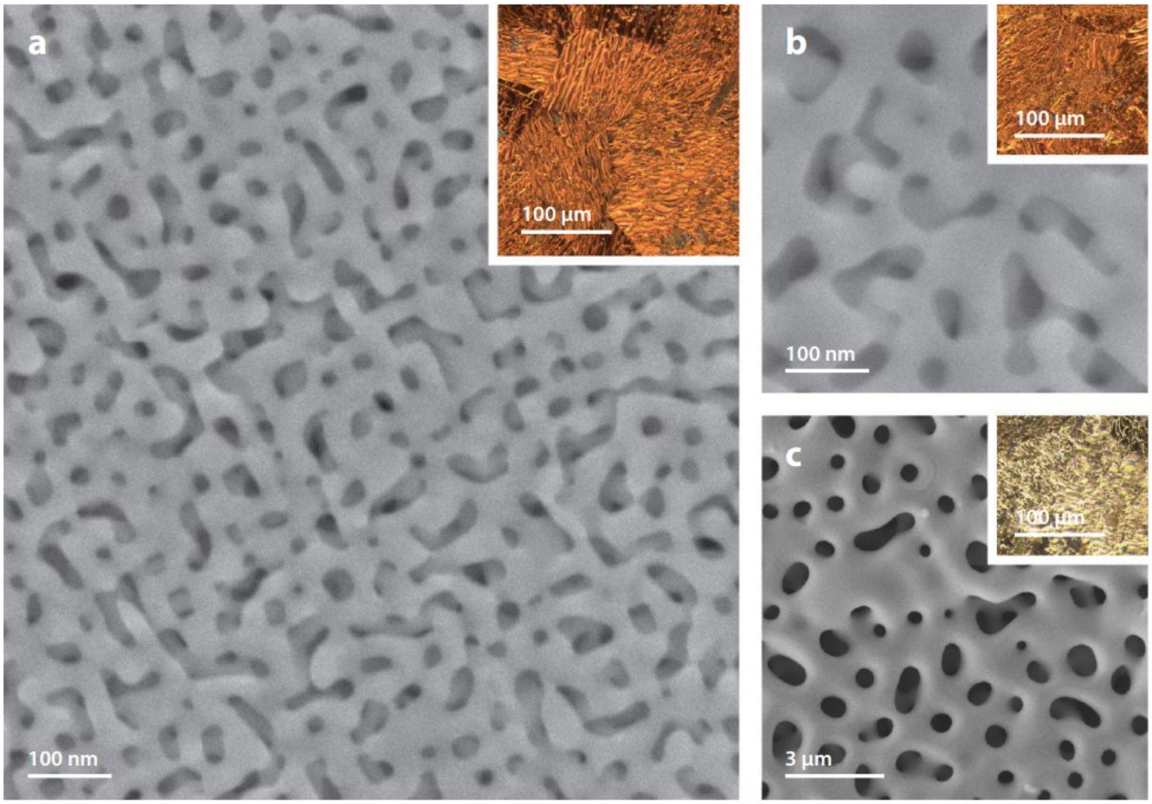

Figure 1-3: SEM and optical micrographs (inset) of nanoporous Au formed by free corrosion dealloying of a homogeneous $Ag_{65}Au_{35}$ alloy in concentrated nitric acid. After initial dealloying for 24 h, the system exhibits ∼30-nm features (a), which coarsen to ∼60 nm after an additional 100 h in nitric acid (b) or to several micrometers after heating to 800◦C for 10 min in air (c).

important challenge to overcome, it can also be a powerful processing tool for controlling ligament size (see **Figure 1-3**). At elevated temperatures, the pore/ligament size can be controlled to grow to tens of micrometers while maintaining the characteristic bicontinuous structure [17]. In an electrolyte, the surface diffusion rate is controlled by the anion species in the solution, with significant coarsening rates observable even at room temperature [18]. The observed structure of a dealloyed material is generally coarser than its intrinsic length scale. Kinetic Monte Carlo (KMC) simulations predict an initial length scale of porosity of approximately 2–3 nm [9], and such small-scale porosity is seen in np-Au during dealloying at subzero temperatures [19] and in lower-mobility alloys such as np-NiPt. However, there is always some coarsening concurrent with the dealloying process, resulting in typical np-Au dealloyed in nitric acid at room temperature having ~30-nm ligaments [8], [20].

Coarsening of nanoporous metals is driven by thermodynamic surface energy reduction, in analogy to sintering [19], [21]. However, unlike sintered structures, the dealloyed structure is a single crystal (within each grain), which imparts unique geometric features to nanoporous metals. Specifically, these metals possess regions of positive, negative, and saddle point curvature in a topologically complex network. Such complex topologies have been of significant recent interest [22]–[26], and methods have been developed to describe the topology of nanoporous metals [27], [28], and the dynamics of topology evolution have been studied by KMC and molecular dynamics (MD) [29], [30]. The results of these studies indicate that structure evolution tends to proceed via pinch-off Rayleigh instabilities that reduce the local genus (the number of handles in the structure). One implication is that inverse Rayleigh instabilities—a tunnel breaking up into a series of voids—can also occur, and such instabilities in turn explain the TEM observations of large voids within the ligaments of np-Au reported in Reference [31]. To control and slow secondary coarsening, the best method developed to date has been to add a slowly moving noble third component to the precursor alloy. For instance, Snyder and coworkers [32], Vega & Newman [33], and Jin and coworkers [20] employed this strategy by adding Pt to an Au-Ag alloy prior to dealloying. Not only does this addition initially refine the pore size to less than 4 nm, but it also adds stability in acidic conditions. The mechanism proposed for this effect is the segregation of Pt to step edges during dealloying along with Au, as in the working model. However, the lower surface mobility of Pt causes it to pin step edges, making them immobile and thus hindering coarsening. Via this expedient, np-Au/Pt is virtually inert to electrochemical annealing (on the scale of days) in acid compared with np-Au.

1.3 Dealloyed Materials

One reason for the growing popularity of studying dealloyed nanoporous metals is that they are very easy to make. A homogeneous alloy precursor of whatever shape is simply immersed into an acid that selectively dissolves one component away. As long as the remaining component is free to diffuse along the acid/alloy interface, porosity generally forms.

Depending on the desired form factor, certain tricks have been developed by the dealloying community, with the majority developed for np-Au dealloyed from Ag-Au precursors. For instance, large, monolithic samples of np-Au require good homogenization prior to dealloying and require slow drying to avoid mud cracking [17], [20]. Thin films of np-Au can be made by dealloying hammered alloy leaf [18] but can also be made from vapor-deposited thin films, whereby galvanostatic dealloying (constant dissolution current rather than fixed dissolution potential) leads to the abatement of thin-film stresses that lead to cracking [34], [35]. Such thin films are finding utility in a variety of sensor applications [36], [37].

One of the cleverest synthetic routes to control nanoporosity was reported by Qi &Weissmuller [38], who demonstrated a method to make np-Au monoliths with hierarchical porosity. The process employs all the fundamental principles of the working model. A relatively dilute Au alloy is first dealloyed at a potential just above V_C and annealed. This process results in a material with relatively large-scale porosity and ligaments that retain a significant amount of Ag such that a second dealloying step can dealloy the large ligaments, forming a second, much smaller scale of porosity. This method is a significant improvement over an anneal/backfill/anneal/redealloy method developed earlier to create multiscale np-Au [39]. Another method to create hierarchical nanoporous metals is deposition of the precursor alloy into templates, such as colloidal particles [40].

Another useful form factor of nanoporous metals is melt-spun ribbons. For instance, np-Ni and np-Cu have been fabricated from melt-spun alloys with Mn, following recipes developed by Hakamada et al. [41] and Chen et al. [42]. An aspect of these melt-spun materials that has not received sufficient attention in our opinion is the size of the crystalline domains in the precursor material. Porosity, as discussed, generally forms on a scale much smaller than the grain size. However, grains are often very small in melt-spun materials, so one must be careful that the nanoporous product is not more similar to a sintered agglomerate of nanoparticles. This idea was recently addressed in a study comparing np-Au made from crystalline precursors and np-Au made from amorphous precursors [43], [44]. Crystalline precursors exhibit the usual lack of grain boundaries within the porous network, but the amorphous material is clearly a nanogranular aggregate. Presumably, for the amorphous precursor, local clusters of Au that form in the initial stages of dissolution are not required to have any crystallographic registry with each other, but how the domains interact during the later stages of dealloying is unknown. How an amorphous precursor affects the ultimate properties of the material made from them remains another unanswered question, but there have been

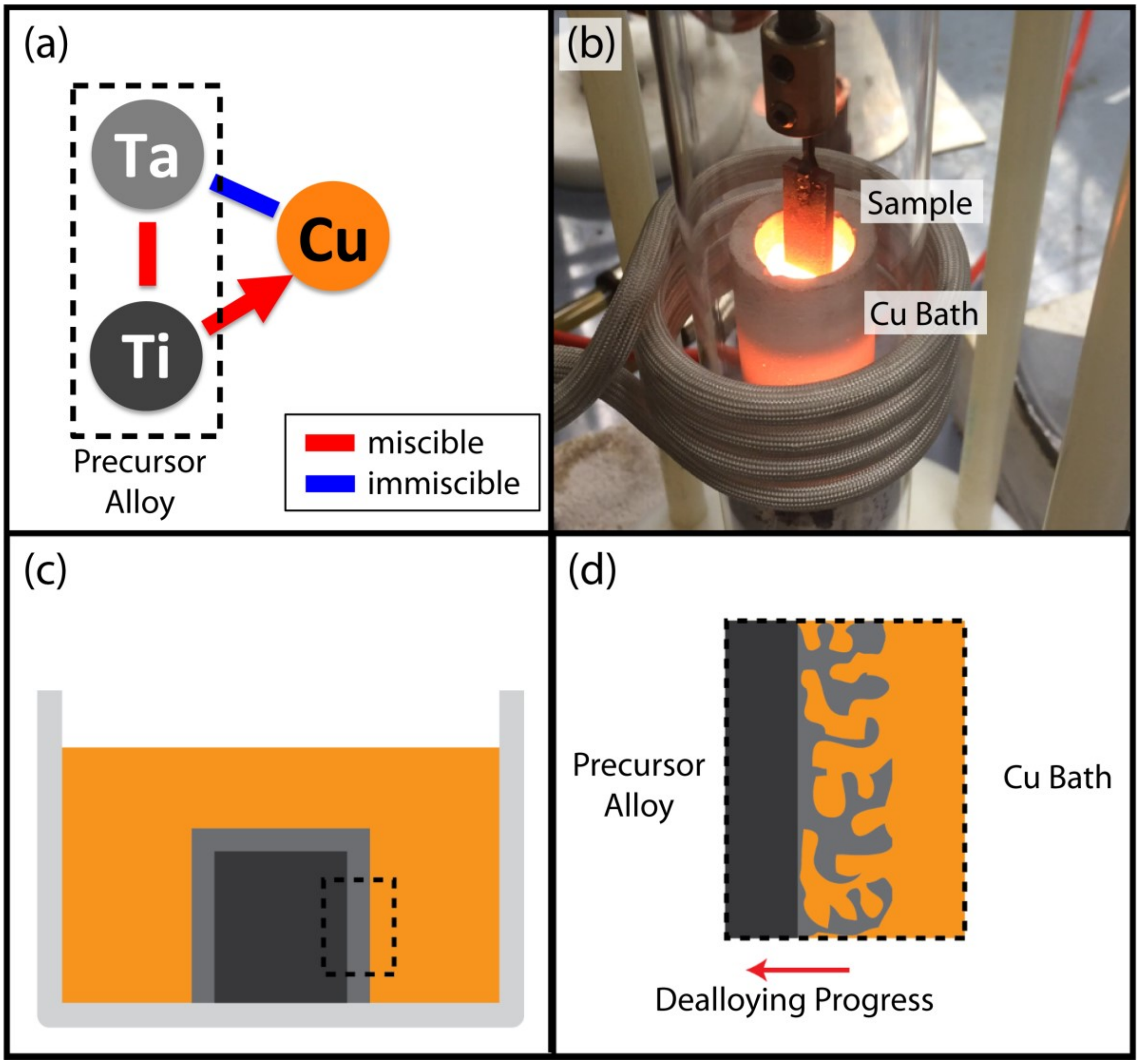

Figure 1-4: (a) A binary alloy of Ti and Ta can be dealloyed in molten Cu, where Ti dissolves and Ta and Cu are immiscible. (b) A sample suspended from a manipulator arm being immersed in a Cu bath heated by induction melting. (c-d) A schematic of how porosity forms from the surface of a sample during LMD where the sample is resting at the bottom of the metal bath. Note that the experiment in (b) is performed by dipping the suspended sample such that all the surfaces of the sample dealloy simultaneously.

many recent studies using metallic glass precursors [45], so an answer to this question is hopefully forthcoming.

The effect of crystallographic order on dealloying is also quite interesting. Early studies of dealloying compared precursors made of Cu_3Au, which can be prepared either in a disordered solid solution (with the atoms randomly organized) or as an intermetallic compound with long-range order in an ordered state with the the L_{12} structure [46]. The key result is that ordered alloys exhibited a higher V_C than did disordered alloys, reflective of a higher average bond enthalpy, a structural feature that may affect catalytic activity for CO oxidation [47].

1.4 Liquid Metal Dealloying

Liquid metal dealloying shares many characteristics with electrochemical dealloying. Both processes are caused by dissimilar driving forces for dissolution in the component metals of an alloy. LMD was first demonstrated by Wada et al. in 2011, when they formed porous titanium by immersion of titanium-copper alloys in a magnesium melt [48]. Since then, several other LMD systems have been identified and the kinetics of the process, structure of the resulting material, and mechanical properties have been studied in detail. To describe general characteristics of LMD, we compare the prototypical gold-silver dealloying system with the tantalum-titanium LMD system where copper is the liquid metal bath (**Figure 1-4**). In this case, Ti has a large solubility in molten Cu across a wide range of temperatures, whereas Ta has virtually no solubility over a similar range (**Figure 1-5**). If a Ta-Ti binary alloy is dipped in molten Cu within this temperature regime, there is a much greater driving force for Ti to dissolve than Ta. This is analogous to the dissolution of silver but not gold in the potential range between the reduction potentials of the two metals. In the silver-gold case, removal of the sample from the electrolyte after dealloying will directly yield a fully formed porous structure. In

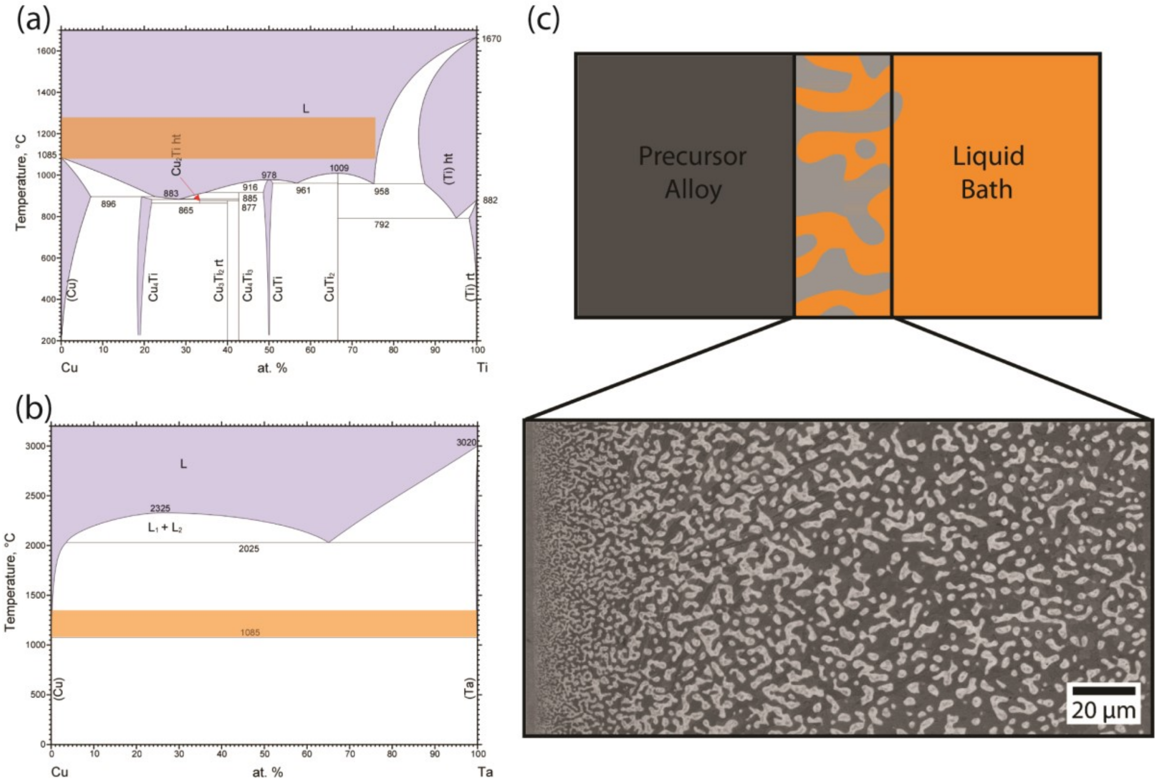

Figure 1-5: Binary alloy phase diagrams for the Cu-Ti system (a) and the Cu-Ta system (b) with the temperature range used in LMD highlighted in orange. Ti is very soluble in Cu, while Ta is almost perfectly insoluble over the temperature range used (purple areas of the phase diagram denote mixing). Immersing a Ti-Ta binary alloy in Cu results in the dissolution of the Ti (c), which can leave a porous network of Ta ligaments and pores filled with Cu that solidifies when the sample cools after LMD.

LMD, however, Cu solidifies in the void space left by the dissolution of Ti during the rapid cooling as the sample is removed from the Cu bath. The sample is initially a fully dense metal-metal composite material with the tantalum ligament structure buried in copper containing varying amounts of residual titanium, as shown in **Figure 1-5**. To observe the porous Ta network directly, the other phase must be removed. That is easily accomplished by etching the Cu phase away in nitric acid or similar, where the Ta forms a passive oxide that protects that phase from dissolution. **Figure 1-6** shows the resulting porous Ta network after the Cu phase is etched away, with a similar structure to the

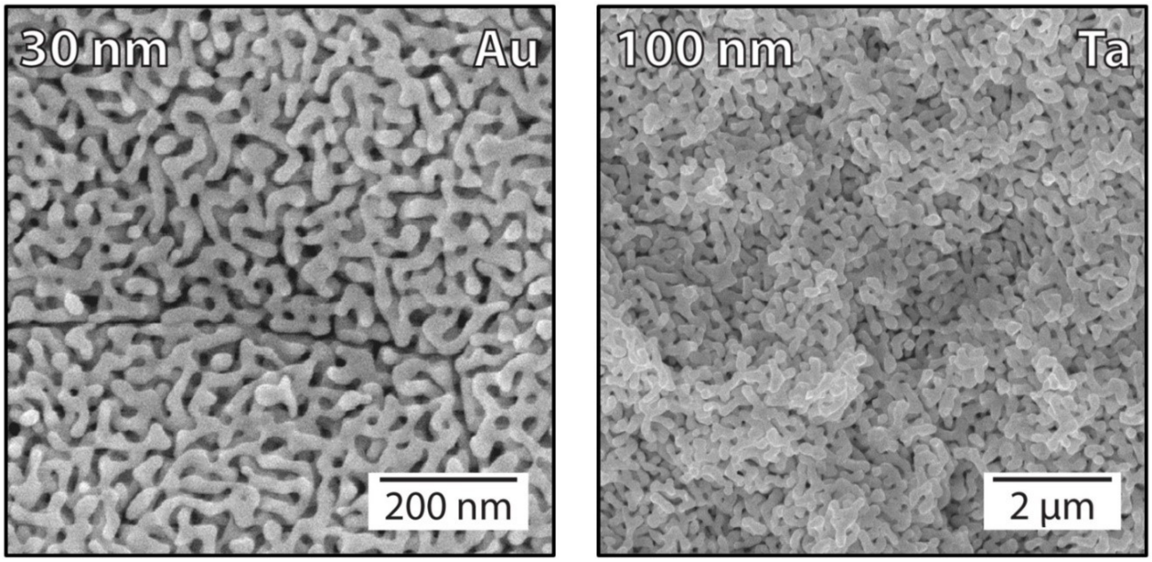

Figure 1-6: A comparison of the porous morphologies formed by dealloying $Au_{35}Ag_{65}$ electrochemically in nitric acid (left) and liquid metal dealloying $Ta_{35}Ti_{65}$ in molten Cu (right).

surface of nanoporous gold. As will be shown later, the concepts of critical potential and parting limit are somewhat less clear in LMD. While electrochemical dealloying will form a bicontinuous porous structure almost any time that it functions, LMD has a gradient of possible structures depending on the kinetic details of the reaction. Similarly, there is no specific driving force where LMD “turns on” like the critical potential; there is always some dissolution of each component when an alloy is placed in contact with a metallic melt, and as the dissolution rates of the components diverge, increasingly complex microstructures can evolve.

LMD is an important addition to the wider field of dealloying because it provides a new set of material systems to study compared to electrochemical dealloying. In the 15 years that electrochemical dealloying has been studied as a material processing technique, a variety of porous metals have been studied (highlighted in **Figure 1-7**), but there are limitations on what metals are available aqueous electrolytes. Precious metals, including

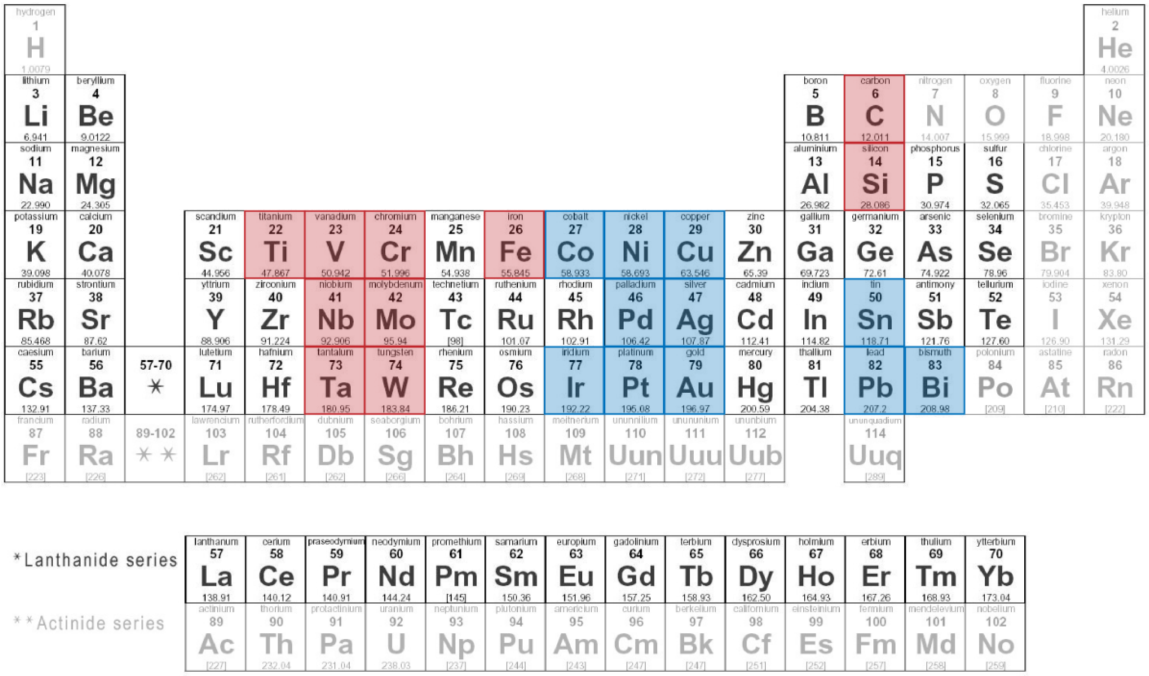

Figure 1-7: The periodic table of elements, highlighting those that can be made porous electrochemically (blue) and those that have been made porous by LMD (red).

gold and platinum, are easily handled and the electrochemistry of precious metals is well studied, but many other metals rapidly oxidize or corrode in water. By introducing LMD with a wide range of available metal “solvents”, many new porous metals can be studied. The number of elemental systems available to LMD is already approaching the total that have been dealloyed electrochemically, and many more LMD systems remain available for identification and study. LMD is not yet a process that promises to solve a particular problem, or provide a material for a specific application, but by expanding the scope of LMD and understanding the underlying processes that drive microstructure evolution during LMD, materials can be designed for a range of applications.

1.5 References

[1] C. Calvert and R. Johnson, “XLI.—Action of acids upon metals and alloys,” *J. Chem. Soc.*, vol. 19, no. 0, pp. 434–454, 1866.

[2] H. W. Pickering, “Volume Diffusion During Anodic Dissolution of a Binary Alloy,” *Journal of the Electrochemical Society*, vol. 115, no. 2. pp. 143–147, 1968.

[3] A. J. Forty, “Corrosion micromorphology of noble metal alloys and depletion gilding [5],” *Nature*, vol. 282, no. 5739. pp. 597–598, 1979.

[4] J. Erlebacher, M. J. Aziz, a Karma, N. Dimitrov, and K. Sieradzki, “Evolution of nanoporosity in dealloying.,” *Nature*, vol. 410, no. 6827, pp. 450–453, 2001.

[5] H. Lechtman, “Pre-Columbian surface metallurgy,” *Sci. Am.*, vol. 250, no. 6, pp. 56–63154, 1984.

[6] V. G. Masing, “On the theory of resistance limits in mixed crystals,” *Anorg. Allg. Chem*, vol. 118, no. 1, pp. 293–308, 1921.

[7] A. Wittstock, J. Biener, J. Erlebacher, and M. Baumer, Eds., *Nanoporous Gold*. The Royal Society of Chemistry, 2012.

[8] J. Erlebacher and R. Seshadri, “Hard Materials with Tunable Porosity,” *MRS Bull.*, vol. 34, no. 8, pp. 561–568, 2009.

[9] J. Erlebacher, “An Atomistic Description of Dealloying,” *J. Electrochem. Soc.*, vol. 151, no. 10, p. C614, 2004.

[10] J. Snyder and J. Erlebacher, “Kinetics of Crystal Etching Limited by Terrace Dissolution,” *J. Electrochem. Soc.*, vol. 157, no. 12, p. S21, 2010.

[11] M. J. Rost, R. Van Gastel, and J. W. M. Frenken, “Anomalous Shape and Decay of

Islands on Au(110),” *Phys. Rev. Lett.*, vol. 84, no. 9, pp. 1966–1969, 2000.

[12] J. M. Dona and J. Gonzalez-Velasco, “Mechanism of surface diffusion of gold adatoms in contact with an electrolytic solution,” *J. Phys. Chem.*, vol. 97, no. 18, pp. 4714–4719, 1993.

[13] H. W. Pickering and P. J. Byrne, “On Preferential Anodic Dissolution of Alloys in the Low-Current Region and the Nature of the Critical Potential,” *J. Electrochem. Soc.*, vol. 118, no. 2, p. 209, 1971.

[14] K. Sieradzki, R. R. Corderman, K. Shukla, and R. C. Newman, “Computer simulations of corrosion: Selective dissolution of binary alloys,” *Philos. Mag. A*, vol. 59, no. 4, pp. 713–746, 1989.

[15] D. M. Artymowicz, J. Erlebacher, and R. C. Newman, “Relationship between the parting limit for de-alloying and a particular geometric high-density site percolation threshold,” *Philos. Mag.*, vol. 89, no. 21, pp. 1663–1693, 2009.

[16] J. Rugolo, J. Erlebacher, and K. Sieradzki, “Length scales in alloy dissolution and measurement of absolute interfacial free energy,” *Nat. Mater.*, vol. 5, no. 12, pp. 946–949, 2006.

[17] F. Kertis, J. Snyder, L. Govada, S. Khurshid, N. Chayen, and J. Erlebacher, “Structure/processing relationships in the fabrication of nanoporous gold,” *Jom*, vol. 62, no. 6. pp. 50–56, 2010.

[18] Y. Ding, Y. J. Kim, and J. Erlebacher, “Nanoporous gold leaf: ‘Ancient technology ’/advanced material,” *Adv. Mater.*, vol. 16, no. 21, pp. 1897–1900, 2004.

[19] L. H. Qian and M. W. Chen, “Ultrafine nanoporous gold by low-temperature

dealloying and kinetics of nanopore formation," *Appl. Phys. Lett.*, vol. 91, no. 8, pp. 89–92, 2007.

[20] X.-L. Ye, N. Lu, X.-J. Li, K. Du, J. Tan, and H.-J. Jin, "Primary and Secondary Dealloying of Au(Pt)-Ag: Structural and Compositional Evolutions, and Volume Shrinkage," *J. Electrochem. Soc.*, vol. 161, no. 12, pp. C517–C526, 2014.

[21] C. Herring, "Effect of change of scale on sintering phenomena," *J. Appl. Phys.*, vol. 21, no. 4, pp. 301–303, 1950.

[22] R. Mendoza, K. Thornton, I. Savin, and P. W. Voorhees, "The evolution of interfacial topology during coarsening," *Acta Mater.*, vol. 54, no. 3, pp. 743–750, 2006.

[23] Y. C. K. Chen-Wiegart, S. Wang, W. K. Lee, I. McNulty, P. W. Voorhees, and D. C. Dunand, "In situ imaging of dealloying during nanoporous gold formation by transmission X-ray microscopy," *Acta Mater.*, vol. 61, no. 4, pp. 1118–1125, 2013.

[24] Y. C. K. Chen-Wiegart, S. Wang, Y. S. Chu, W. Liu, I. McNulty, P. W. Voorhees, and D. C. Dunand, "Structural evolution of nanoporous gold during thermal coarsening," *Acta Mater.*, vol. 60, no. 12, pp. 4972–4981, 2012.

[25] Y. C. K. Chen, Y. S. Chu, J. Yi, I. McNulty, Q. Shen, P. W. Voorhees, and D. C. Dunand, "Morphological and topological analysis of coarsened nanoporous gold by x-ray nanotomography," *Appl. Phys. Lett.*, vol. 96, no. 4, pp. 213–215, 2010.

[26] Y. C. K. Chen-Wiegart, S. Wang, I. McNulty, and D. C. Dunand, "Effect of Ag-Au composition and acid concentration on dealloying front velocity and cracking during nanoporous gold formation," *Acta Mater.*, vol. 61, no. 15, pp. 5561–5570, 2013.

[27] J. Erlebacher and I. McCue, “Geometric characterization of nanoporous metals,” *Acta Mater.*, vol. 60, no. 17, pp. 6164–6174, 2012.

[28] T. Fujita, L. H. Qian, K. Inoke, J. Erlebacher, and M. W. Chen, “Three-dimensional morphology of nanoporous gold,” *Appl. Phys. Lett.*, vol. 92, no. 25, pp. 90–93, 2008.

[29] J. Erlebacher, “Mechanism of coarsening and bubble formation in high-genus nanoporous metals,” *Phys. Rev. Lett.*, vol. 106, no. 22, pp. 1–4, 2011.

[30] K. Kolluri and M. J. Demkowicz, “Coarsening by network restructuring in model nanoporous gold,” *Acta Mater.*, vol. 59, no. 20, pp. 7645–7653, 2011.

[31] H. Rösner, S. Parida, D. Kramer, C. A. Volkert, and J. Weissmüller, “Reconstructing a nanoporous metal in three dimensions: An electron tomography study of dealloyed gold leaf,” *Adv. Eng. Mater.*, vol. 9, no. 7, pp. 535–541, 2007.

[32] J. Snyder, P. Asanithi, A. B. Dalton, and J. Erlebacher, “Stabilized nanoporous metals by dealloying ternary alloy precursors,” *Adv. Mater.*, vol. 20, no. 24, pp. 4883–4886, 2008.

[33] A. A. Vega and R. C. Newman, “Nanoporous Metals Fabricated through Electrochemical Dealloying of Ag-Au-Pt with Systematic Variation of Au:Pt Ratio,” *J. Electrochem. Soc.*, vol. 161, no. 1, pp. 1–10, 2014.

[34] O. Okman and J. W. Kysar, “Fabrication of crack-free blanket nanoporous gold thin films by galvanostatic dealloying,” *J. Alloys Compd.*, vol. 509, no. 22, pp. 6374–6381, 2011.

[35] Y. Sun and T. J. Balk, “A multi-step dealloying method to produce nanoporous gold with no volume change and minimal cracking,” *Scr. Mater.*, vol. 58, no. 9,

pp. 727–730, 2008.

[36] A. Wittstock, J. Biener, and M. Bäumer, “Nanoporous gold: a new material for catalytic and sensor applications,” *Phys. Chem. Chem. Phys.*, vol. 12, no. 40, p. 12919, 2010.

[37] S. Ahl, P. J. Cameron, J. Liu, W. Knoll, J. Erlebacher, and F. Yu, “A comparative plasmonic study of nanoporous and evaporated gold films,” *Plasmonics*, vol. 3, no. 1, pp. 13–20, 2008.

[38] Z. Qi and J. Weissmüller, “Hierarchical nested-network nanostructure by dealloying,” *ACS Nano*, vol. 7, no. 7, pp. 5948–5954, 2013.

[39] Y. Ding and J. Erlebacher, “Nanoporous metals with controlled multimodal pore size distribution,” *J. Am. Chem. Soc.*, vol. 125, no. 26, pp. 7772–7773, 2003.

[40] J. Biener, G. W. Nyce, A. M. Hodge, M. M. Biener, A. V. Hamza, and S. A. Maier, “Nanoporous plasmonic metamaterials,” *Adv. Mater.*, vol. 20, no. 6, pp. 1211–1217, 2008.

[41] M. Hakamada and M. Mabuchi, “Fabrication, microstructure, and properties of nanoporous Pd, Ni, and their alloys by dealloying,” *Crit. Rev. Solid State Mater. Sci.*, vol. 38, no. 4, pp. 262–285, 2013.

[42] L. Y. Chen, T. Fujita, Y. Ding, and M. W. Chen, “A three-dimensional gold-decorated nanoporous copper core-shell composite for electrocatalysis and nonenzymatic biosensing,” *Adv. Funct. Mater.*, vol. 20, no. 14, pp. 2279–2285, 2010.

[43] F. Scaglione, P. Rizzi, and L. Battezzati, “De-alloying kinetics of an Au-based amorphous alloys,” *J. Alloys Compd.*, vol. 536, no. SUPPL.1, pp. S60–S64, 2012.

[44] F. Scaglione, F. Celegato, P. Rizzi, and L. Battezzati, "A comparison of de-alloying crystalline and amorphous multicomponent Au alloys," *Intermetallics*, vol. 66, pp. 82–87, 2015.

[45] Y. M. Wang, W. Zhang, and A. Inoue, "Nanoporous Cu wide ribbons with good mechanical integrity," *Mater. Sci. Eng. B Solid-State Mater. Adv. Technol.*, vol. 177, no. 7, pp. 532–535, 2012.

[46] B. W. Parks, J. D. Fritz, and H. W. Pickering, "The difference in the electrochemical behavior of the ordered and disordered phases of Cu3Au," *Scr. Metall.*, vol. 23, no. 6, pp. 951–956, 1989.

[47] S. Kameoka and A. P. Tsai, "CO oxidation over a fine porous gold catalyst fabricated by selective leaching from an ordered AuCu3 intermetallic compound," *Catal. Letters*, vol. 121, no. 3–4, pp. 337–341, 2008.

[48] T. Wada, K. Yubuta, A. Inoue, and H. Kato, "Dealloying by metallic melt," *Mater. Lett.*, vol. 65, no. 7, pp. 1076–1078, 2011.

2 Kinetics and Morphological Evolution during Liquid Metal Dealloying

2.1 Introduction

Liquid metal dealloying provides a rich experimental space to study metal composites and porous metal materials. While basic criteria for elemental systems that will undergo LMD are known, the details of how these structures form are not understood in as much detail as the mechanisms controlling porosity evolution during electrochemical dealloying. To design materials with specified structures and properties, the length scale of the microstructural morphology resulting from LMD must be understood and the kinetics of the process quantified. Like any other dealloying process, LMD requires transport of one species along the solid-liquid interface and simultaneous dissolution of another component that must then be removed by diffusion through the liquid phase. In electrochemical dealloying, the morphology of the resulting porous network is fairly consistent, with a bicontinuous structure of interconnected pores and ligaments forming under most conditions where dealloying occurs. The kinetics are also relatively simple, as described in Chapter 1, with dealloying proceeding at a constant interface velocity limited by the dissolution of terrace atoms from subsequent layers of the alloy. The basic processes required for LMD to occur are known, but how they interact is of key importance to comprehensively understand LMD.

This chapter will focus on answering the question of how the kinetic processes in LMD interact, by studying dealloying kinetics and morphology evolution in binary alloys of titanium and a refractory BCC metal which is immersed in molten Cu. Ta is the favored element as a model system here, but later Nb is used as well. Mo, W, Cr, and V share the same chemistry, and can be processed by analogous methods. While experiments can be conducted over a wide range of parameters, the initial stages of dealloying are difficult to study due to practical difficulties with experiments shorter than a few seconds. Experimental work is complemented here by phase field simulations of the early stages of dealloying to give insight into initial pattern formation, work done in collaboration with Prof. Alain Karma and his group at Northeastern University. Due to computational limitations, there are several orders of magnitude separating the largest simulation from the smallest experiment both in time and length scale, but nevertheless important insight can be gained by comparing the results using each method.

2.2 Experimental Methods

2.2.1 Alloy Preparation

The high temperatures and reactivity of the materials used for this study pose some unique processing challenges. The Ta-Ti parent alloys have melting points above 2000 °C and Ti melts are reactive with many common crucible materials, making preparation difficult. To prepare these alloys, induction heating was used to reach the temperatures required. A 45kW Ambrell Ekoheat ES power supply was used to heat metals in a water cooled copper crucible produced by Arcast (Oxford, ME). Due to the interaction of the induction field with the crucible, the metal being heated is pushed away from the walls of the crucible, limiting heat loss to improve efficiency, and maintaining the purity of the sample. This effect allows very high temperatures to be reached in optimal conditions where the sample is almost entirely levitated. On the other hand, it is difficult to heat samples that do not couple well with the induction field and thus retain a large contact area with the cold crucible surface. Even with this optimized equipment, alloy preparation presents a significant hurdle for this study. Ti alloys were not well-levitated by the Cu crucible, so some samples were melted many times to ensure total mixing. The large difference in density and melting point between Ti and Ta causes unmelted Ta pellets to rapidly sink to the bottom of the melt while remaining solid. Near the crucible bottom, the local temperature dropped enough that there was little driving force to dissolve Ta. Thus after a few minutes molten the melt had to be cooled, removed from the crucible, and inverted before remelting. Samples took approximately 6 minutes to cool sufficiently to handle easily. Cooling under a protected atmosphere is important to avoid oxidation of the sample surface which occurs rapidly at elevated temperatures. After inverting the sample, another several minutes were required to purge the atmosphere of the furnace chamber by alternately evacuating it to ~1 Torr and refilling with purified Ar. The total cycle time for each remelt was thus around 30 minutes, including assembling and disassembling the furnace chamber as well as the melting itself.

Another experimental consideration is the vapor pressure of Ti. The boiling point of Ti is close to the melting point of Ta, so significant evaporation occurs as Ta begins to dissolve in a Ti melt and the temperature required for continued dissolution increases. For the most Ti rich alloys (more than about 70 at. % Ti) this issue is not pronounced since the melting point of the alloy remains modest, but as the Ta fraction increases the rate of Ti evaporation from the melt increases rapidly. In this work, the most Ta rich samples were made with several percent extra Ti in the initial mixture, compensating for the expectation that it would evaporate during the alloying process to leave the proper composition in the final ingot.

BCC-stabilized titanium alloys are known to be very susceptible to oxygen embrittlement, so care must be taken to maintain a pure argon atmosphere during all heating [1]. This was accomplished by flowing the argon through a tube furnace packed with titanium sponge at approximately 650 °C to react with trace oxygen, water, and nitrogen gas entrained in the argon stream.

Many alloys are commonly prepared under high vacuum conditions rather than under an inert gas environment. In some cases, this is simply convenient for processing, while in others it can be of critical importance (for instance Pt-rich melts can dissolve sufficient Ar to produce internal bubbles upon solidification). For studies in this thesis, we initially used a high vacuum environment to prepare some samples by connecting a small turbo pump directly to the induction furnace chamber backed by the same roughing pump used for purging. Due to the lack of a bypass to pump the chamber down to rough vacuum without spinning down the turbo pump, alloy preparation requiring a series of remelts by this technique was extremely slow. Further, under high vacuum the melt acts as an evaporative deposition system, coating everything in line of sight with a layer of Ti. This is problematic because as the layer thickens, it begins to heat due to the same induction field heating the sample, which can cause furnace components to overheat and obscures vision of the sample both for the operator and the optical pyrometer for temperature measurement. At high furnace powers, Ti evaporation can cause a plasma to ignite in the vapor above the surface of the sample, which the manufacturer of the induction system strongly advises against. In short, high vacuum melting is not appropriate for the alloys of interest here.

Instead of vacuum, the alloy ingots used in this study were remelted repeatedly in inert atmospheres until they melted homogeneously upon heating, indicating an even distribution of Ta. The number of melts required for this varied significantly based on the composition of the alloy and how effectively the melts were maintained; in some cases the motion of the melting metal causes it to "stick" to the side of the cold crucible, solidifying rapidly and stopping the alloying process prematurely. Ingots melted insufficiently showed clearly visible pieces of Ta suspended in them upon cross sectioning. After melting, samples were annealed in the same cold crucible induction system at a temperature just below their melting point for approximately 8 hours to homogenize compositional variations, which are unavoidable during solidification. The temperature was determined by slowly heating the sample until the first melting was observed, then reducing the induction power by approximately 5%. Directly measuring the temperature in the induction melting system is difficult. Thermocouples are not usable because the induction heating itself interferes with temperature measurement. Optical pyrometry is commonly employed, but the system used here had no optical detector integrated into the system, so an external optical pyrometer observed the hot zone through a quartz window at the top of the sample chamber. Especially in high temperature Ti alloy melts, Ti evaporation on the quartz window can cause significant drift in the temperature measurement during a single experiment as deposition obscures the detector. In the relevant temperature regime, this can cause variation in the measured temperature of up to several hundred Celsius.

2.2.2 Liquid Metal Dealloying

The apparatus to perform LMD experiments evolved several times over the course of this work. In initial proof of concept experiments, the metal for the bath and the sample were placed adjacent to each other in a cast alumina trough. The bath was heated to the desired temperature then the trough was tilted to slide it into contact with the Ti alloy sample and dealloying occurred. This presented several problems for control, including difficulty monitoring temperature and controlling the reaction time precisely. To allow more precise experiments, a system was constructed where the bath remained stationary in an alumina crucible within the induction coil and the sample was lowered by hooking it to a Ta wire and lowering the wire from the end of a rod through a grommeted opening in the top of the heating chamber (replacing the port for the optical pyrometer, so no simultaneous temperature measurement was possible). This system allowed precise kinetic measurements to be taken, but the crucibles were single-use and the atmosphere purity was compromised by the greased rubber grommet used for the sample. The sample was also raised and lowered by manually pushing or pulling the top of the rod, which became uncomfortably hot during long experiments. In the final iteration of this system, the rod was replaced with a high vacuum manipulator arm with a crank, and the disposable alumina crucibles were replaced with machined boron nitride ceramic, together forming a clean, precise, and fully reusable dealloying system which eliminated an important source of sample-to-sample variation.

2.2.3 Sample Preparation and Characterization

After heat treatment, ingots were sectioned using either wire EDM or a diamond wafering saw, and the resulting slices were roughly hand-polished with sandpaper to remove cutting damage or EMD recast layer. They were then spot welded to a Ta wire and suspended from the manipulator arm. The Cu melt was heated at high power until fully molten using a 4.5kW Ameritherm Easyheat induction power supply, and allowed 10 minutes to equilibrate at the desired temperature before the sample was dipped to dealloy. After dealloying, samples were cross sectioned with a diamond wafering saw using 6-inch all-purpose metal cutting blades purchased from Pace Technologies. To observe the dealloyed cross section of the sample, it was mounted in a cylinder of conductive thermoset epoxy, which was roughly ground to the correct depth with sandpaper, then polished on a Struers Tegramin-20 autopolisher with 9 μm, 3 μm, and 1 μm diamond suspension and finally with 50 nm colloidal silica.

X-ray diffractometry (XRD) was performed using a Phillips PANalytical X'pert PRO diffractometer using Cu K-α radiation, and samples were observed by scanning electron microscopy (SEM) with a JEOL JSM-6700F field emission SEM equipped with secondary electron and annular backscattered electron detectors as well as energy dispersive x-ray spectroscopy (EDS) to provide local compositional analysis.

2.3 Results and Discussion

To investigate the kinetics of the LMD process, the first detailed study was made using Ti-Ta alloy samples dealloyed in molten Cu for several experimental times at a variety of temperatures by Ian McCue, myself, and coworkers [2]. Geslin, myself and

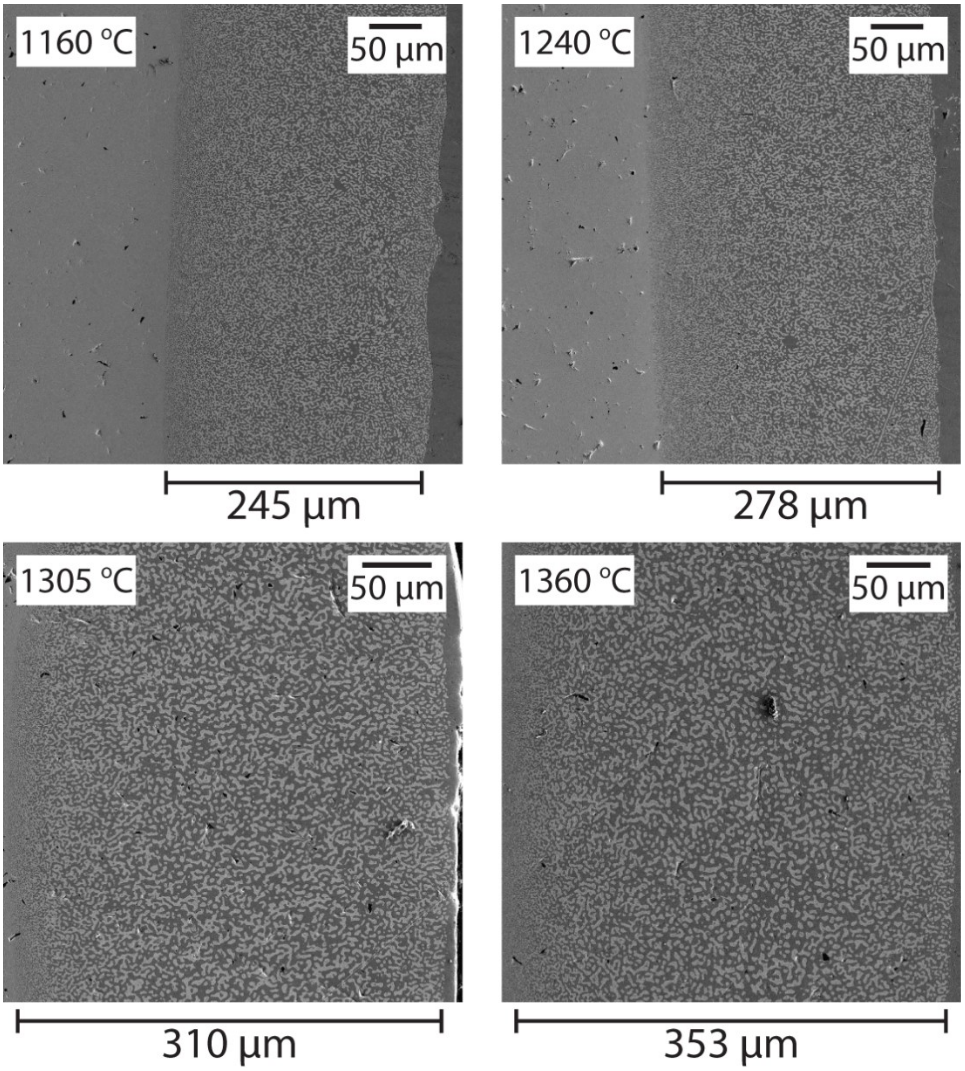

Figure 2-1: Scanning electron microscopy (SEM) micrographs of $Ti_{55}Ta_{45}$ samples dealloyed in molten Cu for 20 seconds at four temperatures. The dealloying interface is sharp and flat, and the dealloyed region has a natural contrast due to the different compositions; the dark phase is Cu and the light phase is Ta. The top two images were taken at 200x magnification and the bottom two were taken at 270x magnification, but it can be seen that dealloying depth increases with increasing time.

others [3], employing a combination of of phase field modeling and experiments, provide the first detailed look at the mechanisms of structure formation during LMD. In the remainder of this chapter, some results from these studies are summarized, addressing the kinetics and morphological evolution that provide the basis for detailed studies reported in later chapters. Of key importance are the velocity of the dealloying front, the topology of the LMD structure, and the evolution of feature size in LMD materials during the initial phase evolution and afterwards due to coarsening.

2.3.1 Dealloying Kinetics

After dealloying, the samples were cut and polished such that the cross section of the dealloyed region was visible, so the maximum depth dealloyed could be measured from the original surface of the sample to the dealloying interface (the edge of the dealloyed region where Ti dissolution is occurring). The dealloyed region is known to shrink slightly in volume as it dealloys, but measurement of the sample dimensions before and after LMD showed that this effect did not significantly alter the measured depths. **Figure 2-1** shows SEM micrographs for a representative set of experiments where a single starting composition was dealloyed for 20 seconds, showing the dealloyed depth increasing at higher temperatures. Plotting the dealloyed depth from several such datasets (**Figure 2-2**) shows that the dealloyed depth increases with time, but rather than scaling linearly the dealloying rate slows over time. The dealloying rate also slows with increasing Ta fraction in the starting alloy.

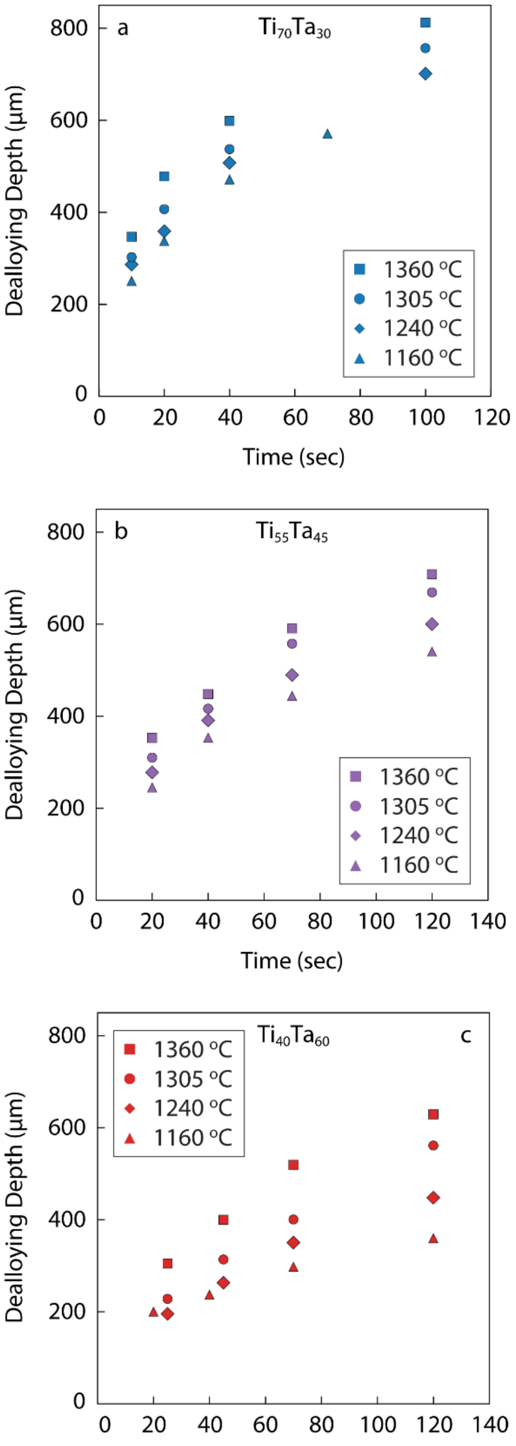

Figure 2-2: Dealloying depth versus time for the samples in this study. We studied four temperatures: 1160 °C (triangle), 1240 °C (diamond), 1305 °C (circle), and 1360 °C (square), four times (10-120 seconds), and three compositions: (a) $Ti_{70}Ta_{30}$ (blue), (b) $Ti_{55}Ta_{45}$ (purple), and (c) $Ti_{40}Ta_{60}$ (red).

The rate of dealloying decreases because the rate limiting step in the LMD process is the diffusion of Ti away from the dealloying interface. As the dealloyed depth increases, the distance newly dissolved Ti must diffuse through the porous network increases, and the longer diffusion time causes the overall rate to slow. At the dealloying interface, the solid and liquid are in equilibrium, so the liquid concentration of Ti should depend only on the solid Ti fraction, and experiments confirm that the liquid composition at this moving interface remains relatively constant throughout the experiment. At the opposite edge of the dealloyed region the sample is in contact with a bath of molten metal. In the experiments here, this bath is very large compared to the size of the sample (a 40 g bath compared to samples around 1 g) so for the purposes of modeling the diffusion of Ti, the bath far away from the sample remains at a Ti concentration close to zero. Due to the flow in the bath from induction heating, dissolving Ti is rapidly carried away once it leaves the porous region of the sample and becomes subject to convection. Thus the liquid Ti concentration was set to zero at the plane of the original surface of the sample. Based on these boundary conditions, a model for the diffusion of Ti based on the one-dimensional Stefan problem is presented in Reference [2], where the concentration profile of Ti in the solution is derived in detail.

The primary conclusion that can be drawn from this result is that the dealloying depth slows with time due to diffusion limited transport of dissolved Ti away from the interface. Like many other diffusion-limited rate problems, the solution to the Stefan problem gives a depth that has a square root dependence on time, which visually matches the data in **Figure 2-2**. The main temperature dependence in the model is the diffusivity itself, which has an Arrhenius relationship with temperature, with activation barriers tabulated in Reference [2]. The dealloyed depths can be scaled by the Arrhenius factor of the diffusivity to give a temperature-independent dealloying depth that is plotted against time in **Figure 2-3**, with the data collapsing onto parabolic power law fits as anticipated.

Unlike this LMD system, electrochemical dealloying is usually considered to progress at a constant rate. When the dealloying is driven by an applied potential, this rate can be observed directly since the current that passes through the circuit is directly proportional to the volume of dissolved material. Because diffusion in aqueous electrolytes is much faster than the dissolution step of this dealloying process, there is never a notable concentration gradient of the dissolving species in the porous region or near the surface. While the diffusion-limited nature of LMD is important due to the resulting power law dealloying rate, it also creates a unique chemical environment within the pores where a significant fraction of the liquid is the dissolving component rather than the bath. As we will show later, this effect can lead to interactions occurring within the pores that would not be possible otherwise, which can cause unwanted side effects but also provide an additional route to more complex LMD materials.

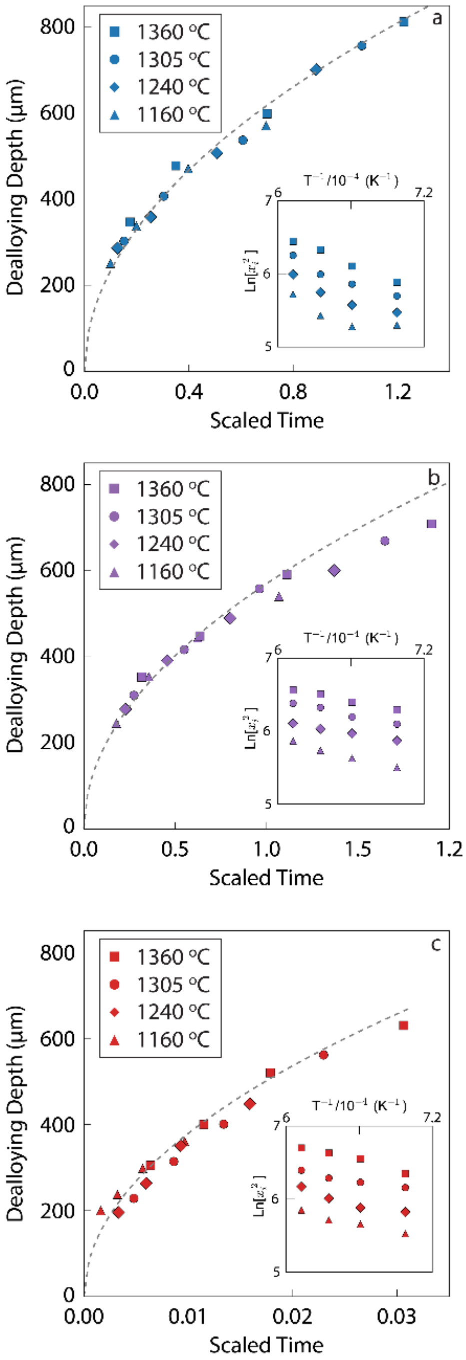

Figure 2-3: Collapsed dealloying depth versus scaled time $t' = t * \exp\left(-E_a/k_BT\right)$ for $Ti_{70}Ta_{30}$ (blue), $Ti_{55}Ta_{45}$ (purple), and $Ti_{40}Ta_{60}$ (red). The symbol shape corresponds to the experimental temperature: triangle (1160 °C), diamond (1240 °C), circle (1305 °C), and square (1360 °C). Dashed lines: fits to the data using the relationship $x_i\left(t\right) = \sqrt{4pD_Lt}$. (Insets) Arrhenius plots of each dealloying time showing clear linear behavior across our temperature range. Kinetic parameters for each sample are listed in Reference [2].

2.3.2 Morphology Evolution

By combining phase-field modeling and experiments, we revealed the key mechanisms controlling the formation and evolution of topologically complex structures during LMD for the baseline Ti-Ta dealloyed in Cu case. Phase field modeling is a technique for simulating dynamic systems where, in general, a phase field distinguishes a key parameter that varies between discrete states. Here, the phase field has one value for liquid and another for solid, and varies smoothly between two values across the discrete width of the solid-liquid interface. This phase field is coupled to the concentration field of each component in the system, and the entire system evolves based on a free energy function that accounts for the phase behavior of the components as well as the energetic contribution from the interfaces. Phase field modeling is a well-developed field with applications in a variety of dynamic systems. The type of model used here is common for simulating phenomena including solidification of melts into multiphase metals. More detail on the methodology is available in the methods section of Reference [3].

Experiments were carried out by dealloying $Ta_{c0}Ti_{1-c0}$ alloys with an initial (mole fraction) composition c_0 in contact with pure Cu liquid. We used a standard phase-field model of ternary alloys with parameters that approximate the Ta–Ti–Cu system. Simulations were carried out in both two and three dimensions (2D and 3D) to highlight topological differences dependent on dimensionality and to access longer time scales in 2D. The ability of the phase-field method to model complex interfacial patterns in solidification [4]–[7] and other phase transformations [8] makes it a method of choice to explore topologically complex dealloyed structures. Moreover, the simpler structure of the solid–liquid interfaces in metallic alloys, compared with alloy-electrolyte interfaces, makes the phase field method readily able to investigate dealloying in the context of LMD. Using phase-field simulations and experiment, we show that interfacial spinodal decomposition destabilizes the dealloying front via the formation of compositional domains enriched in the immiscible element with an initial spacing of several nanometers. We further show that interface pattern evolution at intermediate time and length scales is controlled by 'diffusion-coupled growth' of solid domains enriched in the immiscible element and the liquid phase enriched in the miscible element. This pattern formation mechanism is remarkably analogous to the coupled growth of two-phase structures in solidification [9] and other phase transformations [10], but unanticipated in LMD where alloys do not typically exhibit three-phase equilibria.

Figure 2-4 illustrates the different topologies observed in simulations and experiments as a function of initial alloy composition c_0, combining 3D simulations, 2D simulations, and micrographs taken of the cross section from analogous experiments for four compositions of starting alloy. For high c_0, a connected 3D structure of A-rich ligaments is formed. **Figure 2-4a** illustrates the evolution of the solid–liquid interface during the formation of this structure for c_0=25%. This complex evolution yields a bicomposite of interpenetrating A-rich and B–C phases (also a nanoporous structure after the B–C phase is etched out). Interestingly, over the same composition range, ligaments of corresponding simulated 2D structures are disordered but not connected (**Figure 2-4b,c**). For a lower intermediate range of c_0, a 3D filamentary structure is formed consisting of disconnected A-rich filaments inside the B–C matrix, also manifested as a lamellar structure in 2D. Filaments or lamellae are aligned along an axis perpendicular to

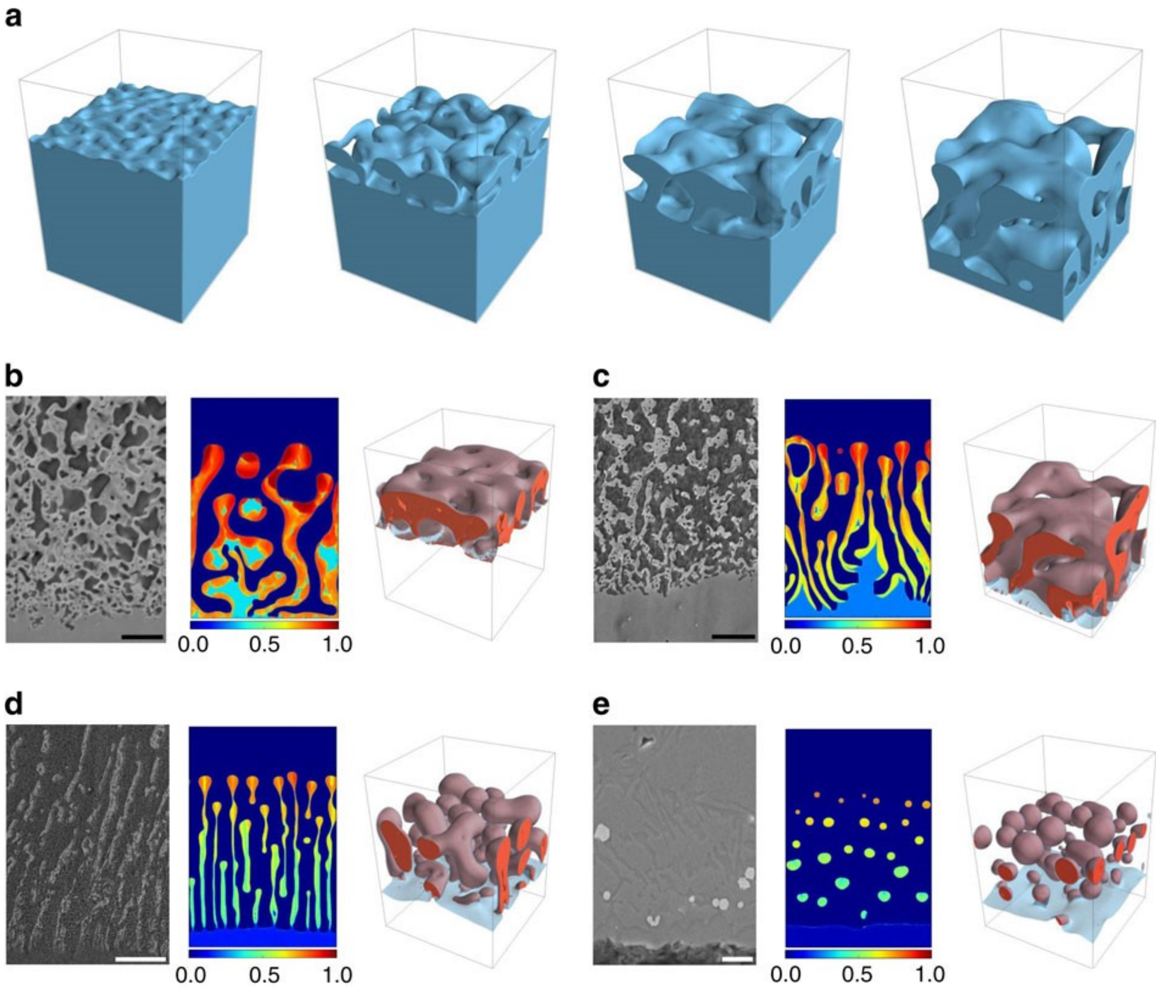

Figure 2-4: (**a**) Phase-field simulation illustrating the formation of a topologically connected bicontinuous nanostructure during the dealloying of a $A_{c_0}B_{1-c_0}$ alloy in contact with a pure C liquid for c_0=25%. Snapshots of the solid–liquid interface (φ=1/2 surface) are shown at dealloying times $tD_l/w_i^2 = 80,\ 320,\ 640,\ \text{and}\ 1,260$. The simulation domain size is 96 × 96 × 128 nm^3. Structures for c_0=35% (**b**), c_0=25% (**c**), c_0=15% (**d**) and c_0=5% (**e**) in experiments, and 2D and 3D simulations in domain sizes 256 × 384 nm^2 and 96 × 96 × 128 nm^3, respectively. 2D simulation results are shown by a colourmap of the concentration of the immiscible alloy element A. For 3D results, the solid–liquid interface is represented in transparent light blue, while the red surface represents an iso-concentration surface c_A=1/2, delimiting the A-rich solid phase. The solid–liquid interface appears in light blue at the dealloying front and brown (due to color addition of light blue and red) when the interface covers the A-rich phase. Scale bars, 1 µm (**b**), 3 µm (**c**), 10 µm (**d**) and 5 µm (**e**) (on experimental pictures, respectively).

the dealloying front (**Figure 2-4d**) and filaments can further break up into aligned blobs in 3D. For low c_0, a globular structure is formed consisting of randomly dispersed 3D blobs (or 2D islands) of the A-rich phase in the B–C matrix (**Figure 2-4e**). It is important to emphasize that topologically disconnected filamentary and blob structures do not have a direct analog in electrochemical dealloying that yields connected structures even for very low composition, for example, as low as 2%Au in Ag–Au alloys [11]. Filaments and blobs during LMD result from interfacial pattern formation and not from topological changes induced by coarsening of an already formed connected structure. Simulations probe smaller dealloying depths than the experiments but are large enough to reproduce salient features of the observed topologies for different alloy compositions. Furthermore, they capture very early stages of interfacial pattern formation that are impossible to investigate experimentally with the currently available techniques.

These phase field simulations address the early stages of dealloying and the formation of Ta rich ligaments at the dealloying interface, but the structure of LMD materials continues to evolve away from the interface as ligaments coarsen. **Figure 2-5** shows that differences in morphology are still visible for difference concentrations in a cross section taken near the original surface of the sample, where ligaments have had the longest time to evolve after the dealloying front moved away. We observed good mechanical integrity when the Ta concentration was greater than ~30 at.%, owing to the connectivity in the porous network, which is a major reason why this work focuses on Ta-rich alloys. Samples with lower Ta concentrations were mechanically stable for short immersion times (less than 10 seconds), but fell apart during longer immersions (greater than 20 seconds). Only samples with at least 30 at.% Ta were robust enough to hold together during long immersion experiments (up to 120 seconds). This variety of morphologies promises to make LMD much more flexible than electrochemical dealloying with respect to the types of structures that can be made.

2.3.3 Ligament Size and Coarsening

One of the most important characteristics of dealloyed materials is the consistently narrow distribution of the width of the ligaments and pores, and more specifically the ability to tune this parameter by selecting the dealloying conditions and through post-dealloying coarsening treatments. In electrochemical dealloying, it has been shown that this feature size depends on processing temperature, with Chen et al. forming significantly finer features in nanoporous gold by dealloying below room temperature [12]. There is also variation in ligament size depending on the metal, with higher melting point elements generally having smaller features. Chen and Sieradzki showed that the feature sizes scaled almost universally with the homologous temperature during dealloying, that is the solution temperature normalized by the melting point of the porous metal [13]. They suggest that this universal relationship is due to the scaling of surface mobility with melting point, with atoms of lower-melting metals are able to move more freely and thus travel greater distances to organize into larger ligaments. Another implication of this relationship is that some metals with high melting points cannot form porosity by dealloying at room temperature, because the resulting pores would be smaller than an atomic dimension.

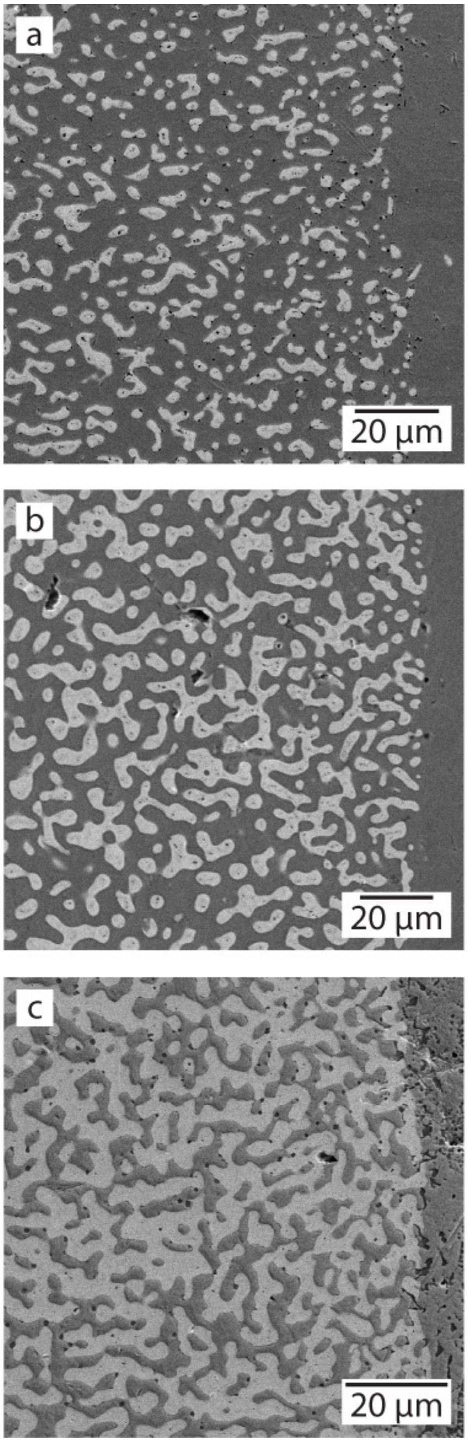

Figure 2-5: Difference in morphology at the edge of samples dealloyed for 20 seconds at 1305 °C as a function of alloy composition (in all cases the morphology underwent significant coarsening): (A) $Ti_{70}Ta_{30}$ showing mostly disconnected blobs, (B) $Ti_{55}Ta_{45}$ showing a mixture of disconnected blobs and connected ligaments, and (C) $Ti_{40}Ta_{60}$showing a highly connected structure.

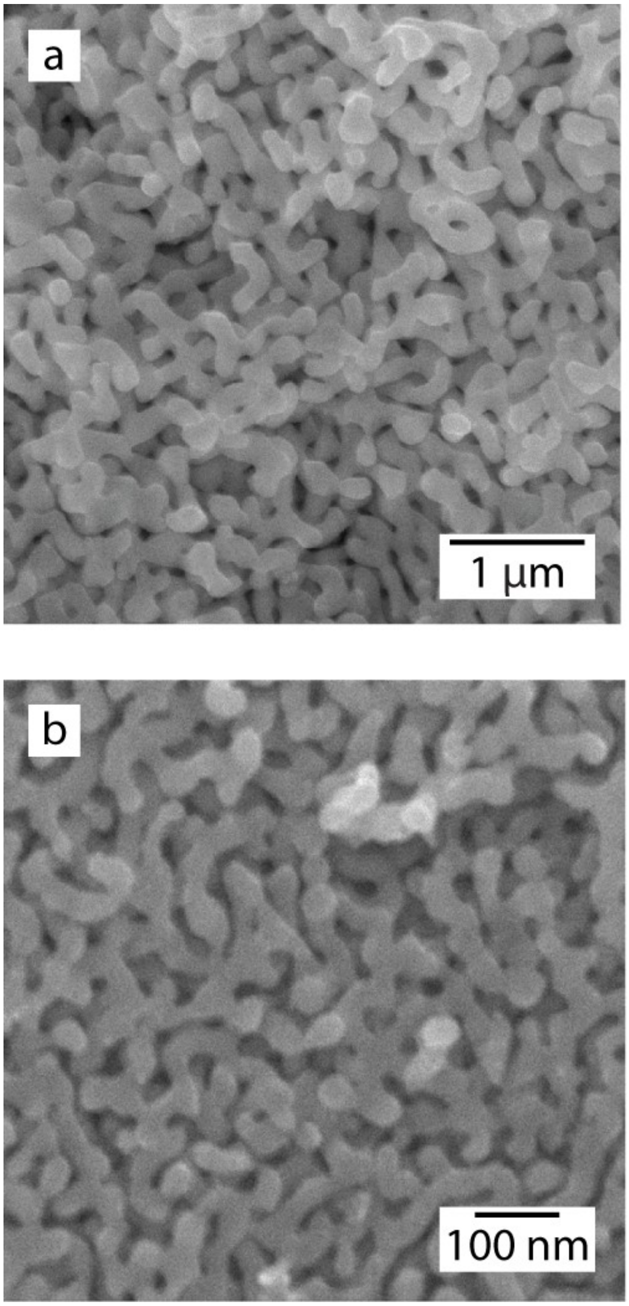

Figure 2-6: Ligament size temperature dependence shown in porous Ta. (A) SEM micrograph of porous Ta with ~100 nm ligaments, dealloyed for an hour in $Cu_{32}Ag_{68}$ (T_m ~ 780 ºC). (A) SEM micrograph of porous Ta with ~50 nm ligaments, dealloyed for an hour in $Cu_{20}Ag_{40}Bi_{40}$ (T_m ~ 600 ºC).

Due to the relatively small temperature window available to aqueous electrolytes, only a small section of the length scale range for dealloyed materials has been accessible.

However, LMD unlocks a much wider temperature range in many systems. In LMD of Ta-Ti alloys, the lower bound on the temperature is the melting point of copper at 1085 °C. The temperature can be increased without a significant change in the phase behavior required for dealloying until Ta starts dissolving significantly around 1600 °C. This 500 °C window is five times larger than the liquid range of water already, but it can be widened even further. Copper forms eutectic melts with several elements. In particular, silver lowers the melting point by as much as 300 °C while maintaining the immiscibility with Ta necessary to preserve dealloying. The melting point can be further depressed by the addition of lower melting elements such as bismuth, lead, or tin, pushing the minimum practical dealloying temperature as low as 650 °C. **Figure 2-6** shows the much wider range in feature sizes for an individual metal system compared to electrochemical dealloying, with Ta dealloyed in baths containing Ag or Bi to depress the melting point of the Cu-rich liquid without altering the dealloying chemistry. Other refractory metals with the body-centered cubic crystal structure, including Nb and W, can also form Ti alloys that dealloy in Cu melts. Due to the range of melting points for these metals, slightly different feature sizes are expected at the same dealloying temperature. In **Figure 2-7**, experiments with Ta, Nb, and W had their average ligament size measured, and plotted against the ratio of melting point to the dealloying temperature. Superimposing these points on the trend line from Reference [13] yields good agreement with the temperature scaling of length scale between electrochemically dealloyed metals and these LMD samples. This implies that surface diffusion continues to control the final ligament size in these LMD experiments, and that the relevant diffusion coefficients in a liquid metal environment have comparable temperature dependence compared to values in

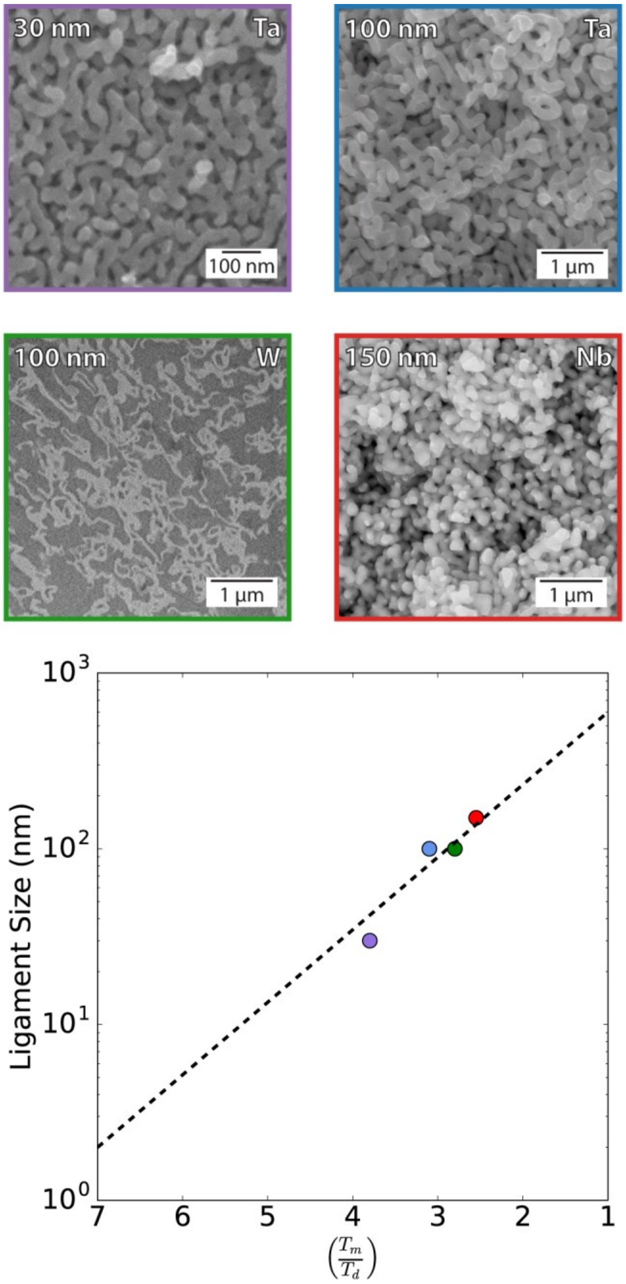

Figure 2-7: SEM micrographs of nanoporous Ta and Nb and a composite of W in Cu made by dealloying Ti-based binary alloys in molten Cu or Cu mixtures and dissolving the liquid phase (top). Superimposing the length scale of each sample on the trend line from Reference [8] (bottom) shows that the feature size scaling relation with homologous temperature is maintained in liquid metal dealloying.

electrolytes. This general trend is an important indicator of what length scale can be expected for the features when planning an LMD experiment in a new system. These

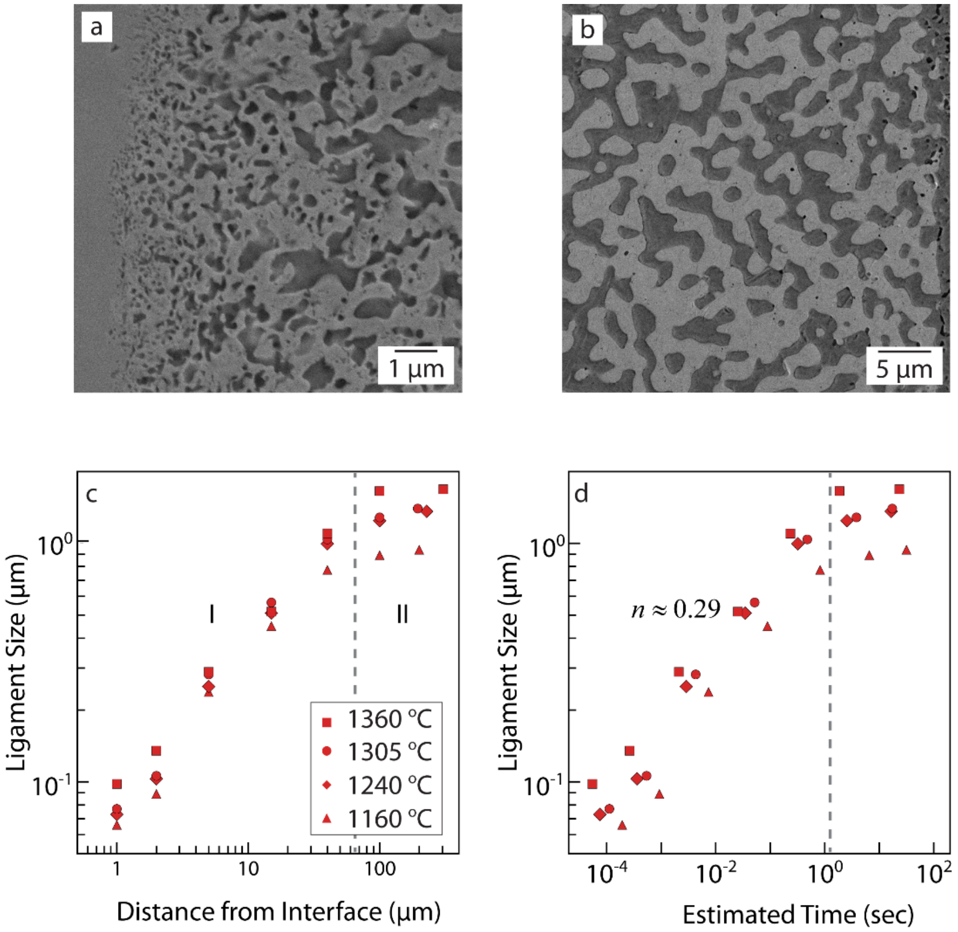

Figure 2-8: Ligament coarsening during LMD using $Ti_{40}Ta_{60}$ as an example. (A) SEM micrograph of the dealloying interface (left of the image) showing ligaments ~80 nm at the interface. (B) SEM micrograph of the edge of the sample (right of the image) showing ~1.5 µm ligaments at the edge of the sample. (C) Ligament size versus distance away from the dealloying interface, with two distinct coarsening regimes. (D) Ligament size versus estimated time, with the power law exponent of best fit n=0.29 for the data in region I.

length scales can always be increased after initial porosity formation due to thermal coarsening, but this relationship provides a rough lower bound on feature sizes in addition to quantitatively suggesting a path to finer features via lower temperature processing.

We observed a significant amount of ligament coarsening during LMD in molten Cu, with nm-sized features at the interface and µm-sized features at the edge of the sample. **Figure 2-8a,b** contrasts the ligament size in a $Ti_{40}Ta_{60}$ sample where the ligaments are ~80 nm at the interface and rapidly increase to ~ 1 μm at the edge of the sample. The morphology of the structures was composition dependent, but in general the length scale was approximately the same as it varied away from the interface regardless of the composition.

It was shown in previous work that coarsening in nanoporous metals consists of two concurrent surface diffusion-mediated processes: surface smoothening and ligament pinch-off events [14], [15]. In an ideal case both have a $t^{1/4}$ dependence, but the mutual dependence of these two processes leads to a more complicated relationship for the surface evolution in nanoporous metals. **Figure 8c** shows the ligament size versus dealloyed depth for $Ti_{40}Ta_{60}$, dealloyed for 20 seconds at 1160, 1240, 1305, and 1360 ºC. The ligament size has a power law relationship with time close to the expected form in region I, before slowing down dramatically in region II, but there is insufficient data here to provide any more detail on a possible mechanistic change between the two regions. In order to form bulk porous structures with finer-scale porosity, the details of ligament coarsening must be elucidated so the coarsening rate can be slowed relative to the dealloying rate.

2.4 Conclusions

We have discussed the thermodynamic and kinetic fundamentals of the LMD process, using the dealloying of Ta-Ti binary alloys in Cu as a model system. In this system, the rate of dealloying is controlled by the diffusion of Ti in the liquid phase away from the dealloying interface, and the measured diffusion constants match well with literature values. This is in contrast to electrochemical dealloying where the rate is interface reaction limited and the dealloyed depth increases linearly in time. The ultimate size of the ligaments, however, seems to follow the trend observed electrochemically, so we hypothesize that the rate of ligament coarsening remains controlled by surface diffusion. The morphology produced by dealloying can be controlled by varying the initial alloy composition, with bicontinuous porous structures forming in a range of Ta fractions between 0.6 and 0.25. The range of ligament sizes available in LMD, like dealloying in general, can be estimated by the ratio of dealloying temperature to the melting point of the metal.

Taken in combination, these conclusions serve as a comprehensive basis to engineer the structure of LMD materials by controlling the dimensions of the dealloyed region as well as the ligament size and topology. This provides a vital theoretical foundation to design more complex LMD systems by adding additional elements with a variety of effects to the liquid bath or the starting alloy.

2.5 References

[1] Z. Liu and G. Welsch, “Effects of oxygen and heat treatment on the mechanical properties of alpha and beta titanium alloys,” *Metall. Trans. A*, vol. 19, no. 3, pp. 527–542, 1988.

[2] I. McCue, B. Gaskey, P. A. Geslin, A. Karma, and J. Erlebacher, “Kinetics and morphological evolution of liquid metal dealloying,” *Acta Mater.*, vol. 115, pp. 10–23, 2016.

[3] P. A. Geslin, I. McCue, B. Gaskey, J. Erlebacher, and A. Karma, “Topology-generating interfacial pattern formation during liquid metal dealloying,” *Nat. Commun.*, vol. 6, pp. 1–8, 2015.

[4] W. J. Boettinger, J. A. Warren, C. Beckermann, and A. Karma, “Phase-Field Simulation of Solidification,” *Annu. Rev. Mater. Res.*, vol. 32, no. 1, pp. 163–194, 2002.

[5] L. Gránásy, T. Pusztai, J. A. Warren, J. F. Douglas, T. Börzsönyi, and V. Ferreiro, “Growth of ‘dizzy dendrites’ in a random field of foreign particles,” *Nat. Mater.*, vol. 2, no. 2, pp. 92–96, 2003.

[6] T. Haxhimali, A. Karma, F. Gonzales, and M. Rappaz, “Orientation selection in dendritic evolution,” *Nat. Mater.*, vol. 5, no. 8, pp. 660–664, 2006.

[7] I. Steinbach, “Phase-field models in materials science,” *Model. Simul. Mater. Sci. Eng.*, vol. 17, no. 7, pp. 1–31, 2009.

[8] L.-Q. Chen, “Phase-Field Models for Microstructure Evolution,” *Annu. Rev. Mater. Res.*, vol. 32, no. 1, pp. 113–140, 2002.

[9] J. A. Dantzig and M. Rappaz, *Solidification*. EPFL press, 2009.

[10] M. Asta, C. Beckermann, A. Karma, W. Kurz, R. Napolitano, M. Plapp, G. Purdy, M. Rappaz, and R. Trivedi, “Solidification microstructures and solid-state parallels: Recent developments, future directions,” *Acta Mater.*, vol. 57, no. 4, pp. 941–971, 2009.

[11] J. Snyder and J. Erlebacher, “Kinetics of Crystal Etching Limited by Terrace Dissolution,” *J. Electrochem. Soc.*, vol. 157, no. 12, p. S21, 2010.

[12] L. H. Qian and M. W. Chen, “Ultrafine nanoporous gold by low-temperature dealloying and kinetics of nanopore formation,” *Appl. Phys. Lett.*, vol. 91, no. 8, pp. 89–92, 2007.

[13] Q. Chen and K. Sieradzki, “Spontaneous evolution of bicontinuous nanostructures in dealloyed Li-based systems,” *Nat. Mater.*, vol. 12, no. 12, pp. 1102–1106, 2013.

[14] K. Kolluri and M. J. Demkowicz, “Coarsening by network restructuring in model nanoporous gold,” *Acta Mater.*, vol. 59, no. 20, pp. 7645–7653, 2011.

[15] J. Erlebacher, “Mechanism of coarsening and bubble formation in high-genus nanoporous metals,” *Phys. Rev. Lett.*, vol. 106, no. 22, pp. 1–4, 2011.

3 Controlling Morphology by Tuning the Driving Force in Liquid Metal Dealloying

3.1 Introduction

Material design and optimization is a time-consuming process due to the variety of variables in many complex materials. Modern computational tools can streamline this process by simulating an array of experimental conditions to identify key trends which should be tested experimentally. Metallurgical processes including alloy solidification have been successfully simulated using phase field modeling [1], [2]. Previously, we have used phase field simulations to study the formation of complex structures during liquid metal dealloying (LMD), where a binary alloy of titanium and tantalum is immersed in a liquid copper bath such that titanium dissolves and tantalum rearranges into a variety of structures depending on the initial conditions [3], [4].

LMD is a field of interest primarily due to the unique structures that can be prepared, including fully dense metal-metal composites with promising mechanical properties and new porous materials for use in batteries and capacitors. While new elemental systems for LMD are rapidly being identified and investigated experimentally [5], [6], the efficiency of experimental studies can be improved via feedback from simulations. One hurdle to effectively simulating LMD is the disparity in length and time scales between simulations and experiments. In our LMD experiments, a sample is physically lowered into a molten metal bath and then raised after a specified time interval. For the reaction to occur, the sample must first heat to the bath temperature, and it must cool afterward for the reaction to terminate. Both processes take around a second, so the experimental time must be significantly longer to avoid introducing a significant systematic error in timing. In a 10 second experiment, Ta-Ti binary alloys LMD in molten Cu can dealloy up to several hundred micrometers from the surface. In contrast, phase field modeling rapidly becomes computationally expensive as the time grows, because the spatial extent of the dealloyed area and thus the required simulation volume continue to grow. With these limitations, it is important to understand how simulated behavior relates with experimental observations. In this study, we investigate the structure that forms during LMD of starting alloys in a composition range close to the threshold where a bicontinuous morphology can evolve. By observing the prevalence of lamellar growth in simulations as the driving force for Ti dissolution varies, we are able to predict a regime where a connected porous structure is formed from low-Ta precursor alloys and validate this prediction experimentally.

3.2 Experimental

Liquid Metal Dealloying: Titanium-tantalum binary alloys were produced by induction melting pure Ti evaporation pellets (Kurt J. Lesker, 99.995%) and Ta evaporation pellets (Kurt J. Lesker, 99.9%) with an 45 kW Ambrell Ekoheat ES induction power supply and a water-cooled copper crucible purchased from Arcast, Inc (Oxford, ME). After melting several times, each alloy was annealed for 8 hours at a temperature within 200 °C of the melting point to allow homogenization and grain growth. Samples cut from this parent ingot were attached to a Ta wire by spot welding and suspended from a manipulator arm. The metal bath was prepared by heating a 40g mixture of Cu (McMaster Carr, 99.99%) with Ag (Kurt J. Lesker, 99.95%) or Ti pellets at high power using a 4kW Ameritherm Easyheat induction heating system until the bath was fully molten. The power was decreased, and the bath was allowed to mix and equilibrate at the reaction temperature of 1240 °C for half an hour. The manipulator arm was then lowered to immerse the sample in the bath for the specified time, before removing the sample to allow it to cool. All heating for both alloy preparation and LMD was performed in a purified Ar atmosphere. After dealloying, sample cross sections were polished and observed by optical microscopy and scanning electron microscopy (SEM, JEOL JSM-6700F). Elemental analysis was performed by energy dispersive x-ray spectroscopy (EDS) in the SEM. The three-dimensional microstructure of the dealloyed samples was observed by dissolving the solidified Cu-rich phase in 35% nitric acid solution (ACS reagent grade, Fluka).

Phase field modeling was performed by the same method described in detail in Reference [3] by the Karma group at Northeastern University.

3.3 Results and Discussion

In all experiments and simulations presented here, Ti-Ta binary alloys were dealloyed in a Cu-rich liquid in which Ti is much more soluble than Ta, leading to Ti dissolution. LMD is a kinetically complex process where constant competition between the dissolution rate of Ti and the surface rearrangement rate of Ta causes morphology to evolve. Here, we modify this balance by changing the composition of the liquid to decrease the driving force for Ti dissolution.

$Ta_{15}Ti_{85}$ dealloyed in a pure Cu melt forms a lamellar structure analogous to eutectic growth, with alternating layers of Ta-rich solid and Cu liquid extending into the

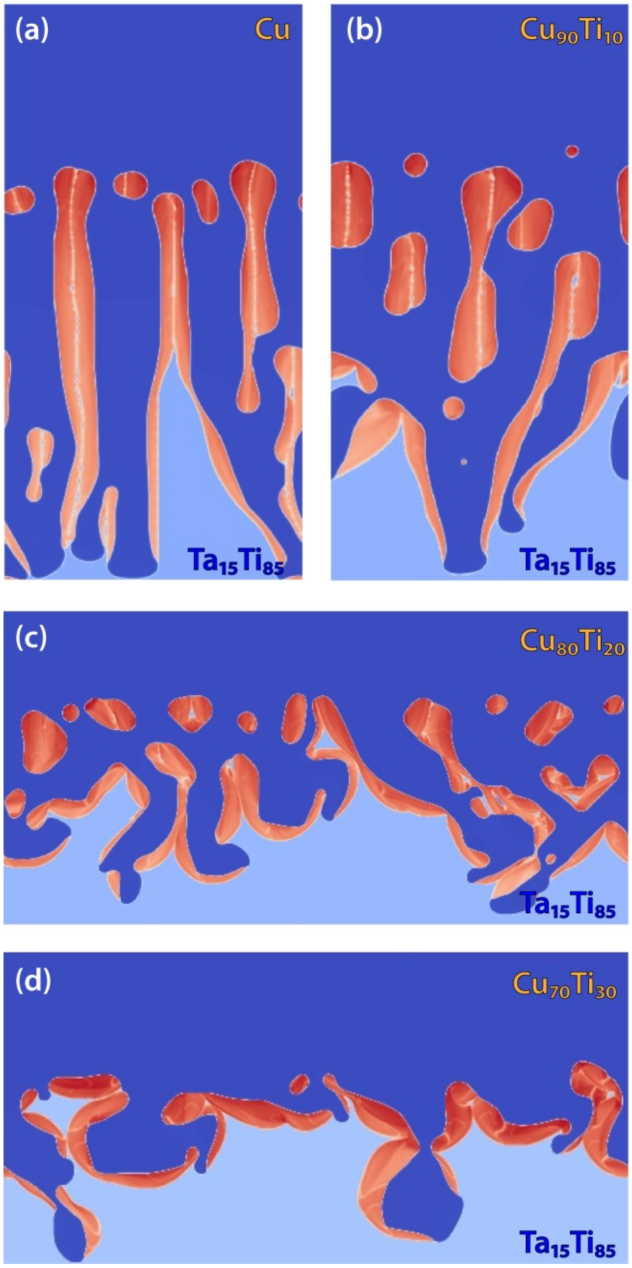

Figure 3-1: Two-dimensional phase field simulations of $Ta_{15}Ti_{85}$ dealloying in baths of pure Cu (a), $Cu_{90}Ti_{10}$ (b), $Cu_{80}Ti_{20}$ (c), and $Cu_{70}Ti_{30}$ (d). Areas are colored based on Ta concentration, where red is Ta rich, light blue is the starting alloy with 15% Ta, and dark blue is the liquid with almost zero dissolved Ta.

starting alloy perpendicular to the initial surface (See **Figure 2-1** for an example). As a liquid domain grows into this alloy, Ti dissolution leaves a region at the edge of the solid around the liquid channel enriched in Ta. In order for the dealloying to continue to form this lamellar structure, the excess Ta partitions to either side of the liquid domain, exposing additional Ti which can continue the dissolution and growth process. In this composition range, Ta can partition at a rate that balances Ti dissolution, so channels can grow without interruption from Ta buildup. If the starting alloy is more Ti rich, the liquid channels are able to grow laterally and undercut the lamellae of Ta, and they pinch off into oval blobs with the long axis in the dealloying direction, producing a discontinuous structure. If Ta fraction is instead increased, a topologically complex bicontinuous structure familiar from earlier dealloyed metals forms. In this case, Ta can no longer rearrange quickly enough ahead of a growing liquid domain, so instead of stable linear liquid channels, the liquid is forced to redirect into a more tortuous structure. Critically, the liquid channels also split if excess Ta builds up at the tip, and recombine randomly as they travel into the alloy, which causes the complex topology of the porous structure to grow.

The driving force for Ti dissolution is very high in a Cu melt. Just above the melting point of Cu at 1085 °C, Ti already has more than 70 at. % solubility in a Cu melt due to several low-melting intermetallic compounds between the two elements. One way to reduce this driving force is to initially dissolve some Ti into the liquid bath so the effective solubility for the dissolution of additional Ti from the solid is lower. The miscibility between Ti and Ta means this also increases the solubility of Ta in the liquid phase significantly, so Ta dissolution from the solid is no longer negligible. **Figure 3-1** shows the results of two-dimensional phase field simulations of $Ta_{15}Ti_{85}$ dealloying in a bimetallic melt of Cu with Ti added. With 10 at. % Ti in the liquid phase, the general morphology is maintained, with channels of liquid oriented into the solid. When additional Ti is added to make the liquid 20 at. % Ti, dealloying slows significantly, which is expected because the driving force is lowered. Also, the dealloying path becomes more tortuous, with liquid domains forced to turn or bifurcate rather propagate in a straight line normal to the dealloying interface. At 30 at. % Ti, the morphology changes further. The structure forms more slowly and some areas of the surface are close to passivating, with flat Ta rich areas protecting additional Ti from dissolution; nonetheless, bulk dealloying still proceeds. This result is interesting because it matches the effect of changing the solid composition, where dealloying slows down as the Ta fraction increases, but with the structure becoming more connected.

Using two-dimensional simulations has some drawbacks compared to 3-D simulations in terms of predicting experimental morphologies from LMD. A connected bincontinuous structure is impossible in two dimensions, so areas of material will always become detached from the parent alloy, but changes in the shape evolution can be indicative of changing dealloying mechanisms as well. Understanding the links between observations in 2-D simulations, 3-D simulations, and experimental results is vital. This understanding allows 2-D simulations to be employed to rapidly screen a variety of compositions to identify key regions of the experimental space to evaluate further with more expensive 3-D simulations or experiments.

Our simulations were validated by dealloying pieces of $Ta_{15}Ti_{85}$ in Cu melts containing 20% and 30% Ti (**Figure 3-2**). The morphology of the resulting Ta phase is more complex than a lamellar structure. Near the dealloying interface it appears to form the characteristic bicontinuous structure, but towards the original surface of the sample the ligaments become sparse and uniformly rounded, suggesting that they are in fact

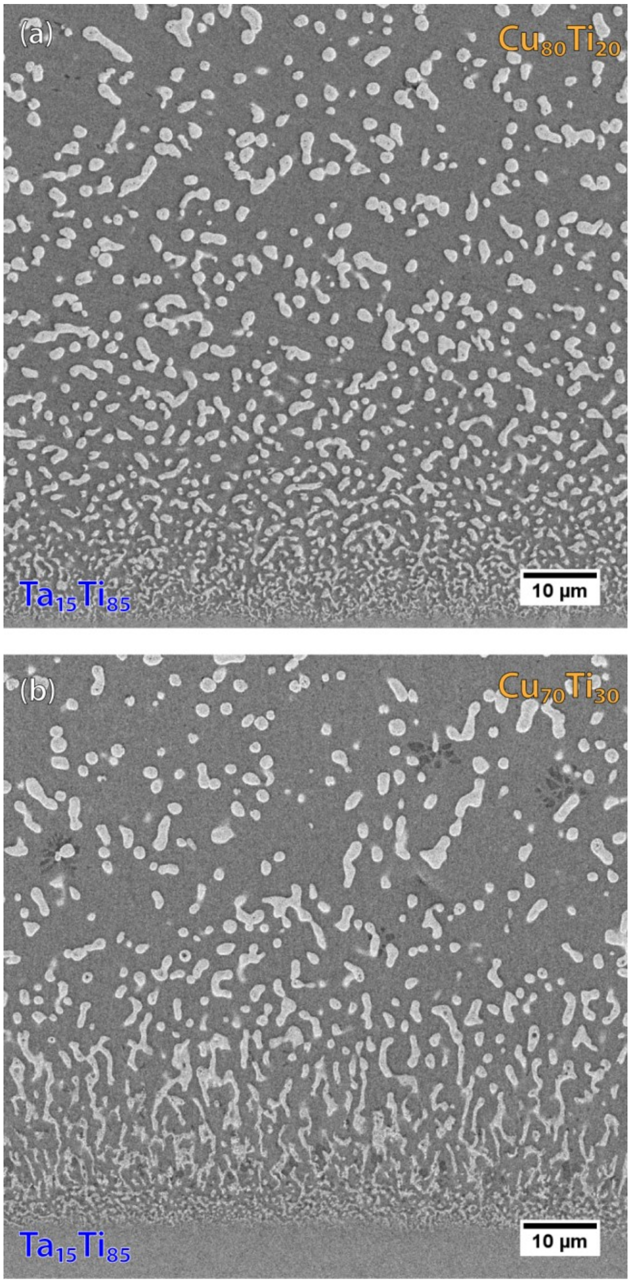

Figure 3-2: SEM micrographs of the cross section of $Ta_{15}Ti_{85}$ samples dealloyed in $Cu_{80}Ti_{20}$ (a) and $Cu_{70}Ti_{30}$ (b) where dealloying occurred from top to bottom on the image, that show a transition from a porous Ta structure near the dealloying interface (bottom) to disconnected droplets of Ta near the top. Ta near the original surface of the sample dissolved completely.

disconnected droplets of Ta. A side-effect of increasing the Ti fraction in the melt is the dissolution of Ta from the sample due to the liquid phase miscibility of Ta and Ti. The total width of the sample decreased significantly over the 10 second duration of the

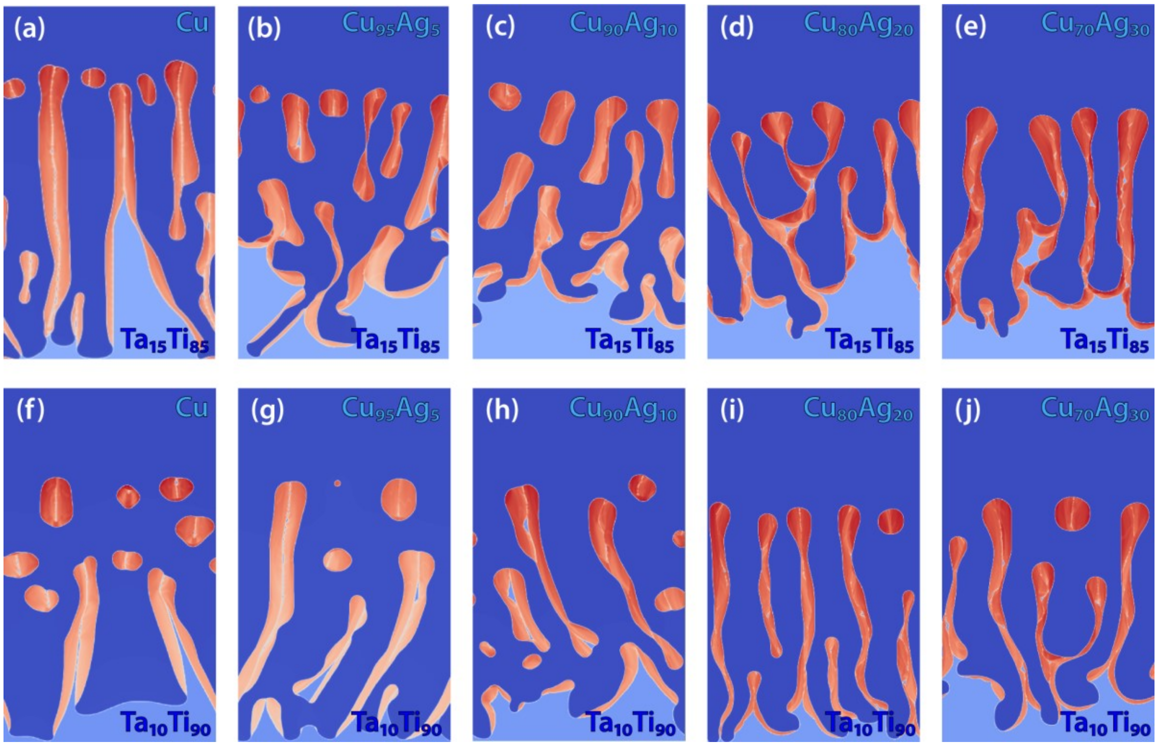

Figure 3-3: Snapshots of two-dimensional phase field simulations for a $Ta_{15}Ti_{85}$ (top) and $Ta_{10}Ti_{90}$ (bottom) dealloyed in Cu-Ag binary liquids with increasing Ag fraction from left to right, showing the evolution of the morphology formed from disconnected droplets to a bifurcating lamellar structure.

experiment, with approximately 200 micrometers dissolving from the surface of the sample in $Ti_{20}Cu_{80}$ melt, and approximately 400 micrometers dissolving in $Ti_{30}Cu_{70}$. This secondary dissolution of Ta may also lead to the disconnection of the initially bicontinuous structure observed in these samples.

The dissolution of Ta limits the applicability of Cu-Ti binary melts to form LMD materials. Ti melts are also highly reactive, presenting additional processing challenges. Rather than adding significant Ti to the melt, another way to decrease the driving force for dealloying is to dilute the melt with a component in which Ti does not dissolve to decrease the total solubility. Ideally this component would also be immiscible with Ta to mitigate the dissolution seen above. For this system, silver was selected because it is conveniently miscible with Cu, immiscible and unreactive with Ta, and has a maximum Ti solubility of only 15 at. %. For simulations, rather than adding silver as an additional component, the simulated CuAg mixture was assigned an overall solubility of Ti and was otherwise treated similarly to pure Cu. To change the silver fraction, the Ti solubility was approximated as a weighted average of the solubilities in Cu and Ag. The results of these simulations are shown in **Figure 3-3** for both $Ta_{15}Ti_{85}$ and $Ta_{10}Ti_{90}$ starting alloys. Between 10 at. % and 20 at. % Ag in the $Ta_{15}Ti_{85}$ alloy there is a clear change from a structure with disconnected blobs to one where the ligaments remain connected. In $Ta_{10}Ti_{90}$, a similar occurs between 20 at. % and 30 at. % Ag.

Experimentally, the observed structure near the dealloying interface is different when reducing Ti solubility by adding Ag to the Cu melt compared to the scenario above where Ti was pre-added to the melt. Rather than uniform rounded ligaments, plates of Ta-rich solid form. As the sample continues to dealloy, more Ti dissolves from these plates until a structural transition occurs where they break up into a rounded structure with a relatively low volume fraction filled by Ta ligaments (**Figure 3-4**). The solidified CuAg can be dissolved chemically, excavating the Ta structure, which even more clearly illustrates the morphology evolution from the plate-like angular structure observed near the interface to a rounded porous structure, and demonstrates conclusively that the latter structure is composed of a connected network of ligaments that remains mechanically robust even when freestanding. In this case, the area containing Ta ligaments extends the full width of the original sample, so Ta dissolution did not result in the loss of significant material.

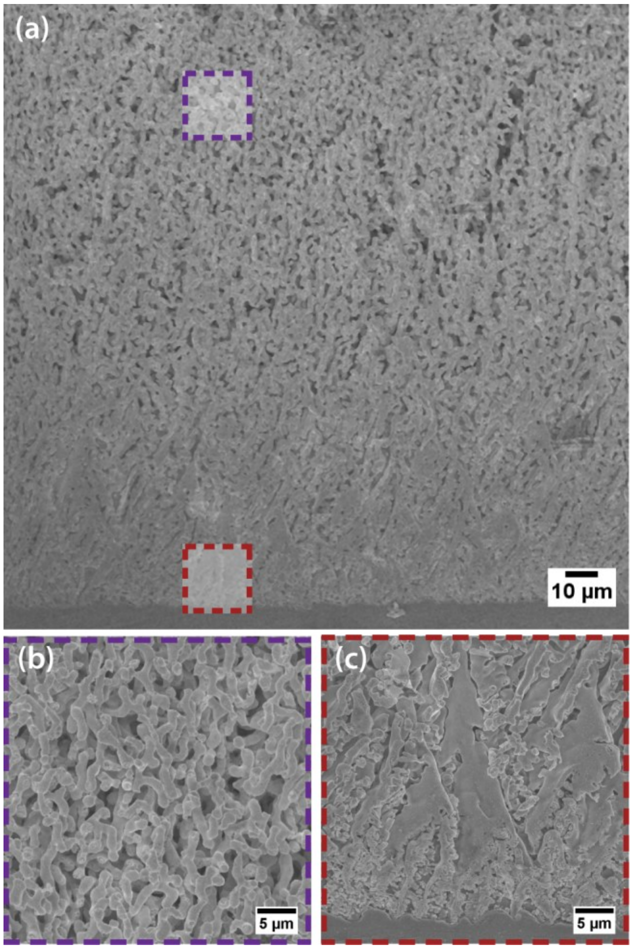

Figure 3-4: SEM micrograph of the cross section of a $Ta_{15}Ti_{85}$ sample dealloyed in $Cu_{70}Ag_{30}$ where the Cu-rich phase has been etched away after dealloying revealing the details of the three-dimensional structure formed. After dealloying, a structural transition occurs approximately 100 micrometers from the dealloying interface (a) where the structure changes from the porous structure near the surface (b) to a denser, angular structure near the dealloying interface.

Both sets of simulations shown above show a transition from the dissolution of linear channels to a more complex structure where the channels preferentially form more complex geometries instead, and in each case the analogous experiment shows a change from a dealloyed structure featuring separated solid domains to one with an interconnected network of solid ligaments. This connectedness transition is important because bicontinuous structures combine important properties including high interfacial area with mechanical integrity that are key selling points for new dealloyed materials. As

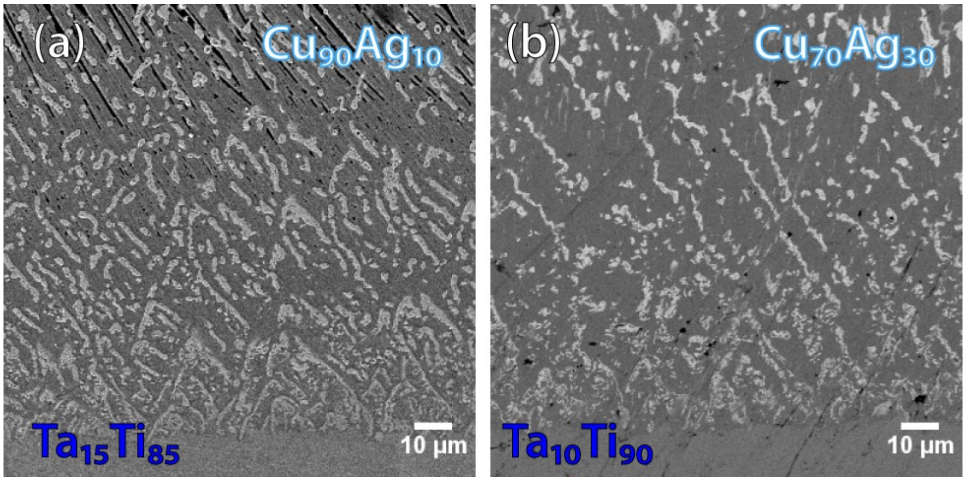

Figure 3-5: SEM micrographs of cross sections taken from $Ta_{15}Ti_{85}$ dealloyed in $Cu_{90}Ag_{10}$ (a) and $Ta_{10}Ti_{90}$ dealloyed in $Cu_{70}Ag_{30}$ which show the same angular structural features near the dealloying interface at the bottom of each image.

discussed above, the formation of such structures is based on the bifurcation of pores to create geometric complexity, and in the simulations here, pore bifurcation is observed in both types of bimetallic bath.

Based on this observation, the simulations in **Figure 3-3** suggest that structurally connected morphologies are accessible at even lower initial Ta fraction by further reducing the driving force. Simulations with 10 at% Ta starting alloy require much more Ag in the bath to form a similar structure, but in **Figure 3-3** (d) and (j) both begin to display pore bifurcation. This similarity in the analogous experimental structures is demonstrated in **Figure 3-5**, where the two starting alloys result in very similar structure near the dealloying interface at the lower edge of the images. However, further from the dealloying interface the structures are notably different owing predominantly to the different fraction of solid component. While phase field modeling is a powerful tool for predicting initial behavior during LMD, this highlights an important drawback. Due to the short time scale of the simulation, it does not entirely address post-dealloying coarsening that begins to dominate structural evolution during the longer time frame of the experiment. This coarsening behavior is complex and the active coarsening mechanisms can change based on the volume fraction and connectedness of the solid phase.

At short time scales, efficient 2-D phase field simulations have successfully predicted changes in the structure of dealloyed Ta in two types of binary metallic bath. In each case, a starting alloy that had previously formed a disconnected final structure was shown experimentally to form a bincontinuous ligament structure in a bath composition regime where the simulation showed the bifurcation of liquid channels in the solid. By reducing the fraction of Ta in the starting alloy, the final structure contains a greater fraction of void space than previous LMD materials, which can be important for applications where flow through the porous structure is required. The more open pore structure leaves more space for coatings or other post processing of the material.

3.4 Conclusion

The future applicability of porous materials depends on the ability to design materials within a specific set of parameters. In dealloying, and LMD in particular, properties such as length scale, depth of dealloying, and volume fraction of ligaments are all mutually dependent primarily on the processing time and temperature. However, by understanding the interaction between solid and liquid composition that controls the structural evolution during LMD, an additional control variable is introduced which, in this case, allows the volume fraction of the final material to vary independently of time and temperature, and beyond the constraints imposed previously by the composition of the starting alloy. The small scale two-dimensional phase field models used here can be efficiently employed to probe a large variable space while still providing valuable insight to guide more detailed experimental studies.

3.5 References

[1] W. J. Boettinger, J. A. Warren, C. Beckermann, and A. Karma, “Phase-Field Simulation of Solidification,” *Annu. Rev. Mater. Res.*, vol. 32, no. 1, pp. 163–194, 2002.

[2] L.-Q. Chen, “Phase-Field Models for Microstructure Evolution,” *Annu. Rev. Mater. Res.*, vol. 32, no. 1, pp. 113–140, 2002.

[3] P. A. Geslin, I. McCue, B. Gaskey, J. Erlebacher, and A. Karma, “Topology-generating interfacial pattern formation during liquid metal dealloying,” *Nat. Commun.*, vol. 6, pp. 1–8, 2015.

[4] I. McCue, B. Gaskey, P. A. Geslin, A. Karma, and J. Erlebacher, “Kinetics and morphological evolution of liquid metal dealloying,” *Acta Mater.*, vol. 115, pp. 10–23, 2016.

[5] T. Wada, K. Yubuta, A. Inoue, and H. Kato, “Dealloying by metallic melt,” *Mater. Lett.*, vol. 65, no. 7, pp. 1076–1078, 2011.

[6] T. Wada and H. Kato, “Three-dimensional open-cell macroporous iron, chromium and ferritic stainless steel,” *Scr. Mater.*, vol. 68, no. 9, pp. 723–726, May 2013.

4 A Model for Rapid Coarsening During Liquid Metal Dealloying

4.1 Introduction

An important part of engineering any nano- or microstructured functional material is control over the length scale of its microstructural features [1]. In dealloying, a common process to make porous metal materials by selective removal of a component from an alloy, the microstructure always initially forms at a fine nm length scale [2]. The primary control over length scale comes from post-dealloying processing, which increase feature sizes via coarsening. Like other porous materials, dealloyed metal structures are inherently metastable owing to their large surface area. While they can be stable for long periods near room temperature, porous samples will always coarsen rapidly when heated sufficiently.

In general, electrochemically dealloyed samples are made by etching the less noble component out of a binary alloy chemically or by applying an electrical potential to cause it to dissolve. During dissolution, the remaining components reorganize into a bicontinuous structure of interconnected pores and ligaments with a relatively narrow distribution of sizes. A specified larger length scale can be reached by removing samples from the electrolyte and heated treating at a specified time and temperature until the sufficient thermal coarsening has taken place. As dealloying has become an increasingly popular processing tool, the length scale dependence of a variety of properties has been studied. Much of the work on dealloyed materials has centered on nanoporous gold dealloyed from silver-rich binary alloys [3]. As a model system for other randomly assembled porous solids, the feature size-dependent mechanical properties of nanoporous gold have been studied by several groups [4,5]. To study size effects in detail, the mechanisms of formation and coarsening in electrochemically dealloyed nanoporous metals has been thoroughly investigated. The formation of porosity and the coarsening process are both mediated by surface diffusion [6]. The mobility of atoms in bulk alloy samples at room temperature is negligible for most metals, but lower coordination surface atoms are much more freely able to move along the interface between the solid and the electrolyte, and anion adsorption from electrolyte can significantly reduce the activation barrier for surface diffusion. This surface mobility is the critical factor that allows nanoporous structures both to form and coarsen. The theory of coarsening in electrochemically dealloyed systems is well-developed and supported by both atomistic simulations and experiments [7,8]. Coarsening of these materials also occurs via surface diffusion, with atoms moving preferentially from areas of high curvature to flatter areas, causing smaller ligaments to shrink as larger ligaments grow [9,10]. Eventually, smaller ligaments become unstable and pinch off. These events reduce the local genus, or the number of distinct holes through the structure in a volume, and the disconnected ligaments provide material that redistributes over the surface to grow other ligaments and increase the average of the size distribution.

Recently, attention has shifted towards liquid metal dealloying (LMD), where the selective removal of an alloy component takes place by dissolution in a liquid metal bath driven by dissimilar solubility of the alloy components [11,12]. Due to the elevated temperatures required to melt the metal bath, the kinetics of LMD are quite different than chemical or electrochemical dealloying in aqueous solution. McCue et al. show that dealloying Ta-Ti binary alloys by immersion in molten Cu is rate-limited by diffusion of

Ti away from the dealloying interface in the liquid rather than the Ti dissolution events themselves [13]. LMD can proceed very rapidly, with millimeter-scale samples dealloying in a matter of seconds, meaning LMD promises to produce bulk samples of dealloyed material with efficient processing times. However, the increase in reaction rate is accompanied by increased coarsening kinetics. In fact, samples coarsen rapidly enough that in a cross-section of a single sample, one observes a significant gradient there is a large disparity between feature sizes at the surface of the sample that were dealloyed first, and those near the dealloying interface which reacted close to the end of the experiment, as shown by the cross section in **Figure 4-1** as well as in Reference [13]. Computer simulations can provide additional insight into the initial stages of dealloying, where a surface instability on the length scale of a few nanometers leads to porosity formation, as shown by Geslin and coworkers [14]. This structure must coarsen by several orders of magnitude to form the final structure observed after LMD experiments.

While coarsening is an important tool for controlling the properties of a final material by tuning the feature size distribution, the rapid initial coarsening of features must be mitigated to create large samples with a uniformly fine structure. To efficiently reduce the rate of coarsening relative to dealloying, the links between these two processes must be understood. The kinetics of LMD has been studied in depth, but there is no detailed study of coarsening mechanics specific to LMD, where additional coarsening mechanisms are available due to the nature of the dealloying environment. Electrochemically, it is possible to set dealloying conditions where one element is totally soluble and another is almost perfectly insoluble, either by selecting a chemical environment where one component is stable and another dissolves, or analogously by applying a potential between the reduction potentials of the two elements. This is much more difficult in a high temperature metal bath, as most metals have some small mutual solubility. Even between metals that are known to be immiscible, like Cu and Ta in the example above, liquid phase solubilities are on the order of tenths of a percent — many orders of magnitude higher than the solubility of gold at the critical potential for dissolution of silver in an aqueous solution. When the component that makes up the solid ligaments can dissolve slightly, the ligaments are able to coarsen both by Ostwald ripening, mediated by dissolution/redeposition of the solid phase component, as well as coarsen by surface diffusion.

Here, we use the formation of porous Nb from a Nb-Ti binary alloy in a molten Cu bath as a model system to study the coarsening of ligaments that occurs in-situ during the dealloying process. By combining contributions from surface and liquid phase diffusion that account for the solubility of each component in the bath, a model is presented that includes both Ostwald ripening and surface diffusion to explain the rapid initial coarsening observed during LMD of niobium but remains consistent with previous coarsening observations in LMD tantalum materials.

4.2 Experimental Methods

To make the precursor alloy for dealloying, Nb (99.9%) and Ti (99.95%) evaporation pellets (Kurt Lesker) were melted using induction heating with an Ambrell45kW Ambrell Ekoheat ES induction system with a water-cooled cold crucible purchased from Arcast, Inc. (Oxford,ME). The resulting ingots of $Nb_{30}Ti_{70}$ and $Nb_{40}Ti_{60}$ were annealed at 2000 °C for 8 hours to allow grain growth and ensure homogeneity.

Both melting and heat treatment were conducted under an atmosphere of flowing purified Ar. The ingot was then sectioned using a diamond wafering saw and the cross section observed to confirm the presence of a single phase alloy. Pieces from these master ingots was prepared for dealloying by spot welding to a Ta wire. A 40 g piece of Cu was fully melted by induction heating in a machined boron nitride crucible, and allowed to equilibrate at 1100 °C for 10 minutes under a flowing Ar atmosphere. The Ta wire holding the sample was clamped to the end of a vacuum manipulator arm and lowered into the Cu bath for the specified experimental time, after which it was removed by retracting the manipulator arm and allowed to cool naturally in Ar. The Cu used for LMD was grade 101 (> 99.99% Cu) purchased as rods (McMaster-Carr). Samples were then cross sectioned using a diamond wafering saw, and mechanically polished before imaging on a JSM-6700F equipped with a annular backscattered electron detector. SEM images were rotated so the dealloying interface was parallel to the long edge of the image, then converted to binary. The average width of ligaments in each row of pixels was calculated.

4.3 Results and Discussion

In LMD, the relatively high homologous temperature during the dealloying process means the in-situ coarsening during dealloying has a similar rate as the dealloying rate itself, leading to a broad gradient of feature sizes within a single sample, with small pores and ligaments near the furthest extent of dealloying and significantly larger features near the original surface of the starting alloy where ligaments have been

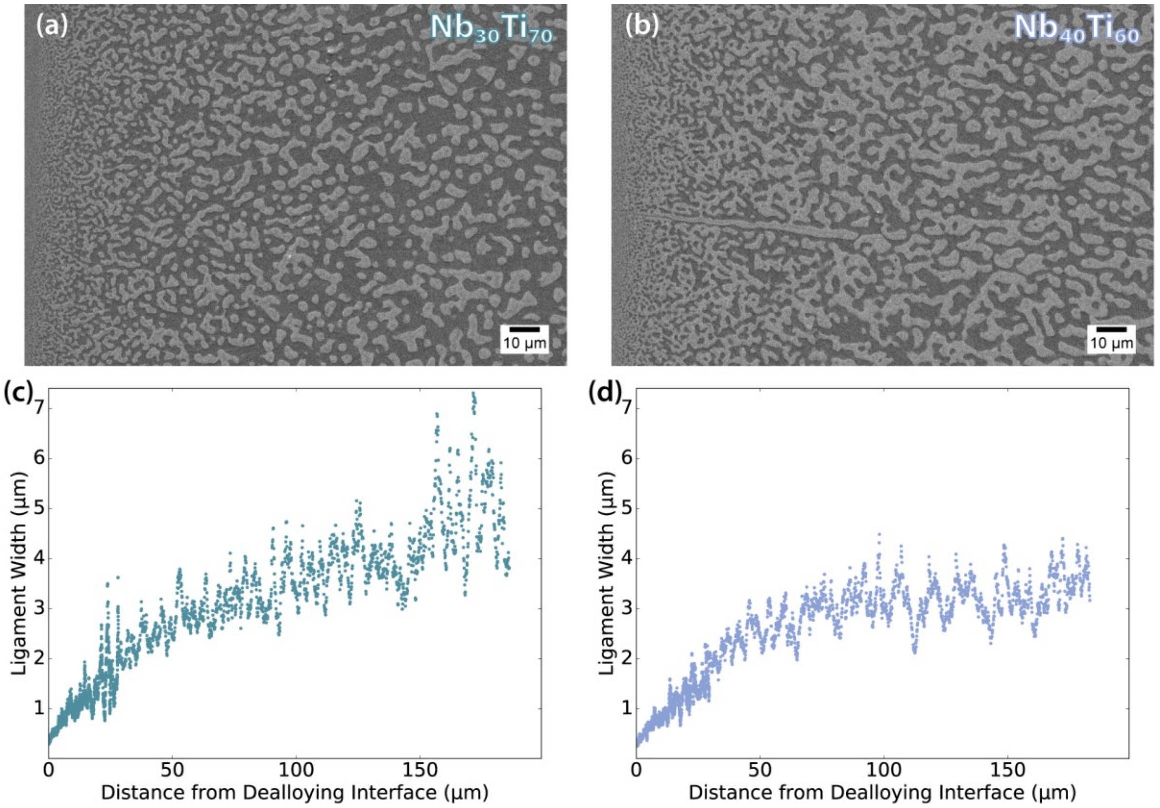

Figure 4-1: SEM images of polished cross sections of LMD composites made by dipping $Nb_{30}Ti_{70}$ (a) and $Nb_{40}Ti_{60}$ (b) in molten Cu at 1100 °C for 60s. Plots of average ligament width as a function of distance from the dealloying interface were generated from sets of similar images for $Nb_{30}Ti_{70}$ (c) and $Nb_{40}Ti_{60}$ (d).

exposed to liquid for the longest time. **Figure 4-1a** shows a cross section in a sample of $Nb_{30}Ti_{70}$ dealloyed for 60 seconds which demonstrates the extent of coarsening during the dealloying process. We can quantify this effect by measuring ligament size distributions at several depths in the same sample and analyze different subvolumes of the sample to understand how the phenomenon of coarsening itself evolves as dealloying progresses.

Our previous work has focused on dealloying Ta-Ti binary alloys, but here Nb was chosen to replace Ta as the immiscible element. Our expectation was that Nb ligaments would coarsen more rapidly than Ta ligaments due to its lower melting temperature, and the consequently higher homologous experimental temperature. Nb alloys with 30 and 40 at. % Nb were chosen. These alloys are near the center of the composition range for which bicontinuous porous structures are expected to form [14]; alloys with Nb fraction below 20 at. % become discontinuous during dealloying, and alloys with more than 55 at. % Nb do not dealloy.

As shown in **Figure 4-1**, samples of each alloy immersed in molten Cu for 60 seconds develop a wide range of feature sizes between the surface and the interior of the sample. Polished cross sections imaged by scanning electron microscopy show two dominant phases in both alloy compositions: a brighter Nb-rich ligament phase, and a darker phase formed by molten Cu which solidified in the pores after the samples were removed from the melt. Two datasets from each sample are discussed in detail: one is taken from images near the dealloying interface which looks specifically at ligaments that were dealloyed in the last 10 seconds of the experiment, and the other was gathered with lower-magnification images and captures much of the overall time evolution of the samples, with time windows up to 40 seconds. Due to the resolution of imaging, this dataset suffers from reduced accuracy near the dealloying interface where features are smallest. The ligament width data were found by thresholding backscattered electron images to separate the Cu-rich pores from the ligaments. The distribution of the width of ligaments was then measured for a line across the image at constant depth in the sample. This gives the ligament size distribution as a function of position in the sample. The two datasets are combined in **Figure 4-1c,d** to show the ligament size continuously from within a micrometer of the dealloying interface across a broad area of the sample. Understanding the temporal evolution of ligament sizes during dealloying is complex. A given depth of dealloyed sample starts coarsening as soon as the dealloying front reaches that depth. However, in LMD, the dealloying rate slows down as the dealloyed depth increases due to diffusion limited transport of Ti out of the pores [13], so the time necessary to dealloy to a depth x in the sample is given by

$$t(x)=\frac{x^2}{a^2}, \tag{1}$$

where a is the rate prefactor. The total experimental time T is the sum of the time necessary to dealloy to a depth and the coarsening time for ligaments at that depth, so we can define the coarsening time τ as

$$\tau(x)=T-t(x). \tag{2}$$

The prefactor a can be calculated from the kinetic data above by substituting the experimental values for the final depth and time into Eq. (1) and using that result in Eq. (2). Transforming the data to express it in terms of time rather than position in this manner leads to the relationship between coarsening time and ligament size shown in **Figure 4-2** for starting alloys $Nb_{30}Ti_{70}$ and $Nb_{40}Ti_{60}$. In general, for electrochemically dealloyed materials, ligament coarsening would be approximately fit by a power law with exponent around 0.25, due to the time dependence of surface-diffusion-mediated ligament pinch-off events that reduce the local genus of the material by removing “handles” or loops [10].

Neither alloy studied here displayed the $t^{1/4}$ power law behavior characteristic of surface diffusion and that we saw in the Ta-Ti system (Chapter 2), which suggests that another mechanism is determining the overall coarsening rate. Ostwald ripening driving by dissolution/redeposition is a common mechanism for the coarsening of features in a

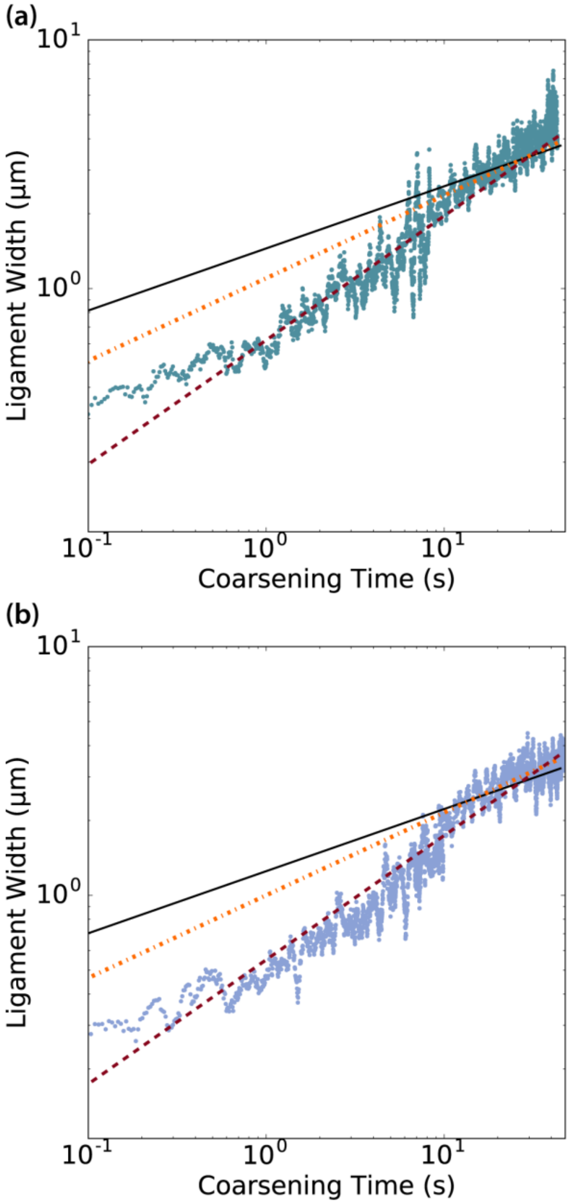

Figure 4-2: Feature size as a function of total coarsening time for $Nb_{30}Ti_{70}$ (a) and $Nb_{40}Ti_{60}$ (b) with power law with exponents of 0.25 (black, solid) associated with surface diffusion-mediated coarsening, 0.33 (orange, dot-dashed) indicative of Ostwald ripening where the overall rate is limited by diffusion kinetics, and 0.5 (purple, dashed) caused by Ostwald ripening where surface attachment and detachment kinetics control the rate of the process.

variety of solid and liquid systems, including metallic melts, colloids, and precipitation-hardened alloys [15,16]. Ostwald ripening has a characteristic time-evolution power law exponent of $t^{1/3}$ when the process is rate-limited by diffusion between ligaments, and an exponent of $t^{1/2}$ when limited by the rate of attachment and detachment of Nb at the ligament surface [17]. As shown in **Figure 4-2**, the coarsening data is best fit associated with surface reaction-limited Ostwald ripening.

LMD coarsening by Ostwald ripening is complicated by the spatial and temporal variation in liquid composition over the course of the LMD process. At the dealloying interface, Ti in the liquid is close to equilibrium with the Ti composition of the solid, and in the liquid bath beyond the outer surface of the sample the Ti concentration vanishes to zero due to convection induced via the RF melting technique used [13,14], which sets a functionally zero Ti concentration boundary conditions outside the sample. The general notion we consider is that Nb is highly miscible in Ti, so when the Ti concentration in the liquid is relatively high (near the dealloying front), the Nb solubility rises enough to drive ripening, whereas where the Ti concentration in the liquid is relatively low (near the geometric surface of the sample), the Nb solubility is low, and coarsening is slow. We reasonably assume that the Nb solubility is proportional to the Ti concentration in Cu, and approximate it as declining linearly from a value of C_L at the dealloying interface ($x = a\sqrt{t}$), given by the equilibrium concentration at the Ti-Cu/Nb interface, to C_0 at the original surface of the sample ($x = 0$). This gives an expression for the Nb concentration as a function of sample depth and time of

$$C(x,t) = C_0 + (C_L - C_0)\frac{x}{a\sqrt{t}}. \tag{3}$$

Figure 4-3 shows the approximated concentration of Ti between the dealloying interface and the original sample surface and the resulting maximum solubility of Nb.

The total coarsening rate is comprised of separate terms, each associated with Ostwald ripening or surface diffusion, the former proportional to Nb solubility and with either a $t^{1/3}$ or $t^{1/2}$ power law time dependence and the latter progressing independent of Nb solubility and proportional to $t^{1/4}$. If we let λ denote the average ligament size, we can differentiate the time dependence of λ for each coarsening mechanism, and add them in parallel to express the total coarsening rate for a given position $k_C(x)$:

$$k_C(x) = k_1 \frac{1}{4} t^{-3/4} + k_2 C \frac{1}{3} t^{-2/3} + k_3 C \frac{1}{2} t^{-1/2}. \tag{4}$$

Here, k_1, k_2, and k_3 are rate prefactors for surface diffusion coarsening, diffusion limited Ostwald ripening, and surface reaction limited Ostwald ripening, respectively, and are constant under the isothermal dealloying conditions. In this analysis, k_2 and k_3 include the proportionality constant between Ti concentration and Nb solubility, so this does not need to be estimated separately. The ligament size at any given point in the sample is calculated by integrating this expression with respect to time for the total duration a given location has coarsened during the experiment given by τ in Eq. (2) above, yielding

$$\lambda(x,T) = \lambda_0 + \int_0^{\tau(x)} k_C dt. \tag{5}$$

Note that the expression for concentration must be rewritten in terms of the dealloying time at a given position x, rather than the total experimental time as in Eq. (3) , by adding the expression from $t(x)$ from Eq. (1). Evaluating this integral gives an

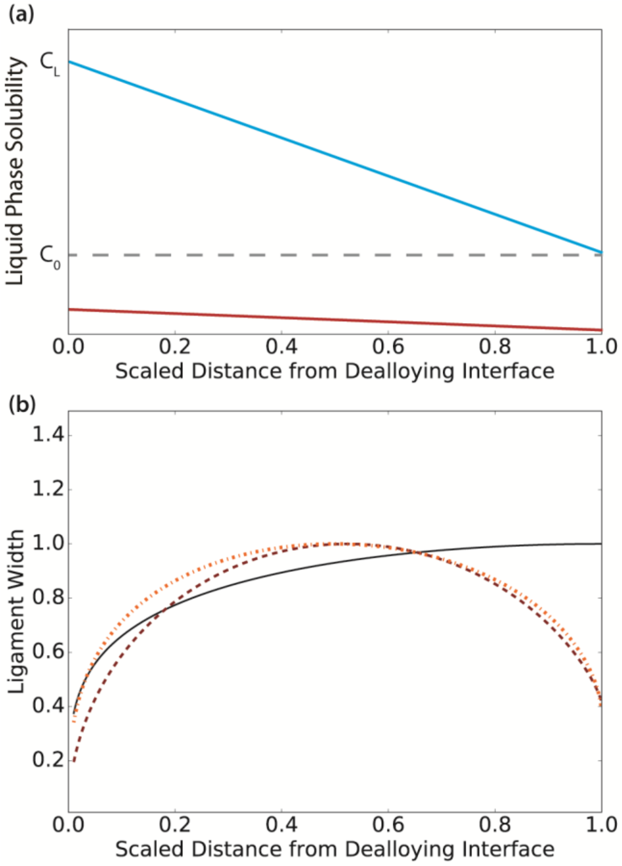

Figure 4-3: A schematic of normalized distance from the dealloying interface (at x=0) to the original surface of the sample (x=1) showing (a) the estimated concentration of dissolved Ti (blue) and the resulting maximum solubility of Nb (red), and (b) the expected size profile for surface diffusion mediated coarsening (black, solid), diffusion limited Ostwald ripening (orange, dot-dashed) and surface reaction limited Ostwald ripening (purple, dashed).

expression for ligament size at any depth in the sample with adjustable parameters k_1, k_2, and k_3, which control the relative rates of surface diffusion, diffusion-limited Ostwald ripening, and surface attachment-limited Ostwald ripening, respectively. This integral can be evaluated exactly in this simple case with a linear concentration profile, but in general must be computed numerically. However, the generic shape of $\lambda(x,T)$ is shown by scaling a and T such that the dealloying time and maximum depth are both 1 and setting all constants to 1. In this case, we can plot these terms separately, as shown in **Figure 4-**

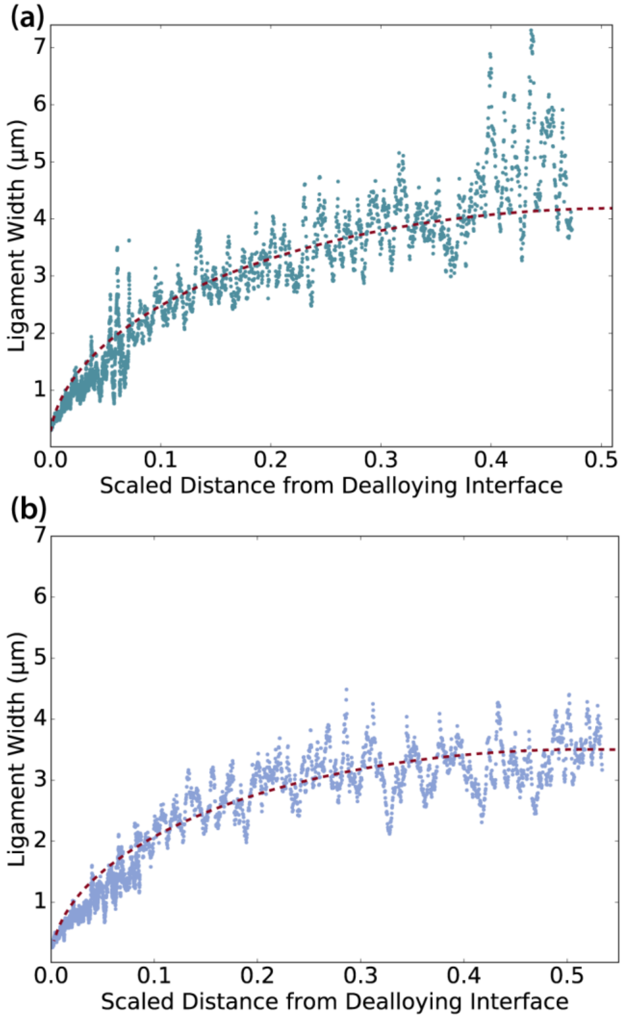

Figure 4-4: Average dealloyed ligament width as a function of position with the dealloying depth scaled so that 0 is the dealloying interface and 1 is the original sample surface. Both datasets showing good agreement with identical fits from surface reaction limited Ostwald ripening model (purple, dashed) for Nb$_{30}$Ti$_{70}$ (a) and Nb$_{40}$Ti$_{60}$ (b) where only the equilibrium Nb solubility has been adjusted to account for sample composition.

3. The k_1 term (black, solid line) is the result of surface diffusion mediated coarsening; it grows monotonically as the distance from the dealloying interface increases.

Surprisingly, our model predicts the feature size curves for Ostwald ripening for either the diffusion limited or surface reaction limited regimes initially increase but then decrease again near the original surface of the sample. This is caused by the consistently low concentration of Ti,near the Cu bath and commensurately small Nb solubility.

To validate this model, we first fit each k_n to the experimental data from **Figure 4-1**. In principle, the coarsening mechanism in a single sample is a linear combination of all three components, but it is likely that either Ostwald ripening or surface diffusion will dominate in a given area in a sample based on the solubility of the solid component in the local liquid. In this case, the term associated with surface-limited Ostwald ripening fits the $Nb_{30}Ti_{70}$ data well, with a prefactor k_3 of 1.5, which is also found by fitting the $Nb_{40}Ti_{60}$ data. It isn't surprising that both data share the same coarsening rate, as they differ only in the dealloying rate parameter a and the equilibrium Ti concentration in the liquid at the dealloying interface. Results of both fits are shown in **Figure 4-4**.

The most interesting feature of this model is the prediction that feature sizes do not increase monotonically as one observes ligaments further from the dealloying interface. At any given time during the experiment, all feature sizes grow at every depth in the sample, but the growth rates near the edge of the sample is sufficiently slow that features in faster-coarsening areas bypass them in size. In a sample of $Nb_{30}Ti_{70}$ dealloyed for 20s, the entire dealloyed depth can be viewed in a single image (**Figure 4-5**). Again, the fit above shows good agreement with the ligament size data over most the dealloyed region, without adjustment of parameters. Ligaments at the outer edge of the sample that dealloyed earliest do appear slightly smaller than ligaments near the center of the dealloyed region (**Figure 4-5**), but the inverted trend in ligament size is not as pronounced as the model predicts. We hypothesize that the reason for this is that our

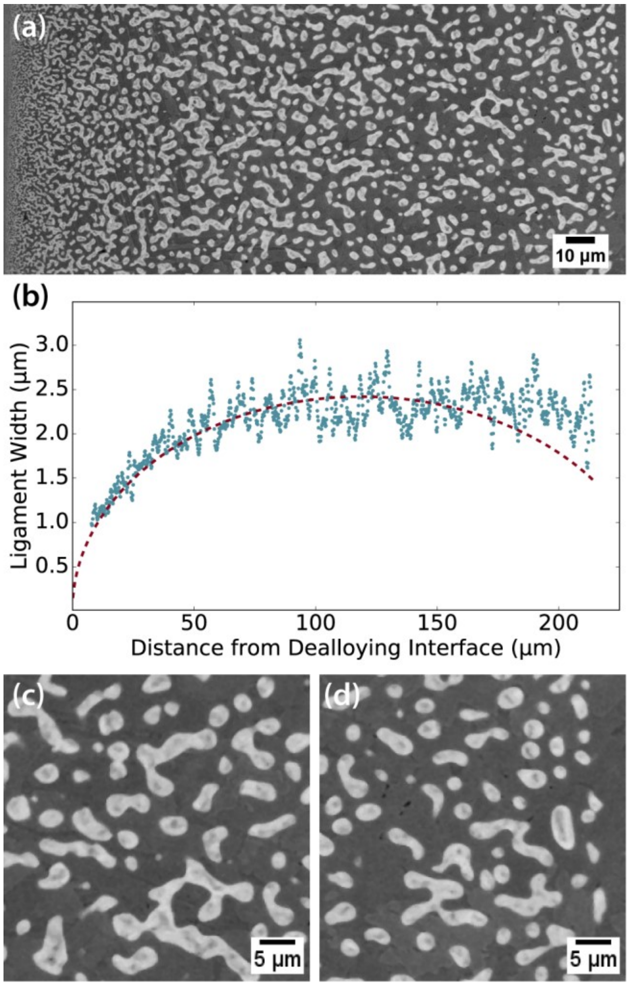

Figure 4-5: SEM micrographs of a region of a $Nb_{30}Ti_{70}$ sample dealloyed for 20s showing a cross section of the entire dealloyed region from the dealloying interface on the left to the original alloy surface at the right (a). Again, the ligament size shows good agreement with the same model used previously. SEM images taken from near the center of the dealloyed region with average ligament area of 7.5 μm^2 (c) and another region near the surface of the same sample where the average ligament area was 6.9 μm^2 (d) illustrate a decrease in ligament size near the original surface where ligaments were dealloying earliest during the experiment.

model ignores diffusion of Nb between ligaments of different depths in the sample, but a driving force for such diffusion does exist due to the concentration gradient cause by the variable solubility. This effect would cause some Nb dissolved from ligaments deeper in the sample to diffuse outwards and redeposit on ligaments closer to the surface. While this would cause ligaments near the surface to grow, this bulk mass transport from one area of a sample to another required by this process makes it distinct from local coarsening.

4.4 Conclusions

We have developed the first model for understanding feature size growth specific to the coarsening processes that samples undergo during LMD. This model accurately predicts feature sizes gradients in systems where some kinetic parameters associated with local coarsening are known. In most dealloyed materials, the region near the surface of the sample which dealloys first and has the longest time to coarsen has the largest final feature size, but our model predicts a feature size profile with a maximum deeper in the sample. Experimental validation supports this result with observations in LMD of Nb-Ti binary alloys in molten Cu.

Coarsening during LMD is an important part of the fabrication process for a variety of composite and porous metal materials. By understanding the mechanisms that drive the rapid coarsening observed during dealloying, steps can be taken to efficiently engineer a specific feature size distribution. In LMD Nb, our model predicts that limiting the Ti concentration in solution, while detrimental to the dealloying rate, could cause a mechanistic shift from Ostwald ripening back to surface diffusion mediated coarsening that keep the final size of the ligaments relatively small.

4.5 References

[1] J. Erlebacher, R. Seshadri, Hard Materials with Tunable Porosity, MRS Bull. 34 (2009) 561–568. doi:10.1557/mrs2009.155.

[2] I. McCue, E. Benn, B. Gaskey, J. Erlebacher, Dealloying and Dealloyed Materials, Annu. Rev. Mater. Res. 46 (2016) 263–286. doi:10.1146/annurev-matsci-070115-031739.

[3] Y. Ding, Y.J. Kim, J. Erlebacher, Nanoporous gold leaf: "Ancient technology "/advanced material, Adv. Mater. 16 (2004) 1897–1900. doi:10.1002/adma.200400792.

[4] H.-J. Jin, J. Weissmüller, D. Farkas, Mechanical response of nanoporous metals: A story of size, surface stress, and severed struts, MRS Bull. 43 (2018) 35–42. doi:10.1557/mrs.2017.302.

[5] N.J. Briot, T.J. Balk, Developing scaling relations for the yield strength of nanoporous gold, Philos. Mag. 95 (2015) 2955–2973. doi:10.1080/14786435.2015.1078512.

[6] J. Erlebacher, M.J. Aziz, a Karma, N. Dimitrov, K. Sieradzki, Evolution of nanoporosity in dealloying., Nature. 410 (2001) 450–453. doi:10.1038/35068529.

[7] J. Erlebacher, An Atomistic Description of Dealloying, J. Electrochem. Soc. 151 (2004) C614. doi:10.1149/1.1784820.

[8] J. Snyder, J. Erlebacher, Kinetics of Crystal Etching Limited by Terrace Dissolution, J. Electrochem. Soc. 157 (2010) S21. doi:10.1149/1.3503042.

[9] J. Erlebacher, I. McCue, Geometric characterization of nanoporous metals, Acta Mater. 60 (2012) 6164–6174. doi:10.1016/j.actamat.2012.07.059.

[10] J. Erlebacher, Mechanism of coarsening and bubble formation in high-genus nanoporous metals, Phys. Rev. Lett. 106 (2011) 1–4. doi:10.1103/PhysRevLett.106.225504.

[11] T. Wada, K. Yubuta, A. Inoue, H. Kato, Dealloying by metallic melt, Mater. Lett. 65 (2011) 1076–1078. doi:10.1016/j.matlet.2011.01.054.

[12] T. Wada, H. Kato, Three-dimensional open-cell macroporous iron, chromium and ferritic stainless steel, Scr. Mater. 68 (2013) 723–726. doi:10.1016/j.scriptamat.2013.01.011.

[13] I. McCue, B. Gaskey, P.A. Geslin, A. Karma, J. Erlebacher, Kinetics and morphological evolution of liquid metal dealloying, Acta Mater. 115 (2016) 10–23. doi:10.1016/j.actamat.2016.05.032.

[14] P.A. Geslin, I. McCue, B. Gaskey, J. Erlebacher, A. Karma, Topology-generating interfacial pattern formation during liquid metal dealloying, Nat. Commun. 6 (2015) 1–8. doi:10.1038/ncomms9887.

[15] P.W. Voorhees, The theory of Ostwald ripening, J. Stat. Phys. 38 (1985) 231–252. doi:10.1007/BF01017860.

[16] P.W. Voorhees, Ostwald ripening of two-phase mixtures, Annu. Rev. Mater. Sci. 22 (1992) 197–215. doi:10.1146/annurev.ms.22.080192.001213.

[17] C. Wagner, Ostwald ripening theory, Ber. Bunsenges. Phys. Chem. 65 (1961) 581–591.

5 Self-Assembled Metal-Metal-Ceramic Nanocomposites via Liquid Metal Dealloying

A major challenge in the synthesis of high surface area metals via subtractive processes such as dealloying has been to maintain the mechanical integrity of the resulting structures. This problem is especially apparent in liquid metal dealloying (LMD), in which selective dissolution from an alloy leading to porosity formation takes place in a molten metal bath at elevated temperatures. In this work, we show that addition of small amounts of silicon to parent alloys of NbxTi1-x leads to generation of a self-assembled array of niobium silicide plates during LMD, merged with the usual bicontinuous porous structure seen in dealloying. This ceramic phase passes through grain boundaries and holds the polycrystalline bicontinuous niobium network intact to form a multi-component, multi-phase metal-metal-ceramic nanocomposite. Kinetic analysis shows that the growth of the silicide phase does not strongly affect the structural evolution of the metal-metal bicontinuous morphology, simultaneously developing during LMD. Dissolving one metal phase from the composite yields a mechanically robust porous metal-ceramic composite, which can be further processed to form a variety of tertiary materials via re-impregnation of a new third phase. The materials design strategy introduced here can be generalized, serving as a platform to form dense metal-metal-ceramic nanocomposites.

5.1 Introduction

Dealloying is commonly used to produce high-surface area metal materials by selective removal of one component from an alloy, creating an open bicontinuous porous network of the remaining alloy components, useful for applications such as catalysis where high surface area is desired [1,2]. Most commonly, dealloying is driven by electrochemical corrosion of a less noble component from an alloy in aqueous solution [3], but a recent innovation has been to replace this aqueous solution with a molten metal bath. In this technique - liquid metal dealloying (LMD) – an alloy is placed in contact with a molten metal bath selected such that one component dissolves readily while the other remains insoluble. Wada et al. first demonstrated LMD in 2011 dealloying TiCu alloys in molten Mg, producing porous Ti [4]. In our group, we have used LMD to form porous refractory X-Cu metal-metal composites from Ti-X (X = Ta, Nb, W) alloys immersed in molten Cu [5].

LMD has several notable characteristics compared to electrochemical dealloying. First is a much larger temperature range accessible to molten metals for LMD compared to water-based solutions. Higher temperatures increase the kinetics of the dealloying process, so macroscopic (cm^3) volumes can be dealloyed in a matter of seconds or minutes instead of days. The range of available metal "solvents" has also widened the number of metals that can be rendered porous by LMD. Many of the noble metals commonly dealloyed electrochemically have limited applications dictated by scarcity and price. Materials made by LMD now include many less noble metals that are easily oxidized in aqueous solution and refractory metals with insufficient surface diffusivity to allow dealloying to progress near room temperature [6], and we expect to see the number and utility of these materials to rise as new protocols are developed for LMD.

A fundamental point applicable to both dealloying methodologies is that the feature size of a dealloyed material at a given processing temperature decreases as the melting point of the metal increases [7]. Many elements cannot be dealloyed in aqueous solution simply because their melting points are too high; the observed correlation between ligament size and melting point predicts a ligament size smaller than an atomic dimension. This places an upper limit on the melting point of porous metals that can be dealloyed electrochemically, with the corollary that if a porous metal can be made by electrochemical dealloying, it will be susceptible to coarsening at modest temperatures because the temperature dependence of the coarsening rate scales with the melting point of the metal. This effect can be observed by comparing data from electrochemically dealloyed nanoporous gold [8,9], nanoporous copper [10] and nanoporous platinum [11].

The product material from LMD is a fully dense composite with the liquid phase having solidified in the free space left by dissolution, such as the Mg-Ti composites studied previously by Kato's group [12]. The solidified liquid phase can subsequently be removed chemically, leaving an open porous network such as those commonly found after electrochemical dealloying. When the parent alloy is a solid solution and no phase change is required during dealloying, this network can be single crystalline in the sense that the grains of the solid parent alloy, along with their crystallographic features, are preserved in the ligaments of the material after dealloying, with the pores appearing within individual grains of the starting material [13]. The preserved grains of dealloyed materials distinguishes their microstructure from porous materials made by loosely sintering nanoparticles into a porous network, where grain boundaries from interparticle interfaces are an unavoidable and energetically unstable feature of the resulting material. As a result, the grain size (and associated microstructural properties) should be tailorable separately in advance of dealloying. Crystallographically, this process where the starting alloy is a solid solution is distinct from dealloying when there is a simultaneous phase change. Notable examples of the latter include dealloying ordered intermetallics where the original crystal structure requires all starting components [14], or metallic glasses where recrystallization occurs during dealloying to form nanocrystalline ligaments [15,16]. Porous Nb has previously been prepared via LMD of a Nb-Ni binary alloy, where multiple intermetallic compounds form [17,18], but this work features Nb prepared from a solid solution alloy and so has a structure devoid of intraligament grain boundaries.

During LMD of polycrystalline samples, the coarsening of the feature size in the bicontinuous microstructure tends to cause each individual grain to contract slightly towards its center of mass to reduce the total surface energy. This slight contraction physically detaches the original grain boundaries of the material, as shown in Error! Reference source not found.. McCue et al show that this effect leads to a composite that fails readily in tension, limiting the structural application of LMD composites [19]. More problematically, when the solidified liquid phase is excavated when making a porous material, the grains become physically separated, leaving a powder of porous individual grains (see Error! Reference source not found.) rather than a mechanically robust bulk porous sample.

In this work, we present a materials design strategy to mitigate the effects of grain boundary detachment during LMD, leading to the synthesis of mechanically robust bulk coarse grained porous refractory samples for the first time. Our material design strategy is to add a small amount of a ternary component to the parent alloy, such that during dealloying a “scaffold network” grows along with the bicontinuous structure that hold the

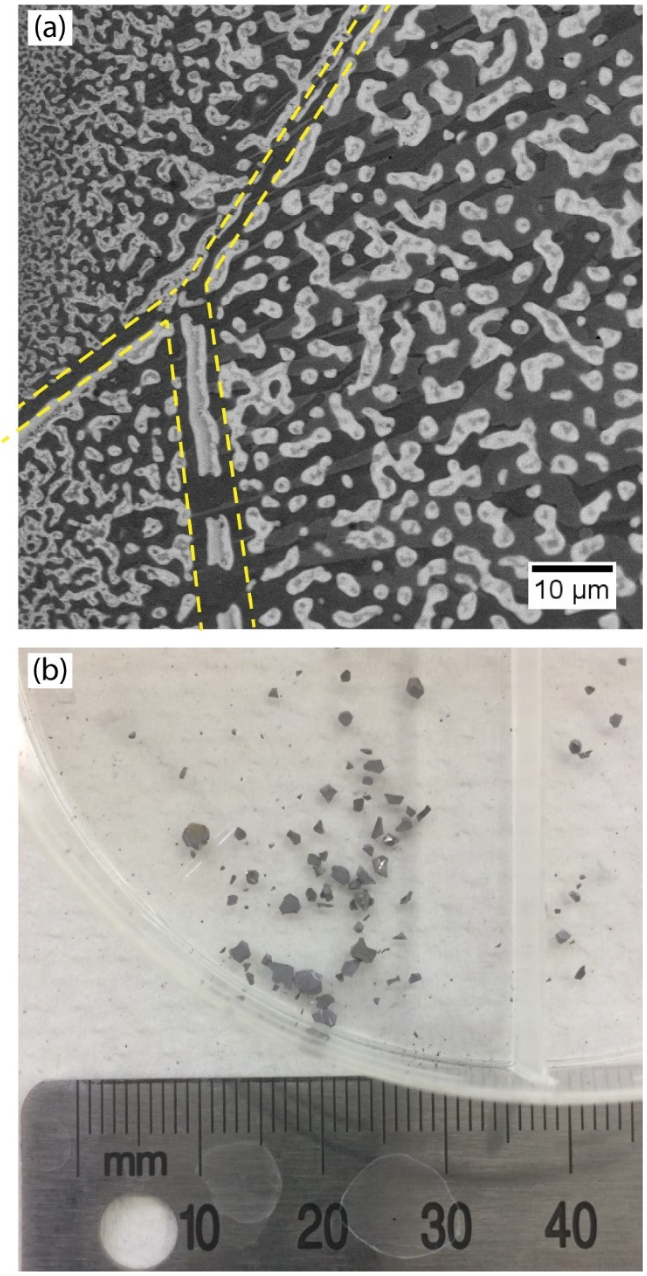

Figure 5-1: (a) Backscatter SEM micrograph of a polished cross section of porous Nb fabricated by liquid metal dealloyed of a $Nb_{30}Ti_{70}$ ingot. The dashed yellow lines highlight areas where grain boundaries have separated, leaving a unbroken volume filled by the darker solidified copper phase. (b) Upon dissolution of the Cu phase, the grains of a polycrystalline ingot fall apart, as shown in the photograph.

grains together. We demonstrate the idea using Nb-Ti with small amounts of Si added.

When dealloyed in copper, dissolving silicon reacts with niobium, precipitating as a

Nb_5Si_3 refractory silicide network during dealloying. We present details of the kinetics of LMD of Nb-Ti (Si) in Cu and characterize the structure of both the fully dense silicide-reinforced three-phase composites and the freestanding porous Nb/Nb_5Si_3 composites formed after dissolving the copper solvent phase. Because the freestanding porous composite is mechanically robust (in the sense that it is dimensionally stable and doesn't fall apart when the copper phase is removed), novel post-treatment pathways have become available. We demonstrate one of these by filling the free space in our porous composite with borosilicate glass to make a metal-ceramic-glass ternary composite. There are many composites that should be formable in this manner have and we think that the class of materials we introduce here have applications as capacitors, structural materials, supports for catalysts, and backbones for new porous materials via coating or other post-treatment.

5.2 Experimental

Alloy Preparation: All alloys used in this study were prepared by induction melting of pure metal pellets purchased from Kurt J. Lesker in a 45kW Ambrell Ekoheat ES induction system with a water-cooled cold crucible purchased from Arcast, Inc. (Oxford,ME). All samples were melted several times to guarantee total mixing, then heat treated to within 10% of their respective melting points for 8 hours to ensure homogeneity. Both induction melting and heat treatment were performed under an atmosphere of flowing purified Ar. After heat treatment, the ingots were sectioned and polished. The presence of homogeneous single-phase alloys was confirmed by scanning electron microcopy (SEM) and X-ray diffraction (XRD).

Liquid Metal Dealloying: LMD experiments were performed by melting copper in a machined boron nitride ceramic crucible under a flowing argon atmosphere using an Ameritherm Easyheat 4kW induction power supply. Forty grams of Cu was heated at high power until fully molten, then the heating power was reduced to allow the bath to equilibrate at 1100 ºC for 5 minutes, with the temperature monitored by optical pyrometer. Samples were cut from alloy ingots prepared as above, spot welded to a Ta wire, and suspended from a vacuum manipulator arm. Once the molten Cu was prepared, the sample was immersed in the bath for the requisite time for the experiment, then removed and cooled. Note that the sample mass is small relative to the copper melt and did not affect the temperature of the melt during dealloying.

Dissolution of the Cu phase: After LMD, the Cu phase solidifies in the pores forming a dense composite. To excavate a porous Nb structure, a redox etchant was prepared by dissolving 10g of $CuCl_2$ (99%, dihydrate salt, Sigma Aldrich) in 50 mL of 5M HCl solution (ACS reagent grade, Fluka). The samples were immersed in this solution overnight (8 hours) to completely dissolve Cu, then rinsed in deionized water and sonicated for one minute to remove solidified residual Ti, disconnected sections of the porous structure, and other debris on the surface.

Characterization and Materials: SEM observations were performed on a JEOL JSM-6700F with EDS and backscatter detectors. X-ray diffractometry was carried out on a Phillips PANalytical X'pert PRO diffractometer using Cu K-α radiation. Ti and Nb were purchased as evaporation pellets from Kurt J. Lesker. Ti purity was 99.995% (metals basis, by weight) and Nb purity was 99.9%. Si purity was 99.9999% purchased

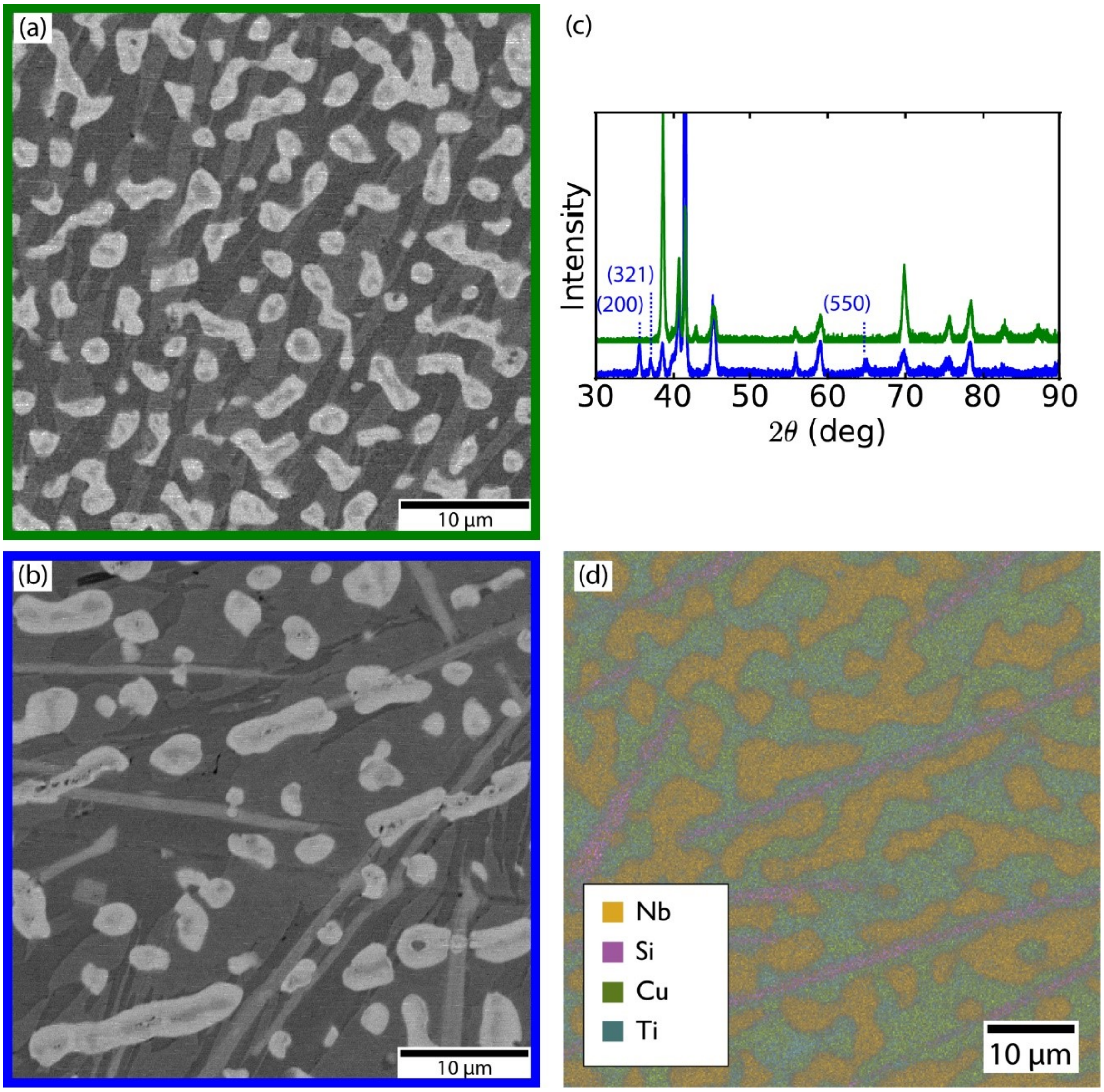

Figure 5-2: (a) Backscattered SEM image of a cross-section of porous Nb (lighter phase) with solidified Cu from the LMD bath filling the remaining volume formed by dealloying $Nb_{30}Ti_{70}$ in molten Cu. (b) When a small amount of Si is added to the starting alloy to make $Nb_{30}Ti_{67}Si_3$, an additional niobium silicide phase, Nb_5Si_3 is formed during dealloying (intermediate contrast phase). (c) X-ray diffractometery shows additional peaks associated with the silicide phase (in blue) while retaining all the major peaks associated with phases in the original composite. (d) The high aspect ratio of the silicide phase is highlighted by EDS mapping of the same sample as (b).

from Alfa Aesar, and the Cu used for LMD was grade 101 (>99.99% Cu) purchased as rods from McMaster-Carr.

5.3 Results and Discussion

Structural Evolution: Homogeneous, single phase starting alloy ingots were prepared by induction melting. Sections from these ingots were immersed in Cu at 1100°C for 20 seconds to dealloy them, and the resulting samples were cross sectioned and polished to reveal the structure formed during LMD. **Figure 5-2** shows the general structure of the composites resulting from LMD of $Nb_{30}Ti_{70}$ and $Nb_{30}Ti_{67}Si_3$ in Cu. SEM of these cross sections shows a brighter Nb phase and a darker Cu phase, with each phase forming a connected porous structure. Contrast variation in the Cu phase is due to uneven distribution of the dissolved Ti during solidification of the liquid after the experiment has concluded. In the Si-containing sample, the intermediate-contrast phase is Nb_5Si_3, as shown more clearly by EDS mapping. X-ray diffractometry shows that the major phases present in the dealloyed $Nb_{30}Ti_{70}$ sample all remain unchanged with the addition of silicon to the parent alloy, but additional peaks appear which match the niobium silicide. The cross sections in **Figure 5-2** were obtained by polishing a surface parallel to the original surface of the parent alloy, such that the dealloying reaction is progressing into the page. Further structural information is available by examining a perpendicular cross section, as shown in **Figure 5-3,** where the dealloying direction goes from the top to the bottom of the image. A gradient in feature size is visible, with the ligaments near the dealloying interface at the bottom of the image visibly finer than those that had dealloyed earlier in the experiment. The plates of silicide remain visible, but from this direction they are much longer than in the previous image, indicating that they form two-dimensional plates where the longer of the two dimensions is perpendicular to the original surface of the sample and parallel to the axis of dealloying.

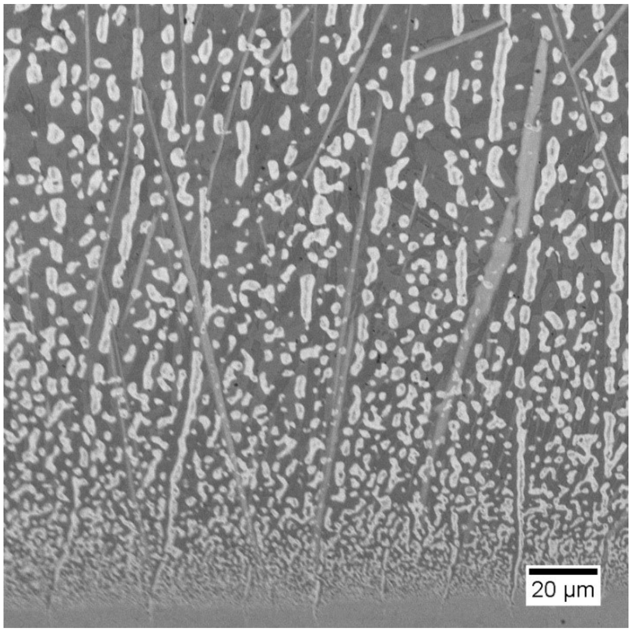

Figure 5-3 SEM microgaph of dealloyed $Nb_{30}Ti_{67}Si_3$ from a cross section taken such that the dealloying direction is downwards in the image. The bottom of the image is parent alloy that has not yet been dealloyed. The Nb5Si3 silicide plates extend vertically in the same axis as the dealloying.

The LMD behaviors of other compositions of Nb-Ti-Si ternary alloy were also tested. Alloys with more than 3% Si added did not form a single solid solution phase even after heat treatment, instead containing stable precipitates of Ti_5Si_3, while addition of less than 2% Si produced no effect. For the remainder of experiments discussed here, we focus on the samples with 3% Si, because these samples showed the largest effect of Si addition while maintaining the phase behavior of the binary Nb-Ti alloy. The ratio of Nb in the initial alloy can also be altered. Geslin et al. showed that this starting composition changed the final morphology in phase field simulations of LMD on Ta-Ti binary alloys [20]. In that system, a continuous network of porous Ta ligaments was formed by starting alloy compositions with as little as 25% Ta. At compositions lower in Ta, a lamellar structure with disconnected Ta-rich plates forms like in classical eutectic

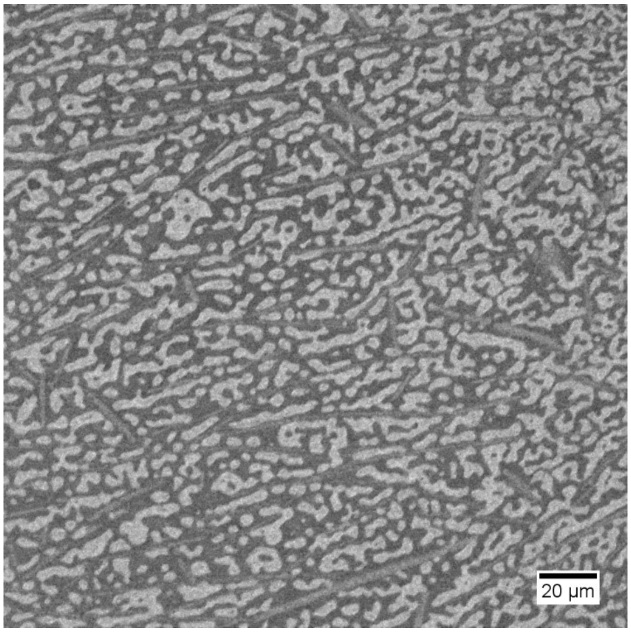

Figure 5-4 SEM cross section of porous Nb prepared from $Nb_{40}Ti_{57}Si_3$. The structure has a much denser network of Nb-rich ligaments than the cross section in **Figure 5-3**.

solidification. Binary Nb-Ti alloys should behave the same way, but there is the question of whether addition of Si alters this limit for structural stability. Because niobium silicide is forming during dealloying, some Nb must be removed from the ligament structure. Furthermore, due to the directionality of the silicide plates, they do not necessarily help hold individual ligaments together. If the 3% Si added to the starting alloy react entirely to make silicide, up to 5% Nb from the initial alloy could be consumed, which would place the $Nb_{30}Ti_{67}Si_3$ alloy near the limit for connectedness. An alloy further from this limit, $Nb_{40}Ti_{57}Si_3$ can also be dealloyed, and a representative cross section is shown in **Figure 5-4**. There is a visible difference in the overall morphology; the Nb ligaments in the Nb-poorer composite (**Figure 5-3**) appear to extend more in the direction of the

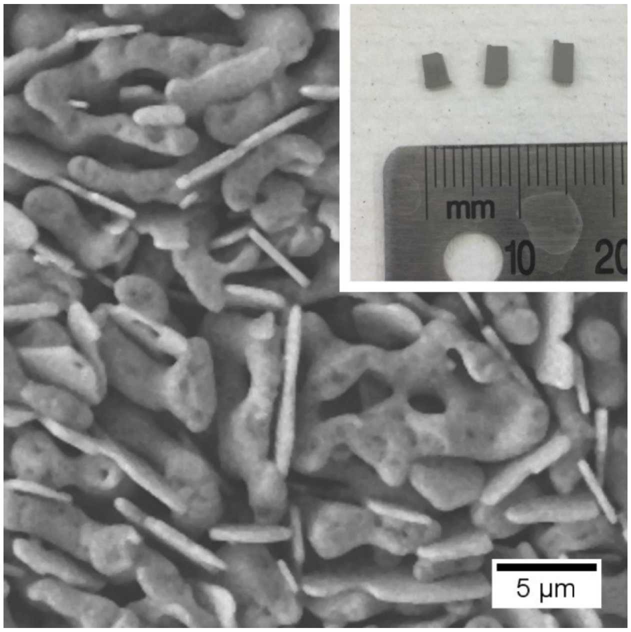

Figure 5-5: SEM micrograph of porous Nb resulting from LMD of $Nb_{40}Ti_{57}Si_3$ and etching in aqueous solution to remove Cu phase, showing precipitated Nb_5Si_3 plates. Optical micrograph of full porous samples (inset).

dealloying, suggesting that sections may be forming more of a lamellar eutectic structure than a bicontinuous one.

To determine whether the overall connectedness of the Nb network changes, the Cu phase can be removed to examine the structure directly. We selectively dissolved the Cu phase from our composite using a Cu redox etchant consisting of concentrated $CuCl_2$ and HCl as described above. The composition of the starting alloy did play an important role in the result of this etching process. Samples without silicon, $Nb_{30}Ti_{70}$ and $Nb_{40}Ti_{60}$, become detached at grain boundaries and fall apart like previous porous LMD materials. $Nb_{40}Ti_{67}Si_3$ showed good mechanical integrity after dissolution of Cu. The samples retained their shape and dimensions and were sufficiently strong to be handled in the laboratory without special care. **Figure 5-5** shows a micrograph of the surface of such a sample, with visible plates of Nb_5Si_3 visible protruding slightly from the geometric surface of sample. Samples disks up to a centimeter in diameter and a millimeter thick were processed in this way. The photograph inset in **Figure 5-5** shows several samples cut from the same plate of LMD material. $Nb_{30}Ti_{67}Si_3$ was found to fall apart into fine dust after LMD and dissolution of the copper phase, showing that the Nb ligament structure is no longer fully connected. This demonstrates that the necessary Nb necessary to form a continuous phase during LMD increases due to silicide formation.

Thermodynamics of silicide formation during LMD: The thermodynamics driving liquid metal dealloying of binary alloys have been described in detail by Geslin et al. [20]. The driving force for LMD is provided by the solubility difference in the liquid of the two primary solid components. In our system, Ti is the dissolving component with almost 80% solubility in molten Cu around the dealloying temperature (~1100 ºC), while Nb has nearly zero solubility. The basic binary alloy system is complicated slightly here by the addition of a third component to the starting alloy. In principle, the third component could either partition into the solid or the liquid phase during dealloying. In fact, the deep eutectic between Si and Cu combined with the small starting concentration of Si suggests that all the Si should dissolve readily along with Ti. This is contrary to our observation that, during LMD, Si instead reacts with Nb to form the high melting-point silicide intermetallic Nb_5Si_3, and that we see no evidence of Si in the liquid Cu-Ti solution.

Here we discuss the thermodynamics of the formation of the Nb_5Si_3 phase in order to identify other systems for which an analogous reaction will occur and use our observations to place a lower bound on the high temperature heat capacity of Ti_5Si_3, which to our knowledge, has never been measured. The basic thermodynamic

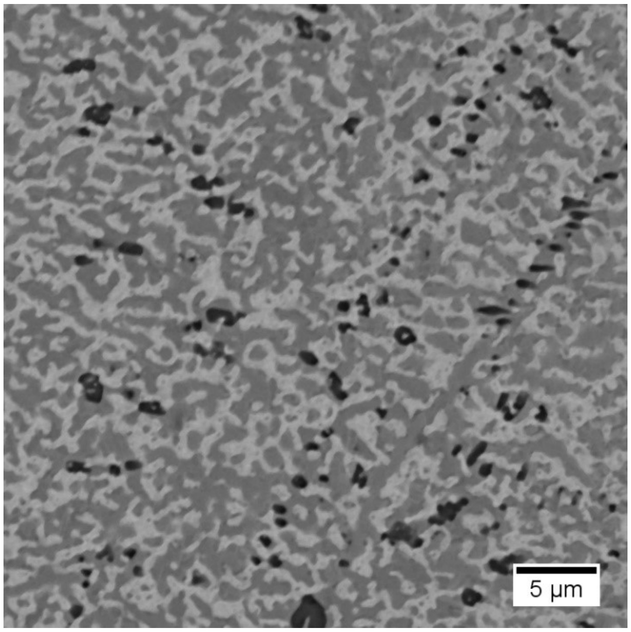

Figure 5-6: SEM micrograph of dealloyed $Mo_{30}Ti_{67}Si_3$ showing the formation of titanium silicide Ti_5Si_3 precipitates (darkest phase) formed during LMD; these are randomly distributed in the Cu phase of the composite.

competition is between the driving force for the formation of niobium silicide compared to the driving force for the formation of titanium silicide in the copper solvent under the experimental conditions. It will be useful to compare our Nb-alloy results with the results of dealloying Mo-Ti-Si alloys. We found that Mo-Ti alloys can be dealloyed in Cu with solid Mo ligaments forming, but upon adding a few percent of Si to the base alloy in this case, round Ti_5Si_3 precipitates appear in the liquid phase, as shown in the SEM image in **Figure 5-6**. This result requires that the Ti_5Si_3 has a stronger thermodynamic driving force to form than Mo_5Si_3, but less than Nb_5Si_3.

We quantitatively estimate the driving force for formation of each silicide as the Gibbs free energy of solidification from the melt at the experimental conditions. Both observed silicides form deep within the pores during dealloying, where there is significant Ti in the Cu liquid, along with smaller amounts of dissolving Si and some of the solid-phase metal that is also dissolved. Assuming the liquid phase is approximately ideal, and that the solid phase entropy is negligible, we calculate the entropy change ΔS during solidification for any of these silicides by selecting a representative composition for the liquid displaced by silicide formation. Because the liquid has the same composition regardless of which silicide forms, the entropy difference is the same for each silicide:

$$\Delta S = R\left(X_{Cu}\ln X_{Cu} + X_{Ti}\ln X_{Ti} + X_{Si}\ln X_{Si} + X_{Nb}\ln X_{Nb}\right), \qquad (1)$$

where X_M is the atomic fraction of the *M* silicide species, and R is the gas constant. The liquid composition is set so that $X_{Ti} = X_{Cu} = 0.48$ and $X_{Si} = X_{Nb} = 0.02$, for which we find $\Delta S = 7.16$ J/mol K. The enthalpy of solidification is calculated at the melting point, where solidification is reversible, and we again assume that the liquid is approximately ideal:

$$\Delta H\left(T_m\right) = T_m R\left(X_{Si}\ln X_{Si} + X_{Nb}\ln X_{Nb}\right), \qquad (2)$$

where T_m is the melting point of the intermetallic in question, and X_M is the atomic fraction of species M in the solidifying intermetallic. Using Eq. (2) the solidification enthalpies of the three silicides were calculated and are listed with their melting points in **Table 1**.

To estimate the enthalpy change at the dealloying temperature, the difference in heat capacity between the solid and liquid phase is integrated with respect to temperature from the melting point to the temperature of interest, in this case the LMD temperature T_d of 1100°C, according to the expression

$$\Delta H(T_d) = \Delta H(T_m) + \int_{T_m}^{T_d} \left(C_{p,solid} - C_{p,liquid} \right) dT \approx \Delta H\left(T_m\right) - \bar{C}_{p,solid}\left(T_m - T_d\right) + \bar{C}_{p,liquid}\left(T_m - T_d\right) \tag{3}$$

The average constant pressure heat capacity is denoted $\bar{C}_{p,liquid}$ for the melt of the component elements of the intermetallic and $\bar{C}_{p,solid}$ for the solid intermetallic silicide. Here, the liquid phase heat capacities can be found by averaging their constituent elements because the solutions are treated as ideal; they all sit near 270 J/mol K. Thus the heat capacities of the liquid phases are known (see **Table 5-1**) [21]; however, the heat capacities of the solid silicides at elevated temperature are not. This provides an opportunity to use our experimental observations to determine ranges for the average heat capacity of each intermetallic between the dealloying temperature and its respective melting point, as follows: Ti_5Si_3 and Nb_5Si_3 must both have negative Gibbs free energy of solidification, because they are both observed to form spontaneously, and the formation energy of the niobium silicide must be more negative for it to be preferred. Because it is not observed to form, the Gibbs free energy of solidification for Mo_5Si_3 must be greater than that of Ti_5Si_3, and there is no requirement that it be negative. To satisfy the first condition, the average heat capacity of the Ti_5Si_3 must be greater than 291 J/(mol K) to allow it to form. No direct measurement in this temperature range was found in literature, but the value here compares favorably with data gathered at lower temperatures [22]. At high temperatures, the heat capacity of solids is approximated by the Einstein heat capacity of $3nR$, or 200 J/(mol K) for the intermetallics here. The calculated value shows good agreement with the basic theory, because it is increased slightly by electronic additions to the purely lattice-based Einstein heat capacity model.

Niobium and molybdenum silicides are structurally identical and Nb and Mo are very similar with respect to their thermal properties, so we expect little difference in the heat capacity of these two intermetallics. If we assume that Nb_5Si_3 and Mo_5Si_3 have the same average heat capacity, we can calculate a range for this single value that makes the Nb silicide thermodynamically more favorable than Ti silicide while leaving the Mo silicide less stable, given the Ti_5Si_3 heat capacity listed above. This range of values for $\bar{C}_{p,solid}$ for both Nb_5Si_3 and Mo_5Si_3 is between 218 J/(mol K) and 242 J/(mol K), slightly higher than the 200 J/(mol K) lattice heat capacity estimate. They are 20% lower than the heat capacity of titanium silicide, but a similar difference is observed for the pure metals, so this discrepancy is expected [21]. This heat capacity range implies that no fundamental difference is necessary between the thermodynamics controlling the formation of Nb_5Si_3 vs. Mo_5Si_3; the higher solidification enthalpy brought about by its higher melting point is sufficient difference in driving force to explain the observed behavior. Following this reasoning, we predict observation of silicide precipitation during LMD in the Ta_5Si_3 (T_m = 2550 °C) system, but not the Cr_5Si_3 (T_m = 1666 °C) or V_5Si_3 (T_m= 1987 °C) systems, when dealloying in molten copper, because the relevant heat capacities of these materials are relatively similar at high temperatures, and their melting points are sufficiently above the LMD temperature.

Dealloying Kinetics in the presence of Si: In conventional dealloying in aqueous media, the overall dealloying rate is interface reaction limited, so the velocity of the

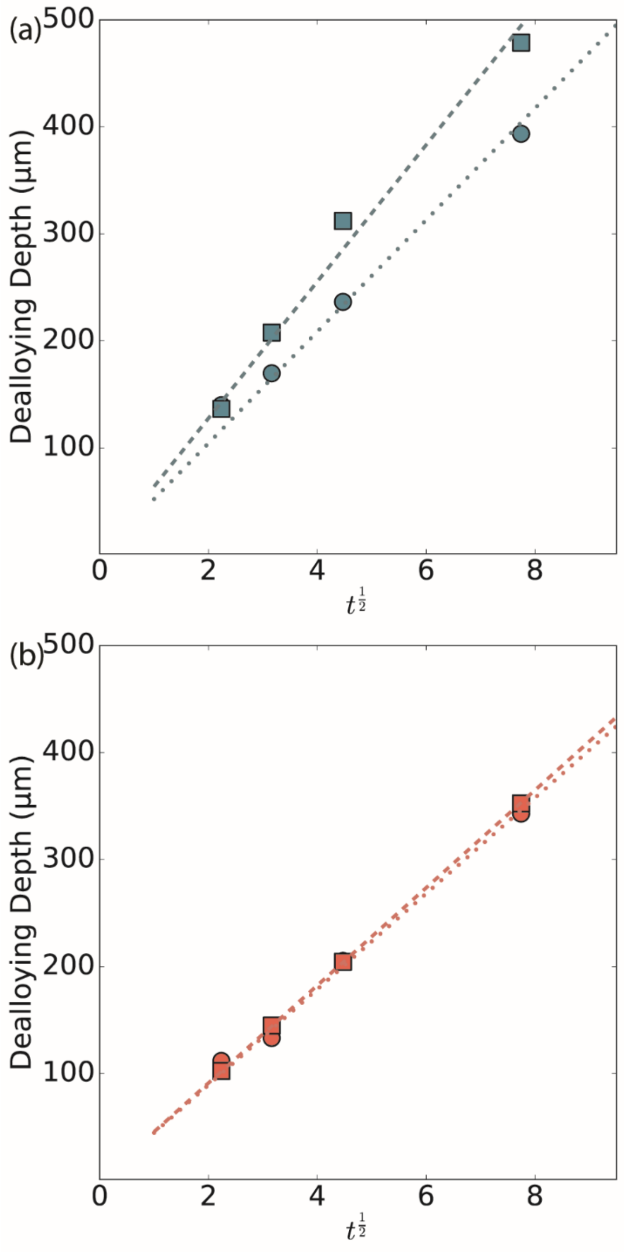

Figure 5-7: Dealloying depth as a function of time for various compositions of parent alloy: (a) $Nb_{30}Ti_{70}$ (green, circles) and $Nb_{30}Ti_{67}Si_3$ (green, squares); (b) $Nb_{40}Ti_{60}$ (orange, circles) and $Nb_{40}Ti_{57}Si_3$ (orange, squares).

dealloying front is constant and the depth *h* of the dealloyed layer increases linearly with time. In LMD however, it has been shown that this is not the case. Due to the much higher dissolution rate relative to liquid phase diffusion, the dealloying reaction rapidly becomes diffusion limited and the dealloying velocity dh/dt gradually slows down. Consistent with the diffusion limitation, the depth increases as $h \sim t^{1/2}$ in the case of porous Ta formed by LMD [5]. **Figure 5-7** shows the dealloying depth as a function of time for the same four parent alloys discussed previously: two with 30% Nb and two with 40%, each with and without 3% Si. In all cases, we see that same diffusion limited behavior and the expected $h \sim t^{1/2}$ dependence.

In the 40% Nb samples we see no change in the dealloying rate with the addition of Si. However, for the 30% Nb composition, the dealloying progresses significantly faster with Si present, contrary to our expectation. The different effects of silicide formation on the dealloying rate can be related to the difference in final structure of the material discussed above. Because the process is diffusion limited, and the driving force for diffusion is approximately the same with similar Nb content, the rate should be influenced by the effective path length for diffusion from the dealloying interface out of the porous structure. The formation of silicides parallel to this diffusion direction and the associated disconnection of the Nb phase means the diffusion path is more direct than in a randomly arranged porous network. This disconnection of the structure was not observed in the case with 40% Nb, and the dealloying rate remained similar as a result.

While there are significant kinetic differences in dealloying rate between the alloys, they all dealloy at a rate sufficient to rapidly form macroscopic LMD composites. The slowest dealloying starting alloy, $Nb_{40}Ti_{60}$ takes ~500 seconds to fully dealloy a 1 mm thick sample (dealloying from one side), while the fastest, $Nb_{30}Ti_{67}Si_3$, takes ~250 seconds. A sample with a centimeter dealloying depth would take 100 times as long due

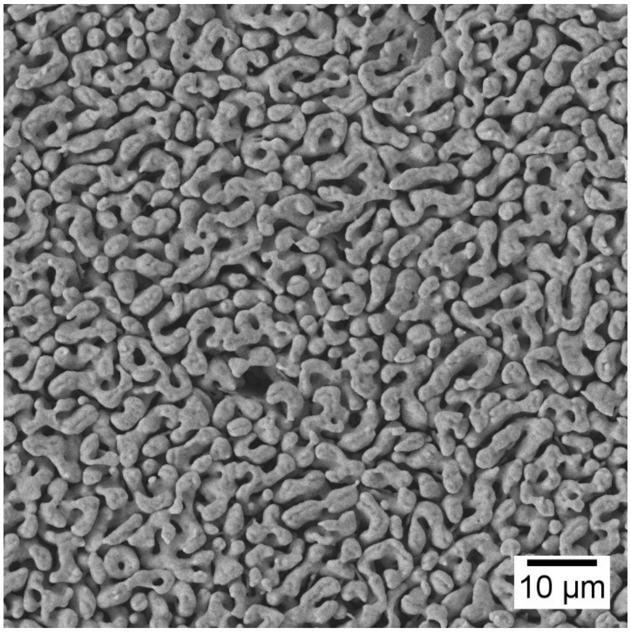

Figure 5-8: SEM image of the surface of silicide-containing porous Nb after heat treatment at 1850°C where the Si has evaporated leaving only metallic Nb with uniform rounded features, but without significant coarsening of the feature size.

to the diffusion-limited nature of the reaction, but the resulting 7 or 14 hours is still an attainable processing time for a bulk sample.

Composites: Dense composites of Cu and Nb are interesting in their own right, especially as a model system for mechanical testing analogous to Nb-Cu multilayer materials [23,24]. However, for many other applications it is of interest to work with a freestanding structure of porous Nb or to re-fill the volume occupied by solidified Cu with a different material [25,26]. Because we can make a freestanding mechanically robust porous ingot by dissolving the liquid phase from the Si-containing dealloyed sample, additional post-processing steps become available to engineer a final composite. As well, the robust freestanding porous Nb introduced here is, to our knowledge, the most thermally stable dealloyed material ever prepared owing to the high melting point of Nb, the lack of other residual elements with lower melting point, and the relatively large starting feature size. This was tested by heat-treating samples of porous Nb-Nb_5Si_3 in an Ar atmosphere. Samples showed no visible coarsening after heating for 8 hours at 1750 °C. Above 1800 °C, the porous structure and feature size remain similar, but elemental Si begins to evaporate from the niobium silicide, leaving behind the Nb which re-integrates into rounded ligaments, as shown in **Figure 5-8**. Only after heat treatment at temperatures above 1900 °C did we observe collapse of the porous structure, as the small amount of residual Ti in some ligaments caused local melting to occur.

The excellent thermal and chemical stability and micrometer-scale pore size allow these porous Nb samples to be filled with many materials simply by immersing them in a melt. Any metal that does not interact with Nb is an obvious candidate, because this allows the production of metal-metal composites which cannot be formed directly from LMD due to the phase behavior of the constituents. Another class of materials of interest are glasses. Borosilicate glass in particular has a softening point around 800 °C, but the viscosity is too high for it to flow into small pores until much higher temperatures. At 1400 °C, immersing a piece of porous Nb in a melt of borosilicate glass for 2 hours yielded a fully dense Nb-Nb_5Si_3-borosilicate ternary composite shown in **Figure 5-9**, with the porous structure fully infiltrated with glass throughout the sample.

5.4 Conclusions

Materials fabricated by LMD are still in the early stages of development. In order to realize the full potential of these materials, challenges associated with coarsening and grain detachment must be addressed to engineer functional fully porous metals with a uniformly defined length scale. By reinforcing the mechanical stability of porous structures with refractory silicides, fully porous bulk samples of Nb were fabricated with

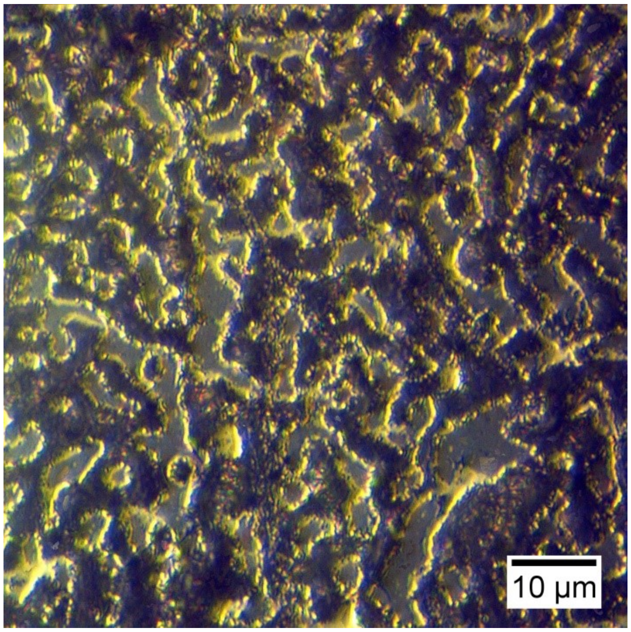

Figure 5-9: Optical micrograph of a polished cross section of Nb/Nb_5Si_3/borosilicate ternary composite formed by immersing porous Nb in molten glass (b).

sufficient mechanical integrity to be handled for processing after full dissolution of the Cu phase. The three-phase silicide-containing composites studied here were fabricated in a single step from a homogeneous alloy precursor, and the additional silicide phase did not inhibit the formation of porosity during dealloying.

In general, silicide-containing porous Nb is a prototype for a new kind of dealloyed material, with multiple phases with properties that can be tuned quasi-independently, in principle allowing the design of robust, multifunctional porous materials. The formation of multiple phases in a single processing step is a powerful tool for composite fabrication. The combination of physical robustness and thermal stability in this porous Nb in particular makes it an interesting intermediate for the fabrication of further composites by filling the pores with an additional material of interest, especially when high-temperature processing is required.

	Nb_5Si_3	Ti_5Si_3	Mo_5Si_3
T_m (°C)	2799	2400	2453
$\Delta H\left(T_m\right)$ (kJ/mol)	-123	-106	-108
$\bar{C}_{p,L}$ (J/mol K)	268	278	271
$\bar{C}_{p,S}$ (J/mol K)	218	291	218

Table 5-1: Reference and estimated thermodynamic quantities for silicides of Nb, Ti, and Mo. Melting temperature T_m and liquid phase heat capacity $\bar{C}_{p,L}$ from reference [21]. The enthalpy of solidification at the melting point ($\Delta H\left(T_m\right)$) is calculated assuming ideal mixing in the liquid phase, with compositions of dissolved species as discussed in the text, and the average solid phase heat capacity ($\bar{C}_{p,S}$) is the calculated minimum via Eqs. (2) and (3).

5.5 References

[1] J. Erlebacher, M.J. Aziz, a Karma, N. Dimitrov, K. Sieradzki, Evolution of nanoporosity in dealloying., Nature. 410 (2001) 450–453. doi:10.1038/35068529.

[2] J. Weissmüller, K. Sieradzki, Dealloyed nanoporous materials with interface-controlled behavior, MRS Bull. 43 (2018) 14–19. doi:10.1557/mrs.2017.299.

[3] I. McCue, E. Benn, B. Gaskey, J. Erlebacher, Dealloying and Dealloyed Materials, Annu. Rev. Mater. Res. 46 (2016) 263–286. doi:10.1146/annurev-matsci-070115-031739.

[4] T. Wada, K. Yubuta, A. Inoue, H. Kato, Dealloying by metallic melt, Mater. Lett. 65 (2011) 1076–1078. doi:10.1016/j.matlet.2011.01.054.

[5] I. McCue, B. Gaskey, P.A. Geslin, A. Karma, J. Erlebacher, Kinetics and morphological evolution of liquid metal dealloying, Acta Mater. 115 (2016) 10–23. doi:10.1016/j.actamat.2016.05.032.

[6] I. McCue, A. Karma, J. Erlebacher, Pattern formation during electrochemical and liquid metal dealloying, MRS Bull. 43 (2018) 27–34. doi:10.1557/mrs.2017.301.

[7] Q. Chen, K. Sieradzki, Spontaneous evolution of bicontinuous nanostructures in dealloyed Li-based systems, Nat. Mater. 12 (2013) 1102–1106. doi:10.1038/nmat3741.

[8] L.H. Qian, M.W. Chen, Ultrafine nanoporous gold by low-temperature dealloying and kinetics of nanopore formation, Appl. Phys. Lett. 91 (2007) 89–92. doi:10.1063/1.2773757.

[9] Y.C.K. Chen-Wiegart, S. Wang, Y.S. Chu, W. Liu, I. McNulty, P.W. Voorhees, D.C. Dunand, Structural evolution of nanoporous gold during thermal coarsening,

Acta Mater. 60 (2012) 4972–4981. doi:10.1016/j.actamat.2012.05.012.

[10] L.Y. Chen, J.S. Yu, T. Fujita, M.W. Chen, Nanoporous copper with tunable nanoporosity for SERS applications, Adv. Funct. Mater. 19 (2009) 1221–1226. doi:10.1002/adfm.200801239.

[11] D. V. Pugh, A. Dursun, S.G. Corcoran, Formation of nanoporous platinum by selective dissolution of Cu from Cu0.75Pt0.25, J. Mater. Res. 18 (2003) 216–221. doi:10.1557/JMR.2003.0030.

[12] M. Tsuda, T. Wada, H. Kato, Kinetics of formation and coarsening of nanoporous α-titanium dealloyed with Mg melt, J. Appl. Phys. 114 (2013). doi:10.1063/1.4821066.

[13] J. Erlebacher, An Atomistic Description of Dealloying, J. Electrochem. Soc. 151 (2004) C614. doi:10.1149/1.1784820.

[14] A. Pareek, S. Borodin, A. Bashir, G.N. Ankah, P. Keil, G.A. Eckstein, M. Rohwerder, M. Stratmann, Y. Gr??nder, F.U. Renner, Initiation and inhibition of dealloying of single crystalline Cu 3Au (111) surfaces, J. Am. Chem. Soc. 133 (2011) 18264–18271. doi:10.1021/ja2054644.

[15] F. Scaglione, F. Celegato, P. Rizzi, L. Battezzati, A comparison of de-alloying crystalline and amorphous multicomponent Au alloys, Intermetallics. 66 (2015) 82–87. doi:10.1016/j.intermet.2015.06.022.

[16] F. Scaglione, P. Rizzi, L. Battezzati, De-alloying kinetics of an Au-based amorphous alloys, J. Alloys Compd. 536 (2012) S60–S64. doi:10.1016/j.jallcom.2011.11.087.

[17] J.W. Kim, M. Tsuda, T. Wada, K. Yubuta, S.G. Kim, H. Kato, Optimizing

niobium dealloying with metallic melt to fabricate porous structure for electrolytic capacitors, Acta Mater. 84 (2015) 497–505. doi:10.1016/j.actamat.2014.11.002.

[18] J.W. Kim, T. Wada, S.G. Kim, H. Kato, Sub-micron porous niobium solid electrolytic capacitor prepared by dealloying in a metallic melt, Mater. Lett. 116 (2014) 223–226. doi:10.1016/j.matlet.2013.11.036.

[19] I. McCue, S. Ryan, K. Hemker, X. Xu, N. Li, M. Chen, J. Erlebacher, Size Effects in the Mechanical Properties of Bulk Bicontinuous Ta/Cu Nanocomposites Made by Liquid Metal Dealloying, Adv. Eng. Mater. 18 (2016) 46–50. doi:10.1002/adem.201500219.

[20] P.A. Geslin, I. McCue, B. Gaskey, J. Erlebacher, A. Karma, Topology-generating interfacial pattern formation during liquid metal dealloying, Nat. Commun. 6 (2015) 1–8. doi:10.1038/ncomms9887.

[21] E.S. Domalski, E.D. Hearing, Condensed Phase Heat Capacity Data, in: P.. Linstrom, W.G. Mallard (Eds.), NIST Chem. WebBook, NIST Stand. Ref. Database Number 69, National Institute of Standards and Technology, Gaithersburg, MD, n.d. doi:doi:10.18434/T4D303.

[22] S. Agarwal, E.J. Cotts, S. Zarembo, R. Kematick, C. Myers, Heat capacities of titanium silicides Ti5Si3, TiSi and TiSi2, J. Alloys Compd. 314 (2001) 99–102. doi:10.1016/S0925-8388(00)01223-8.

[23] A. Misra, J.P. Hirth, R.G. Hoagland, Length-scale-dependent deformation mechanisms in incoherent metallic multilayered composites, Acta Mater. 53 (2005) 4817–4824. doi:10.1016/j.actamat.2005.06.025.

[24] A. Misra, M.J. Demkowicz, X. Zhang, R.G. Hoagland, The radiation damage

tolerance of ultra-high strength nanolayered composites, JOM. 59 (2007) 62–65. doi:10.1007/s11837-007-0120-6.

[25] I. Nowak, M. Ziolek, Niobium Compounds: Preparation, Characterization, and Application in Heterogeneous Catalysis, Chem. Rev. 99 (1999) 3603–3624. doi:10.1021/cr9800208.

[26] P. Kathirgamanathan, S. Ravichandran, Conducting polymer cathodes for high-frequency operable electrolytic niobium capacitors, Synth. Met. 74 (1995) 165–170. doi:10.1016/0379-6779(95)03363-7.

6 High-hardness Dealloyed Coatings for Ni-based Alloys

We present a dealloying-based technique to form fully dense metal composite coatings on Ni-based alloy substrates, in which a Ti alloy precursor coating is first applied to the substrate by plasma spray and then during a subsequent heat treatment, eutectic melting at the interface between the coating and substrate drives a phase separation in both alloys. The microstructural evolution here is analogous to liquid metal dealloying, forming a topologically complex multiphase composite. These coatings have hardness as high as 15 GPa, but unlike many materials of similar hardness they display significant plastic deformation rather than immediate brittle failure. The flexibility and scalability of the dealloying process used here make this a promising avenue for large-scale implementation of a dealloyed materials for mechanically robust coatings.

6.1 Introduction

Nickel alloys are technologically important for applications which require high-temperature strength and creep resistance, especially for power generation and aerospace where energy efficiency is directly related to the thermal stability of systems [1]. The development of new Ni-based superalloys is still an area of active research. Coatings for these alloys are also vital in a variety of applications, including thermal barrier coatings to moderate the temperature experienced by the alloy part in extreme environment applications [2]. Intermetallic compounds including NiTi and $NiTi_2$ have a unique combination of properties including thermal stability and corrosion resistance [3] that make them uniquely suited as coatings in applications where the thermal and electrical insulation from a ceramic-based coating is unnecessary or undesirable. These compounds can be applied directly to component surfaces with techniques such as thermal spray [4]. However, while thermal spray intermetallic coatings can have excellent mechanical properties, they can have some limitations. These limitations include porosity, which allows corrosive environments permeate through the coating to attack the substrate [5,6] and delamination due to poor adhesion [7]. Here, we present a strategy to mitigate these shortcomings by post-treatment of a thermal-sprayed coating in which a dealloying reaction takes place between the coating and substrate. This reaction forms a composite microstructure in the coating, hardening it, repairing porosity left over from the thermal spray process, and improving adhesion with the substrate.

Dealloying is – most commonly – a process used to form porosity in alloys by selectively dissolving one component in a liquid medium [8]. Often, this liquid medium is an aqueous electrolyte, and dissolution is driven either by a chemical etchant or by an externally applied electrochemical potential [9]. Recently, attention has turned towards liquid metal dealloying (LMD), where this aqueous medium is replaced by a liquid metal bath, and the dissolution is driven by a difference in solubility between components in the starting alloy. LMD experiments are often performed by immersing a piece of initial material to dealloy in a molten bath of the chosen liquid metal [10,11]. Both electrochemical dealloying and LMD can produce bicontinuous porous structures where the volume vacated by the dissolving element leaves a network of interconnected pores, and the other alloy constitutents rearrange to form a network of mutually interconnected ligaments [12]. The mechanical performance of these porous structures, prototyped by nanoporous gold (np-Au), has been heavily studied by simulations and experimentally [8,13,14], but porous networks themselves are not useful as a protective coating. Dense composites have been prepared by impregnating np-Au with polymers [15,16], but liquid metal dealloying can be used to prepare fully dense metal-metal composites directly, where the void space in the porous network is filled with solidified liquid phase. Previously, this has been accomplished in several metal systems by immersing an alloy directly in a molten metal bath at a controlled temperature, but this process is difficult to accomplish at a large scale [17,18]. However, McCue et al showed that the mechanical properties of Ta-Cu composites in particular are promising, especially in compression [19]. This material is convenient to make due to the phase behavior of Cu and Ta, but neither metal has widespread structural applications, the former due to its poor strength, and the latter due to price, scarcity, and processing difficulty. A similar composite structure containing more mechanically efficient metals would be significantly more promising as a genuine path to a commercializable dealloyed structural composite.

Another inherent drawback of LMD as a commercial technique is the processing itself. In the laboratory, it is practical to immerse a sample in a bath of molten metal much larger than the sample itself, but this process is difficult to scale up. Also, since dealloying occurs from the surface and slows down as the dealloyed depth increases, the total volume of material that can be dealloyed with a given feature size is fundamentally limited, as the volume of dealloyed material behind the dissolution front coarsen rapidly. However, while this limits applications for bulk materials, the formation of two-dimensional materials including coatings is less hindered by such coarsening, because dealloying times can remain short.

Here, a variation of LMD is employed to form a coating on the surface of an existing part, where the dealloying reaction occurs at the interface between two alloys.

Rather than immersing the coated part in a liquid bath, the liquid metal to drive dealloying is provided by a eutectic melt that forms at the interface between two solid alloys of different compositions. A commercial nickel alloy (Haynes 230) was coated with a titanium-chromium binary alloy using plasma spray deposition. During subsequent heat treatment above the eutectic temperature of the Ni-Ti system, interdiffusion leads to melting at the interface between substrate and coating, driving a phase separation and composite formation in both directions and resulting in a dealloying reaction that forms a fully dense microstructured intermetallic coating with much higher hardness than either starting alloy including hardness, measured by nanoindentation, above 15 GPa, while maintaining the ability to plastically deform during micro-scale indentation experiments.

6.2 Experimental Methods

All powders in this study were provided by Oerlikon Metco. Initial coating samples were prepared by plasma spraying Ti-alloy powder on Ni-alloy substrates using plasma spray equipment at the Johns Hopkins Applied Physics Laboratory. Ti-alloy powder had composition of $Ti_{55}Cr_{45}$. Some particles showed up to 5at% Al contamination caused by reaction with the aluminum oxide crucible used to contain the melt during the gas atomization process that produced the powder. The powder was separated by particle size, with the fraction between 90 and 45 micrometers used for plasma spray. Substrates for plasma spray were Haynes 230, a nickel alloy with 57% Ni, 22% Cr and 14% W by weight, with several percent of Mo, Fe, and Co and smaller amounts of other alloying elements. Coupons 25 mm by 76 mm were cut use a water jet cutter from a 3.18 mm thick sheet of Haynes 230 purchased from California Metal & Supply (Santa Fe Springs, CA) and the surface was treated with alumina abrasive to improve coating adhesion. A coating of Ti-Cr alloy powder approximately 100 micrometers thick was applied in a single plasma spray coat. Heat treatment was conducted on these samples in a quartz tube evacuated to high vacuum (~10^{-6} torr) and heated in a tube furnace.

Plasma sprayed coupons were cross sectioned by electrical discharge machining and the surface mechanically polished to observe the structure both before and after heat treatment. The top surface of the coating was polished to remove oxide scale and x-ray diffractometry (XRD) was performed to identify phases present. Bulk hardness was measured with Vickers indentation, and local mechanical properties were tested on a Nanomechanics iNano nanoindenter. Differential Thermal Analysis (DTA) was performed on an TA Instruments SDT Q600. Transmission electron microscope (TEM) samples were prepared by lifting out a section of coating from approximately one third of the way from the substrate to the surface using focused ion beam (FIB) systems at Drexel University (FEI Strata DB235) and Texas A&M University (Tescan FERA-3 Model GMH), and observed using a FEI Tecnai 12 TEM equipped with EDS and electron diffraction detectors at Johns Hopkins University and a FEI Tecnai G2 F20 TEM with electron diffraction at Texas A&M.

6.3 Results and Discussion

Plasma sprayed coatings are formed by distinct partially melted particles packing randomly on a surface. This melting is sufficient to bond the particles, but porosity caused by voids between particles is a problem. Here, plasma spray was conducted in air, so there is significant oxidation of individual particles during the process, although the argon carrier gas provides some protection for the particles while molten in flight. **Figure 6-1** shows the cross section of the coating before heat treatment, with significant voids

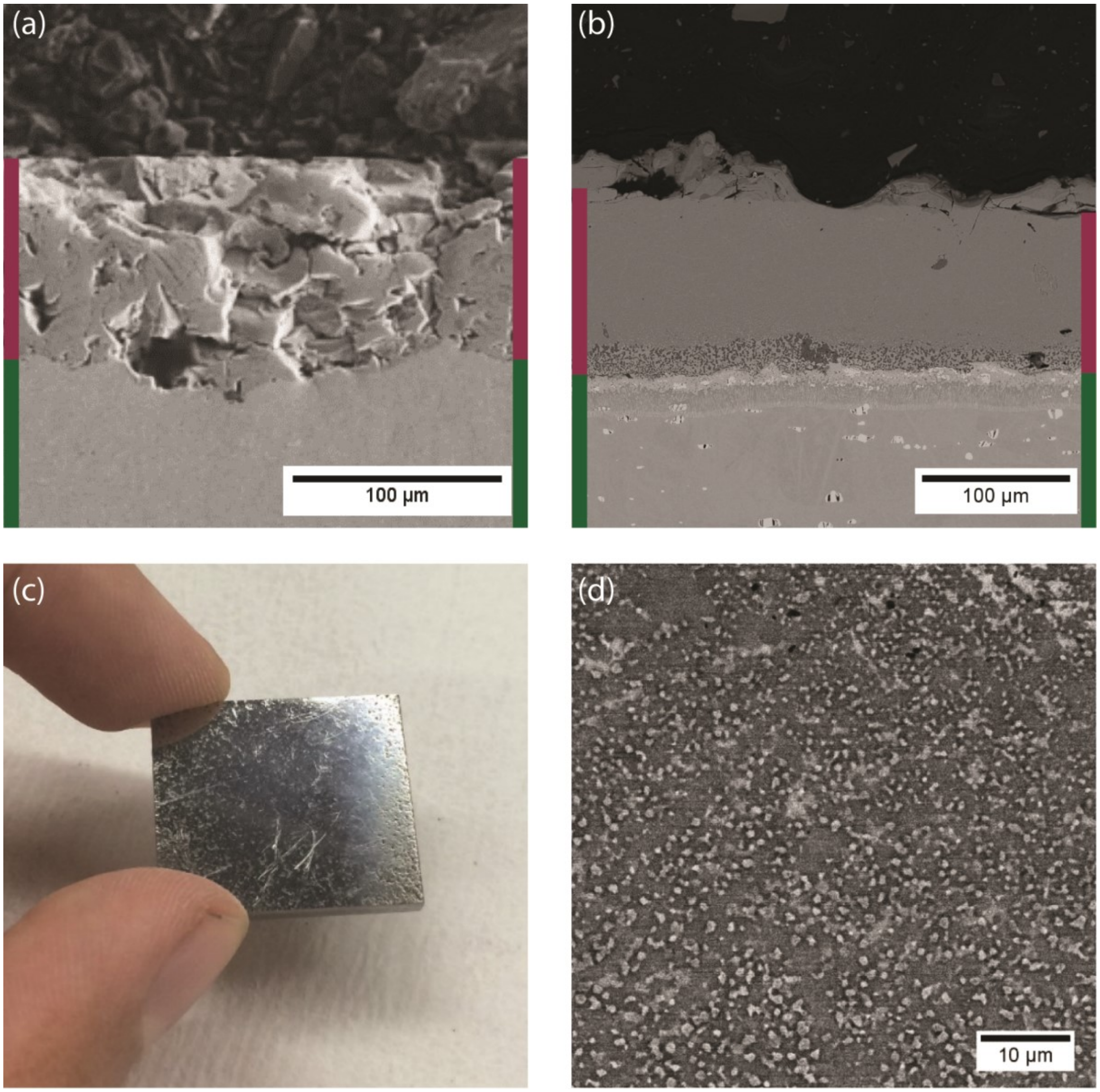

Figure 6-1: (a) A plasma sprayed coating of Ti$_{55}$Cr$_{45}$ on nickel-based alloy substrate was cross sectioned to observe the microstructure of the coating by SEM. (b) After plasma spray, the coating was heat treated at 1150 °C for 270 seconds. In both (a) and (b), the coating is highlighted in red and the substrate in green. Major defects and voids visible in the coating are removed by heat treatment. (c) Optical image of a large area of polished coating, used for XRD analysis. (d) Higher resolution detail of an area in the middle of the coating cross section in (d) showing the fine microstructural features present.

visible in the structure. To dealloy the structure, it was heated in a furnace set at 1200 °C. A thermocouple was placed in contact with the sample and a timer was started as the local temperature passed 1150 °C. After 270 seconds during which the sample continued heating to approximately 1180 °C, the evacuated quartz tube containing the sample was pulled out of the furnace and the sample cooled rapidly to below 700 °C.

After heat treatment, the microstructure of the coating has changed entirely. Large voids are no longer present and the interface between the coating and substrate has smoothened. Both the coating and substrate show a multiphase structure where before there was only a single solid solution alloy phase. Three phases are primarily present in the coating; backscattered electron imaging in a scanning electron microscopy (SEM) makes this clear owing to compositional contrast based on atomic number. The brightest Cr-rich phase has randomly distributed rounded features that range in size between 500 nm and 1 μm. Samples as large as several cm^2 were heat treated, and in all cases the samples showed uniform phase evolution throughout. A sample lifted out of the coating using a focused ion beam (FIB) and imaged by transmission electron microscopy (TEM) provides more detail on the phase distribution (representative micrographs are shown in **Figure 6-2)**. Three phases are present with submicron-sized domains, a darker Ni-rich phase, intermediate contrast Cr-rich phase, and lightest Ti-rich domains. Energy dispersive x-ray spectroscopy (EDS) shows that the Cr domains are mostly pure (>95% Cr), and peaks matching the body-centered cubic Cr lattice are readily identifiable using X-ray diffractometry (XRD) over a large area of the coating. The other two phases contain a mixture of the three elements, with the more Ni rich phase composed of approximately $Ni_{56}Ti_{39}Cr_4$ and the Ti rich phase composition close to $Ni_{34}Ti_{56}Cr_{10}$. The latter phase has Ni:Ti ratio close to 1:2, suggesting that it may be similar to the $NiTi_2$ intermetallic compound stable in the binary alloy system, but the more Ni rich phase has no direct binary alloy analog. TEM characterization shows an array of lines through

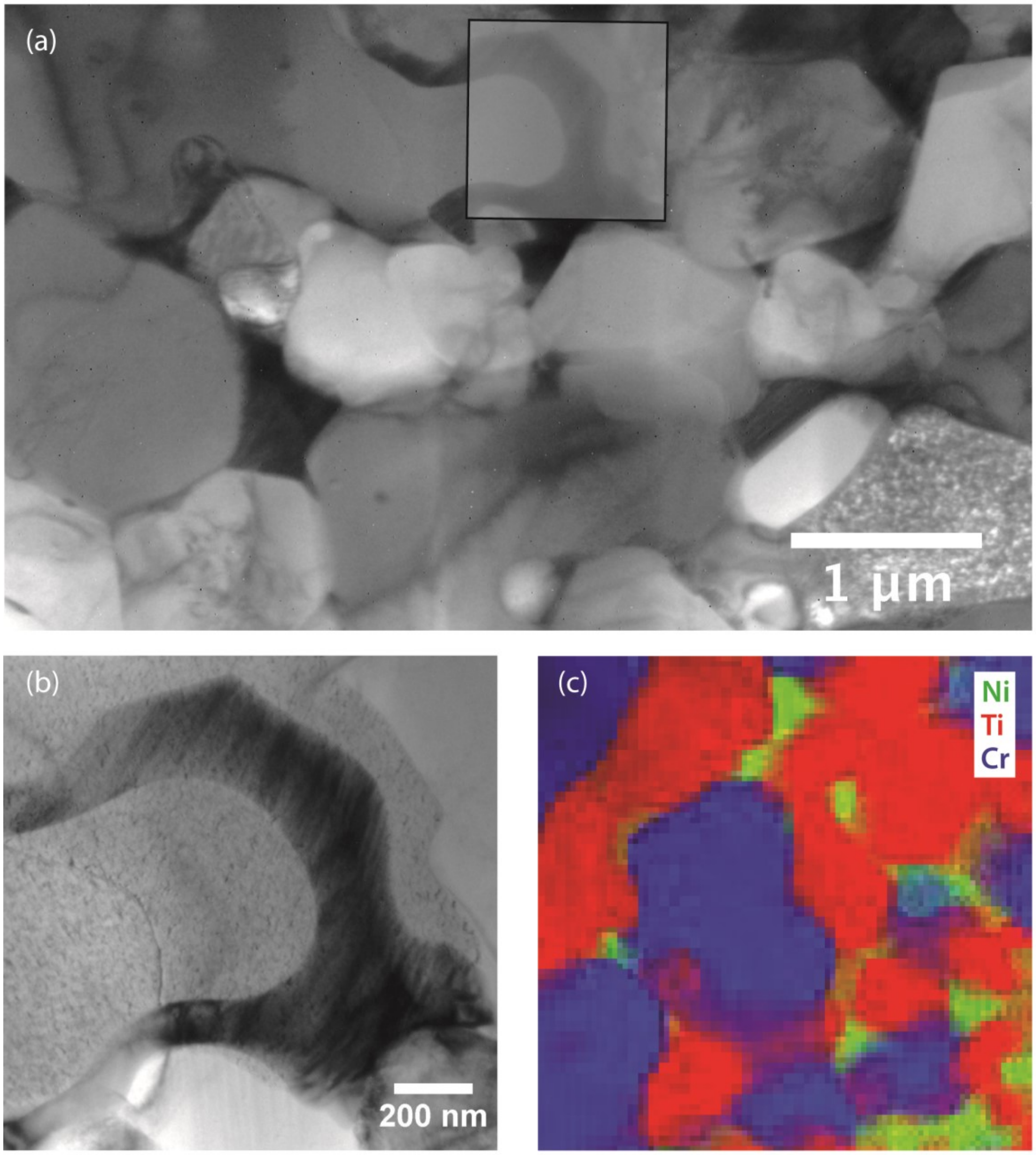

Figure 6-2: (a) TEM micrograph of a section of heat-treated coating sample lifted out and polished by focused ion beam milling, with Ni-rich dark phase, Ti-rich bright phase, and intermediate contrast Cr-rich phase. (b) High resolution of highlighted area in (a) showing contrast within a Ni domain possibly caused by an array of twins. (c) EDS mapping showing sharp interfaces between the three major phases present.

grains of this Ni-rich phase which could indicate deformation twins induced by thermal stresses during solidification. Some of the other domains also show a relatively high defect density which could contribute to the mechanical properties of the coating by effectively work hardening some phases while the coating forms.

Microstructural Evolution: To understand the mechanism that results in this phase behavior requires a step-by-step analysis of the liquid metal dealloying process that takes place. The thermodynamics that drive liquid metal dealloying of a binary alloy in a single-element bath are well understood. The microstructural evolution that results in the final coating structure here is somewhat more complex, with multiple components present in both the film and substrate alloys that interact in a specific way. The $Ti_{55}Cr_{45}$ coating powder was nominally a single-phase binary alloy, and although the powder contained several trace impurities and several percent of residual Al from the gas atomization process, here we only consider the action of Ti and Cr. The substrate was more complex, with 22% Cr and 14% W (by weight) the main alloying elements in a Ni matrix. Mo, Fe, and Co were also present in quantities that were observable by EDS, but they were also omitted in the analysis of the phase evolution during dealloying. Thus, a simplified system for considering the LMD is a NiCrW ternary alloy in contact with a TiCr binary alloy. The only liquid that can be formed by this system at the temperatures used for heat treatment is a Ti-Ni binary eutectic liquid, due to the much higher melting points of Cr and especially W. The liquid can form above either of two eutectic points on the binary phase diagram, the lower temperature one around 73 at. % Ti and 950 °C or the higher temperature one at 33 at. % Ti and 1120 °C. In order for a liquid to form, sufficient solid-state interdiffusion must occur at the interface between substrate and coating for the liquid composition to be reached. Studies of the interdiffusion coefficients for Ti and Ni are known in the binary system [20], and the diffusion of Ti into a Ni matrix is faster than the reverse. The presence of alloying elements Cr and W likely slows all interdiffusion. Thus, we expect that the eutectic closer to pure Ni is more kinetically accessible to the system, and thus is the liquid that drives the LMD process. At the reaction temperature, the two eutectic liquids have a solid region separating them, so the two liquids cannot coexist in the same region of the sample without a solid barrier forming between them. Small amounts of pure Ni and TiCr powder were mixed and analyzed by differential thermal analysis (DTA) to observe thermodynamic changes in the material during the dealloying process. The main feature observed was an exotherm associated with the eutectic melting in the temperature range between 1100 °C and 1150 °C. This agrees with the diffusivity trends and suggests that this Ni-rich eutectic is important in allowing the dealloying reaction to begin.

Once the eutectic liquid forms upon heating, liquid phase diffusion makes the phase evolution proceed more rapidly. Due to the low temperature, Cr and W have limited solubility in the eutectic liquid and preferentially partition into solid domains instead of dissolving. In order for the liquid phase to grow, additional Ti from the coating combines with Ni from the substrate in order to maintain a liquid composition, and as Ni and Ti diffuse through the liquid, the liquid phase grows in both directions normal to the coating/substrate interface. The microstructure formed by dealloying depends on the fraction of each alloy that remains solid, so a different microstructure appears on each side of this interface [12]. In the substrate, the relatively high initial Ni concentration causes a lamellar structure to form, with solid Cr- and W-rich domains growing alongside the liquid channels; this is consistent with the total fraction of Cr and W around 0.15. In the coating, the composition was selected to form a more geometrically complex

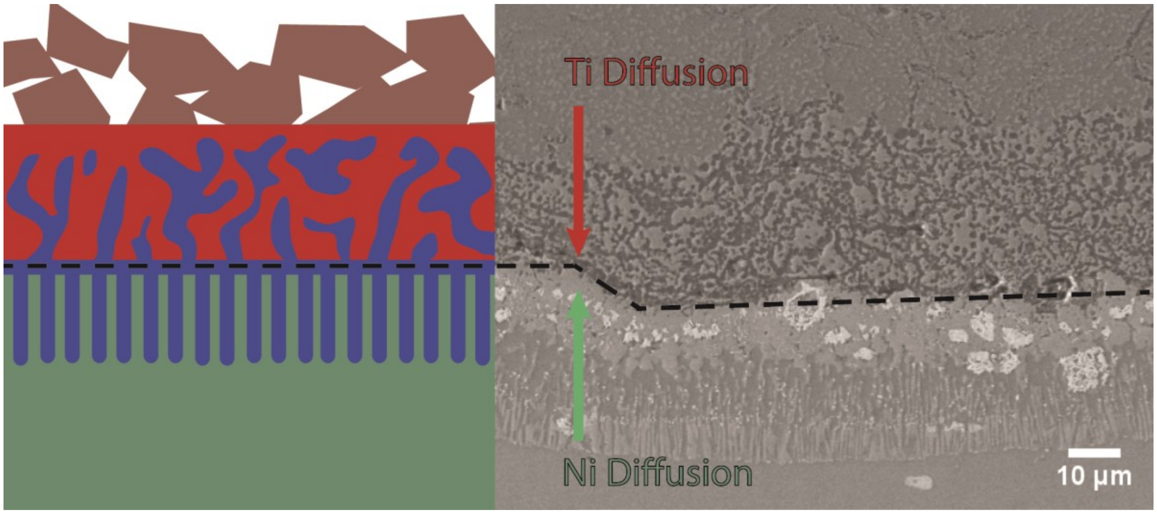

Figure 6-3: A schematic of the phase evolution occurring during dealloying, with Ni diffusing from the substrate and Ti diffusing from the coating to mix in a eutectic liquid that provides an expedited diffusion path, while Cr-rich phases remain solid in both the substrate and coating, and a SEM micrograph of the cross section of the interface, showing a matching microstructure with a random network of phase domains extending into the coating and a lamellar structure visible in the substrate.

structure, and the result is a network of interconnecting Cr-rich solid domains and liquid channels. This process is shown schematically in **Figure 6-3** alongside a detail of the resulting microstructure near the interface. As areas of the coating liquify from the interface towards the surface, surface tension drives densification and removes particle boundaries left from the plasma spray process. The result is the homogeneous distribution of small Cr-rich domains, as shown in **Figure 6-1**. After heat treatment, the sample cools and the eutectic liquid solidifies rapidly in a confined volume within the pores. If a binary eutectic liquid of similar composition were allowed to cool slowly with no geometric constraints, it would form a mixture of intermetallic compounds of Ni and Ti, but this is not observed in this coating. The major domains associated with the solidifying liquid contain the Ti-rich and Ni-rich phases. Due to the small volume and relatively rapid cooling, the first phase that nucleates can rapidly consume the available liquid even when

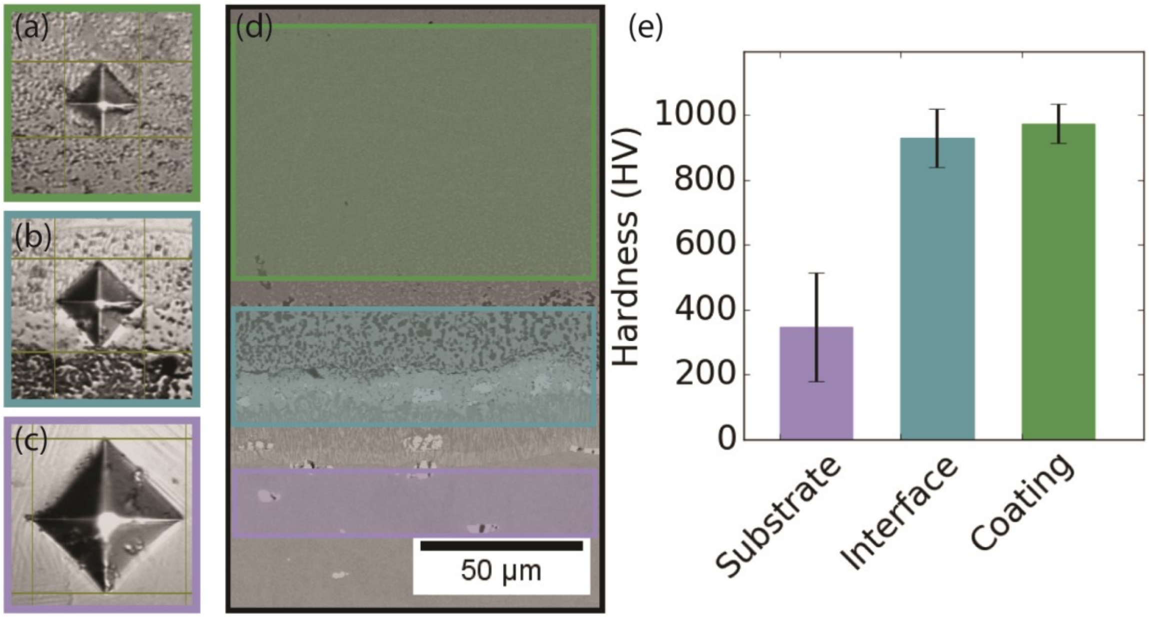

Figure 6-4: Optical images of Vickers indentations used to test local hardness in the coating (a), at the interface layer between the coating and substrate (b), and in the unreacted substrate (c). Low magnification SEM image showing the areas on the sample from which each set of indentations was made (d) and the average measured hardness in each area (e).

a more thermodynamically favorable equilibrium phase exists. We hypothesize that this is the reason the mixtures that we observe do not correlate directly with the equilibrium phase diagram for this system.

Mechanics: The unique dealloying mechanism used here is particularly promising due to the mechanical properties of the coating. It is known that fully dense LMD composites display multiple hardening mechanisms related both to their geometric structure and the reduced length scale of the individual phases [19]. For this material, bulk hardness was initially measured through Vickers indentation on the polished cross section of the coating. Our results are summarized in **Figure 6-4**. The coating average of 974 HV is far higher than any of the individual components. Importantly, indentations up to 500 grams force had no cracking at the corners. Indenting at the interface between coating and substrate measured a similarly high hardness value and showed no indication of cracking or delamination along the interface. In this system, the interface is fundamentally very strong because the eutectic liquid bridges the interface and so there is no interruption in the Ni- and Ti- rich phases at the edge of the original substrate, i.e., the coating is connected to the substrate via a continuous phase, not a bond between two dissimilar materials. Failure of this interface requires breaking phase domains, or delamination of many interconnected domains along a geometrically complex surface.

The mechanics of the coating were investigated in more detail using nanoindentation, which can probe properties with greater spatial resolution and, using dynamic stiffness measurements, measures both hardness and modulus continuously as a function of the depth of indentation. The smaller indentations also mean that properties can be measured at a lengthscale similar to the feature size in the sample, so the variation in mechanical properties associated with the individual phases present become visible [21]. A hardness map histogram generated by nanoindentation is shown in **Figure 6-5**, summarizing the evolution of the stiffness and hardness as the indentation depth increases. The spread of the elastic moduli are approximately follow a normal distribution at small indentation depths, with the modulus decreasing slightly as the distribution sharpens with increasing indentation depth. The hardness shows more interesting behavior. At shallow depths, some indentations have greatly increased in hardness, leading to a bimodal distribution in hardness. At great indent depths, the hardness of both groups of indents converge on a bulk hardness value around 15 GPa. Some individual indents have initial hardness as high as 25 GPa, before a significant strain burst and continuing plastic deformation at a lower hardness, consistent with the average bulk hardness value measured.

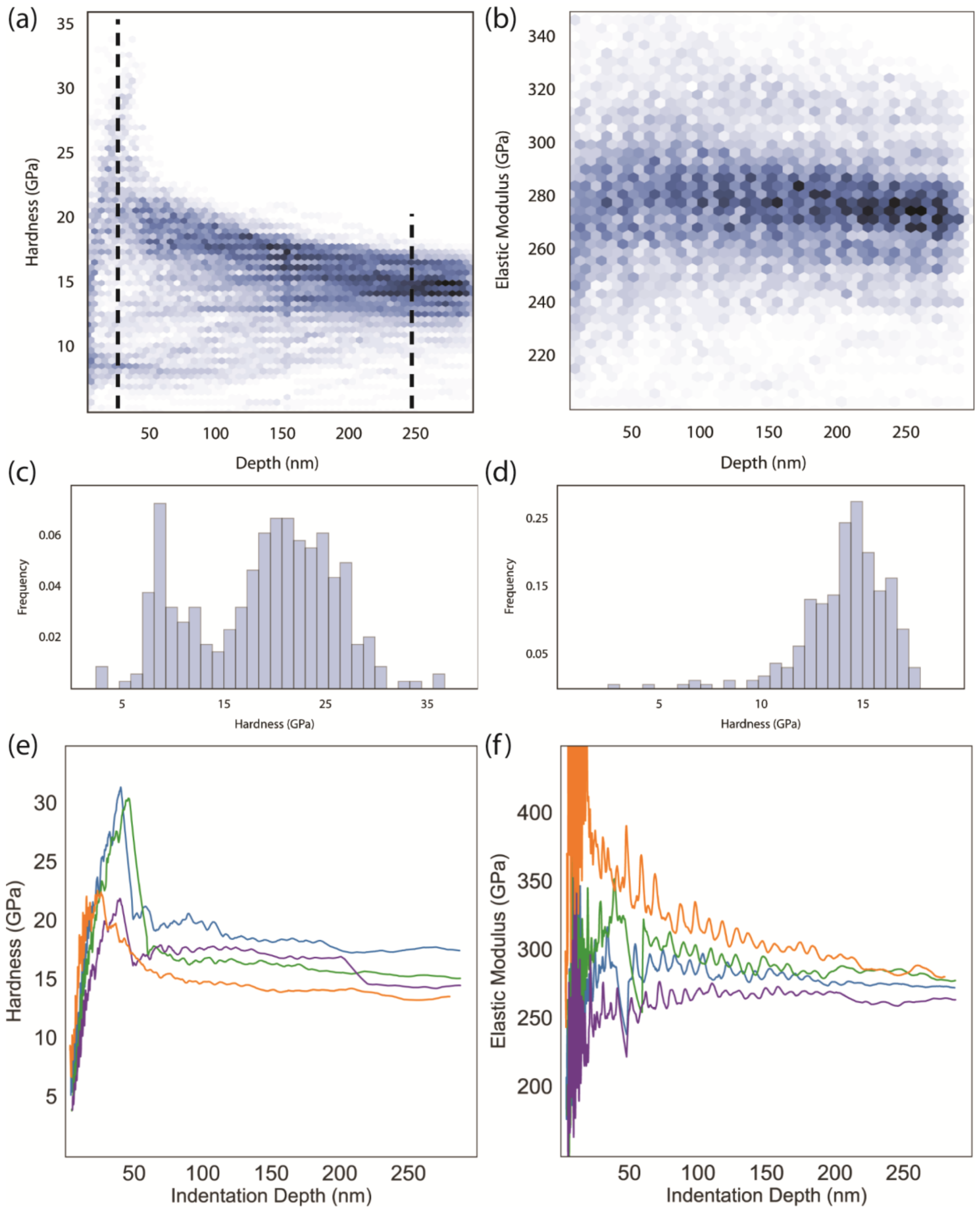

Figure 6-5: Nanoindentation data taken from 400 indentations in a square area in the middle of the cross section of the coating. (a) Hardness as a function of indentation depth, with dashed lines indicating cross sections of the density plot shown by the histograms in (c) (30 nm indentation depth) and (d) (250 nm indentation depth). (b) Elastic modulus as a function of indentation depth. (e-f) Individual hardness and modulus curves for four indentations.

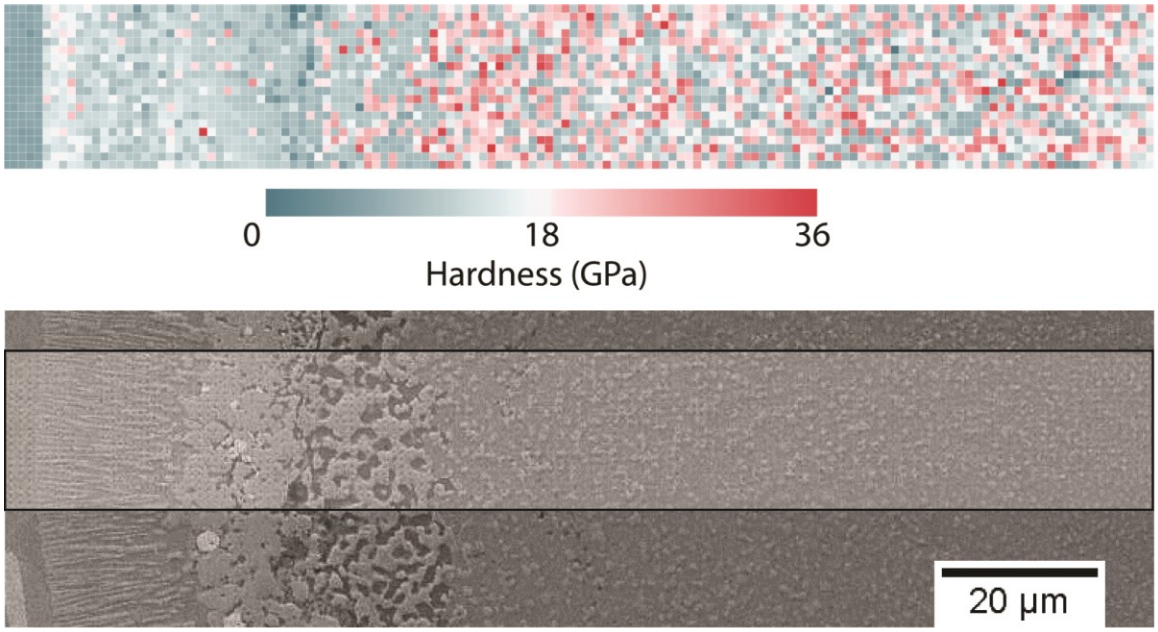

Figure 6-6: Hardness map (top) formed by an array of minimally spaced indents across the cross section of a heat-treated coating from the substrate on the left to the edge of the coating on the right, with visible interfaces at the lowest extent of dealloying and the initial interface between substrate and coating.

Nanoindentation also allows the spatial visualization of the areas exhibiting strain bursts, so we can correlate these with the microstructure. By plotting the measured hardness at 50 nm indentation depth for each indentation on the cross section, **Figure 6-6** shows that they are distributed uniformly around the coating, slightly more prevalent near the interface with the substrate, so these points should uniformly increase the bulk hardness throughout the coating. The lowest-strength area of the cross section occurs near the interface where large Ti-rich domains are visible, but both this area and the dealloyed region at the surface of the original substrate are stronger than the unreacted substrate. As discussed previously, this contributes to a coating that is extremely resistant to failure by delamination.

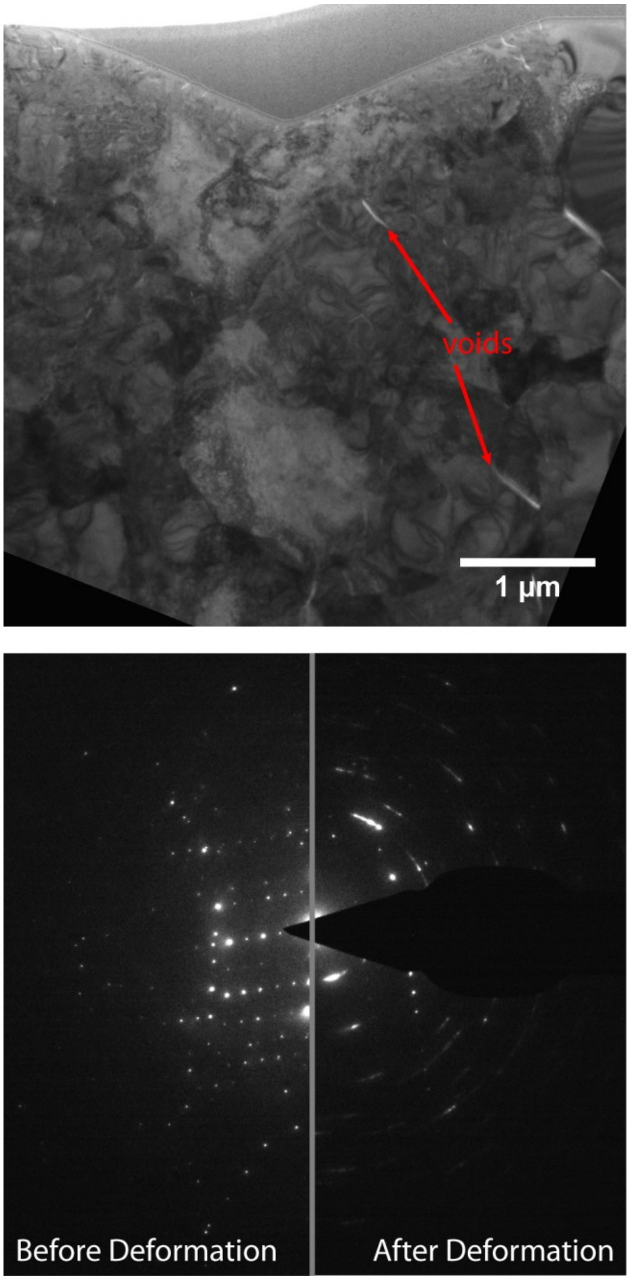

Figure 6-7: TEM characterization of a coating sample prepared by indenting a cross section of the coating with a Knoop-type indenter tip and lifting out a section under the indentation using FIB milling. The triangular indentation is visible at the top of the image (top). Some voids appear between phase domains below the indentation. TEM electron diffraction shows that sharp individual diffraction peaks before deformation become smeared multiple spots afterwards due to the disruption to the structure of grains from defects introduced during deformation (bottom).

To observe the deformation of the microstructure directly, a sample was indented and a slice from the plastic deformation zone below the indentation was removed for observation by FIB milling. TEM characterization of the sample is shown in **Figure 6-7**. Some voids at phase domain interfaces are visible within the sample, but they can only account for a small fraction of the plastic deformation from the visible indentation. Electron beam diffraction of a pristine area of composite compared to an area within the plastically deformed region shows that diffraction spots associated with individual grains have spread out due to plastic deformation of the grains, demonstrating that macroscopic plastic deformation is not dominated by phase boundary sliding or microscopic interfacial cracking.

6.4 Conclusion

Coatings are vital to extend the lifetime of many metal parts by providing thermal shielding, preventing abrasion, or isolating the part from environmental corrosion. Here, we design and fabricate a metal-intermetallic composite coating for Ni-alloy parts that exhibit extreme hardness. Utilizing a novel dealloying reaction driven by eutectic melting at the interface between coating and substrate, the geometrically complex coating microstructure can form during a simple heat treatment. The material system studied here combines the intrinsic mechanical properties of metal and intermetallic phases with the geometric and size-dependent strengthening from the LMD structure to form a coating with remarkable hardness. It also provides a blueprint for a new materials design strategy employing dealloying, where the phase evolution occurs at the interface between metals rather than at a bulk solid-liquid interface, which promises rapid processing and increased scalability compared to existing dealloying techniques.

6.5 References

[1] T.M. Pollock, S. Tin, Nickel-Based Superalloys for Advanced Turbine Engines: Chemistry, Microstructure and Properties, J. Propuls. Power. 22 (2006) 361–374. doi:10.2514/1.18239.

[2] D.R. Clarke, M. Oechsner, N.P. Padture, Thermal-barrier coatings for more efficient gas-turbine engines, MRS Bull. 37 (2012) 891–898. doi:10.1557/mrs.2012.232.

[3] N.S. Stoloff, C.T. Liu, S.C. Deevi, Emerging applications of intermetallics, Intermetallics. 8 (2000) 1313–1320. doi:10.1016/S0966-9795(00)00077-7.

[4] L. Pawlowski, The science and engineering of thermal spray coatings, John Wiley & Sons, 2008.

[5] N. Cinca, C.R.C. Lima, J.M. Guilemany, An overview of intermetallics research and application: Status of thermal spray coatings, J. Mater. Res. Technol. 2 (2013) 75–86. doi:10.1016/j.jmrt.2013.03.013.

[6] J.A. Hearley, J.A. Little, A.J. Sturgeon, The effect of spray parameters on the properties of high velocity oxy-fuel NiAl intermetallic coatings, Surf. Coatings Technol. 123 (2000) 210–218. doi:10.1016/S0257-8972(99)00511-3.

[7] Y. Wang, W. Chen, Microstructures, properties and high-temperature carburization resistances of HVOF thermal sprayed NiAl intermetallic-based alloy coatings, Surf. Coatings Technol. 183 (2004) 18–28. doi:10.1016/j.surfcoat.2003.08.080.

[8] I. McCue, E. Benn, B. Gaskey, J. Erlebacher, Dealloying and Dealloyed Materials, Annu. Rev. Mater. Res. 46 (2016) 263–286. doi:10.1146/annurev-matsci-070115-031739.

[9] J. Erlebacher, M.J. Aziz, a Karma, N. Dimitrov, K. Sieradzki, Evolution of nanoporosity in dealloying., Nature. 410 (2001) 450–453. doi:10.1038/35068529.

[10] T. Wada, K. Yubuta, A. Inoue, H. Kato, Dealloying by metallic melt, Mater. Lett. 65 (2011) 1076–1078. doi:10.1016/j.matlet.2011.01.054.

[11] I. McCue, B. Gaskey, P.A. Geslin, A. Karma, J. Erlebacher, Kinetics and morphological evolution of liquid metal dealloying, Acta Mater. 115 (2016) 10–23. doi:10.1016/j.actamat.2016.05.032.

[12] P.A. Geslin, I. McCue, B. Gaskey, J. Erlebacher, A. Karma, Topology-generating interfacial pattern formation during liquid metal dealloying, Nat. Commun. 6 (2015) 1–8. doi:10.1038/ncomms9887.

[13] H.-J. Jin, J. Weissmüller, D. Farkas, Mechanical response of nanoporous metals: A story of size, surface stress, and severed struts, MRS Bull. 43 (2018) 35–42. doi:10.1557/mrs.2017.302.

[14] L.Z. Liu, X.L. Ye, H.J. Jin, Interpreting anomalous low-strength and low-stiffness of nanoporous gold: Quantification of network connectivity, Acta Mater. 118 (2016) 77–87. doi:10.1016/j.actamat.2016.07.033.

[15] K. Wang, J. Weissmüller, Composites of nanoporous gold and polymer, Adv. Mater. 25 (2013) 1280–1284. doi:10.1002/adma.201203740.

[16] K. Wang, A. Kobler, C. Kübel, H. Jelitto, G. Schneider, J. Weissmüller, Nanoporous-gold-based composites: Toward tensile ductility, NPG Asia Mater. 7 (2015) 1–11. doi:10.1038/am.2015.58.

[17] J.W. Kim, M. Tsuda, T. Wada, K. Yubuta, S.G. Kim, H. Kato, Optimizing niobium dealloying with metallic melt to fabricate porous structure for electrolytic capacitors, Acta Mater. 84 (2015) 497–505. doi:10.1016/j.actamat.2014.11.002.

[18] T. Wada, H. Kato, Three-dimensional open-cell macroporous iron, chromium and ferritic stainless steel, Scr. Mater. 68 (2013) 723–726. doi:10.1016/j.scriptamat.2013.01.011.

[19] I. McCue, S. Ryan, K. Hemker, X. Xu, N. Li, M. Chen, J. Erlebacher, Size Effects in the Mechanical Properties of Bulk Bicontinuous Ta/Cu Nanocomposites Made by Liquid Metal Dealloying, Adv. Eng. Mater. 18 (2016) 46–50. doi:10.1002/adem.201500219.

[20] G.F. Bastin, G.D. Rieck, Diffusion in the titanium-nickel system: II. Calculations of chemical and intrinsic diffusion coefficients, Metall. Trans. 5 (1974) 1827–1831.

[21] I. McCue, B. Gaskey, B. Crawford, J. Erlebacher, Local heterogeneity in the mechanical properties of bicontinuous composites made by liquid metal dealloying, Appl. Phys. Lett. 109 (2016). doi:10.1063/1.4971776.

7 The Future of Liquid Metal Dealloying

7.1 Introduction

The detailed study of dealloyed materials is a relatively new field. Electrochemical dealloying was long considered a corrosion phenomenon to avoid, and it was comparatively recently that the insights garnered from corrosion science was put to use in the development of new materials. Liquid metal dealloying (LMD) is likewise in the early phases of development. While the concept of porosity formation due to selective dissolution upon immersion in a metal melt was first noted more than 50 years ago, it was initially treated as a corrosion process to be avoided during the material selection phase of engineering. LMD reappeared in the literature in 2011, but the delay associated with the adoption of the technique means that only a handful of groups around the world are actively pursuing fabricating LMD materials, and many of the publications since then have focused on recipes to make new materials. This has left a gap both in understanding underlying phenomena important to the LMD process and in detailed characterization of LMD materials for specific applications.

The main aim of this thesis has been to address the fundamental microstructural evolution of materials made by LMD, by studying the impact of kinetic and diffusive processes that control the structure and composition of the resulting materials. However, it is equally important to look forward and consider how the unique features of LMD materials can provide properties necessary to improve a particular product or process. In **Chapter 6**, we have suggested one straightforward way, applying the intrinsic strength of the microstructure to form a coating with excellent hardness that maintained the ability to deform plastically under load, but as a broader range of metals becomes available for LMD, many more applications will become available. Here, we briefly discuss several emerging LMD materials, as well as possible applications for materials discussed previously.

7.2 Dealloyed Silicon

First, we examine the formation of porous silicon during dealloying of Si-Ge binary alloys. Because Si is a semiconductor rather than a metal, the porous networks formed have electronic applications, including use in battery anodes, that are unique among dealloyed materials. A method of making LMD silicon was first reported by Wada et. al in 2015 [1], where the precursor was the silicide intermetallic Mg_2Si. This material shows promise as a high-capacity anode for lithium ion batteries because the complex geometry of the dealloyed structure allows the Si phase to expand in volume as it reacts with lithium while remaining electrically connected to the current collector [2], in analog to nanowire arrays used in a similar application, but with potentially higher charge capacity and more scalable processing [3].

Besides the obvious interest in applying metallurgical processing like dealloying to a semiconductor like Si, there are also unique crystallographic features possessed by this system compared to other dealloying systems. Si crystals have diamond cubic symmetry not shared by any metal. As discussed previously, the crystallographic features of a samples are often maintained through the dealloying process, but that has never previously been observed in a diamond cubic crystal. In LMD of Mg_2Si, a phase change is forced since the intermetallic precursor has a different structure, but a solid solution alloy of Si and Ge can be dealloyed similarly by LMD in a melt of Bi or Sn.

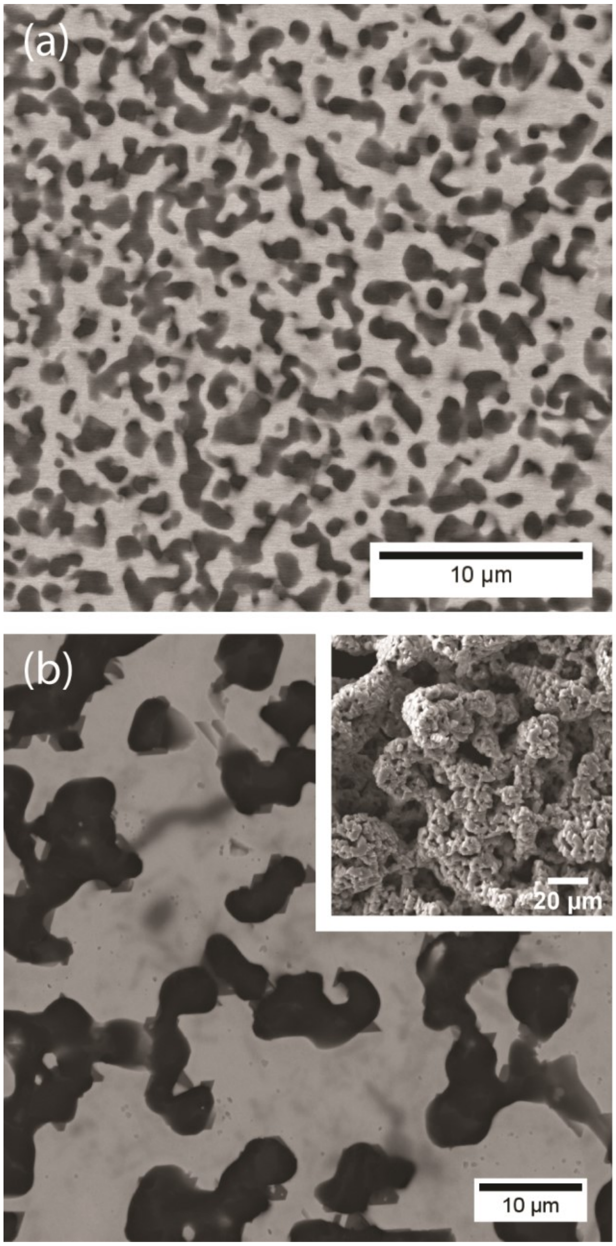

Figure 7-1: SEM micrographs of porous Si prepared by immersion in Sn for 10s (a) and Bi for 90s (b) both at 800 °C. Removing the Bi phase by dissolution in nitric acid leaves the porous Si structure shown in the inset.

Experimental Methods: The precursor alloy for silicon dealloying experiments was $Si_{25}Ge_{75}$, which was alloyed by induction melting in a graphite crucible which acted to both contain the sample as well as heat it by coupling to the induction field in the low temperature regime where Si and Ge are insufficiently electrically conductive to heat.

After melting, the sample was annealed for 8 hours to allow grains to grow and homogenize, although the low interdiffusion coefficients of Si and Ge meant that some compositional variation was present in the final sample. Slices cut with a diamond wafering saw were suspended from a wire and dipped in baths of molten Bi or Sn at various times and temperatures like in other LMD experiments discussed previously (see experimental methods in **Chapter 2**).

Results and Discussion: Surprisingly, dealloying Si and Ge in melts of Bi or Sn produces very different results, shown in **Figure 7-1**. Dealloying in Sn forms a porous structure with rounded ligaments similar to dealloyed metals. However, dealloying in Bi produces a strongly faceted structure in which the ligaments have many flat faces and relatively sharp corners. This is even more clearly visible when the Bi phase is dissolved, revealing facets with hexagonal symmetry on the surface of the ligaments. This structure suggests that the interface between solid Si and molten Bi has highly anisotropic surface energy compared to the Si-Sn interface, which drives the removal of higher energy surfaces in favor of low-energy facets. Bi metal is known to form highly anisotropic crystals compared to Sn, but in this case it is the Bi melt that displays particularly high surface energy anisotropy.

The porous Si prepared previously by Wada and coworkers has angular faceted ligaments as well, but these ligaments features are random rather than organized on length scale larger than a ligament. This is expected due to the small crystal domains formed by the phase transition occurring during dealloying, but in this system it is not required. The coherence of the facet directions between adjacent ligaments is evidence that they remain part of a single larger crystal. Image analysis of the ligament shape,

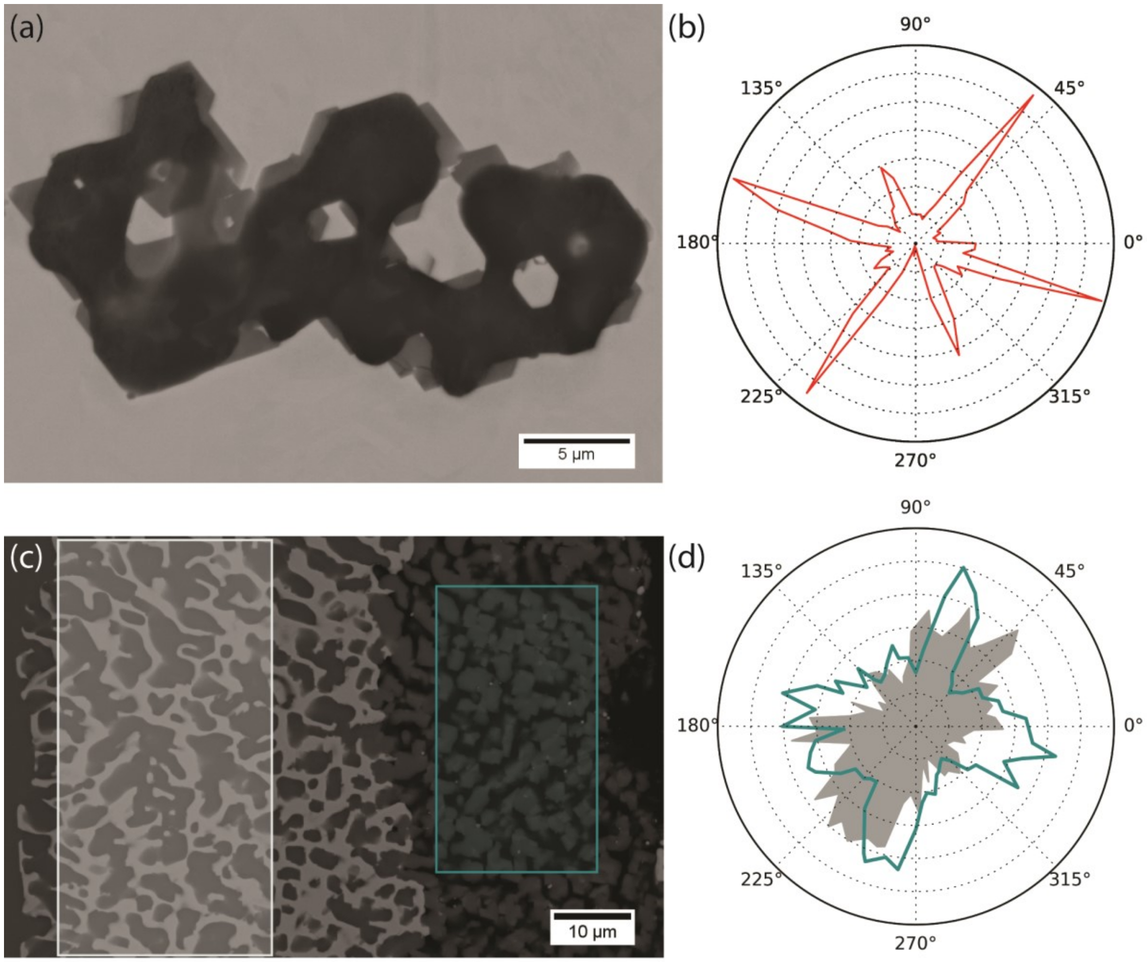

Figure 7-2: SEM micrographs of polished cross sections of porous Si (darker phase) dealloyed in molten Bi at 800 °C for 60 s (a) and 10 s (c) with angular distribution plots showing the distribution of edge direction for a single ligament dealloyed for 60 seconds with hexagonal symmetry (c), and for the ensemble of ligaments in the highlighted areas of part (c) with random distribution (gray) and rectangular symmetry (green) (d).

shown in **Figure 7-2**, shows this more clearly. A single ligament has facets with a clear crystallographic bias, and interestingly this bias is similar to the equilibrium shape of a silicon crystal as measured previously [4]. Forming large crystals with their equilibrium shape is a very slow process in general, with equilibrium facets limited to nanometer scale by the prohibitive activation barrier to nucleating new facets beyond this length scale [5]. In this system, near equilibrium facets formed on the micron scale within the 90 seconds of the dealloying process. Observing the initiation of dealloying in a shorter experiment provides some insight into the time scales involved. **Figure 7-2** shows a transition taking place between rounded and faceted ligaments (in this case with rectangular symmetry due to the rotation of the crystal). As dealloying progresses, the time for ligament surfaces to rearrange grows, so this transition could simply occur at some characteristic time after dealloying, but during LMD, there is also a gradient in Ge concentration in the melt which can change the surface characteristics. We hypothesize that dissolved Ge lowers the interfacial energy between solid Si and the melt, and as the Ge concentration decreases the driving force for faceting grows until some critical value where the shape transformation becomes favorable, at which point it proceeds rapidly.

While this behavior has yet to be studied in detail, it demonstrates a promising path forward for LMD, as a process to make porous semiconductor networks, as a technique for making large near-equilibrium-shape crystals for further study, and as a general tool for forming composites and porous materials with control over the shape and crystallography at the boundary between phase domains.

7.3 Applications of LMD Niobium

Previously, the kinetics and thermodynamics of LMD to form porous refractory metals by dealloying in Cu-based melts has been discussed in detail (see **Chapters 2 - 5**) but the applications for these materials have only been mentioned briefly. Here we look at two applications in greater depth: Nb-based high-performance capacitors, and anisotropic structural composites.

Tantalum and niobium are employed in high performance capacitors due to their stability and the good dielectric properties of their oxides [6,7]. Previous work by Kim

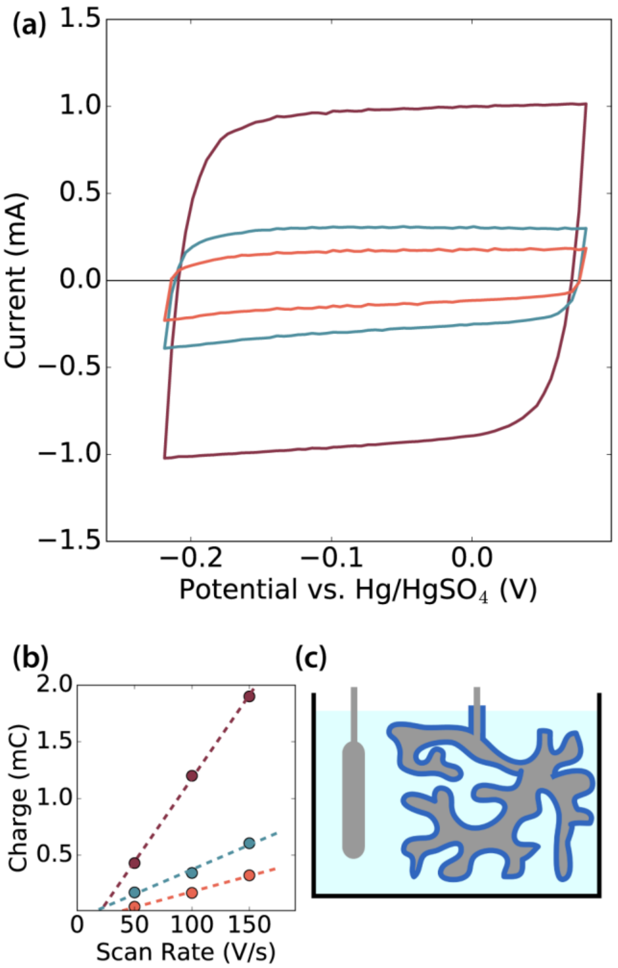

Figure 7-3: Cyclic voltammograms taken at 150 mV/sec scan rate of three samples of porous Nb/Nb_5Si_3 anodized at 2.5V (red) 5V (green) and 10V (orange) (a) with the corresponding chart of total charge storage vs. scan rate that can be used to calculate specific capacitance of 142 mF/g (2.5V, red), 50 mF/g (5V, green), 5mF/g (10V, orange). (c) A schematic of the electrochemical cell for these measurements, with anodized porous Nb immersed in electrolyte with a counter electrode.

and coworkers has shown that porous Nb prepared by LMD is a good candidate material for capacitors [8]. Utilizing the freestanding porous Nb/Nb_5Si_3 composites studied in **Chapter 5**, solid-state Nb capacitor devices can be made easily.

Experimental Methods: Composites of $Nb/Nb_5Si_3/Cu$ were prepared and characterized by the identical methods described in in **Chapter 5**. After dissolution of the solidified Cu leftover from LMD, the porous Nb sample, still suspended from the Ta wire used to hold it during dealloying, was immersed in electrolyte and anodized at several potentials to create Nb_2O_5 layers of varying thickness.

Results and Discussion: The capacitance of a porous sample can be tested directly by immersing the sample in electrolyte, or a solid-state device can be completed by filling the pore volume with a charge collector, commonly a conducting polymer or MnO_2. **Figure 7-3** shows preliminary data for Nb porous Nb anodized at a variety of potentials. Samples were immersed in electrolyte and their specific capacitance measured using electrochemical double-layer charging. Thinner oxide dielectrics resulting from lower-voltage anodization lead to improved capacitor performance, with specific capacitance as high as 142 mF/g Nb measured on a sample anodized at 2.5V.

Another application of LMD composites is as a structural component with high hardness without sacrificing ductility. As discussed previously, Nb/Cu laminated multilayer systems are used as a model to study the mechanical properties associated with nanoscale grains of Cu and Nb [9]. Dealloyed composites provide a contrasting geometry in the same material system with a tunable length scale. Ta/Cu composites also have promising mechanical properties [10,11]. However, by forming multiple phases during LMD, additional strengthening mechanisms are available compared to simple binary composites. The composites in **Chapter 5** contain plates of Nb_5Si_3, a refractory intermetallic with emerging applications as a high temperature structural material to replace or supplement nickel-based alloys [12]. **Figure 7-4** shows that the high hardness of this additional phase adds significant strengthening to the composite. Additionally, the plates are oriented in the direction of the dealloying reaction, and they impart this anisotropy to the mechanical properties as well, with the highest hardness measured when

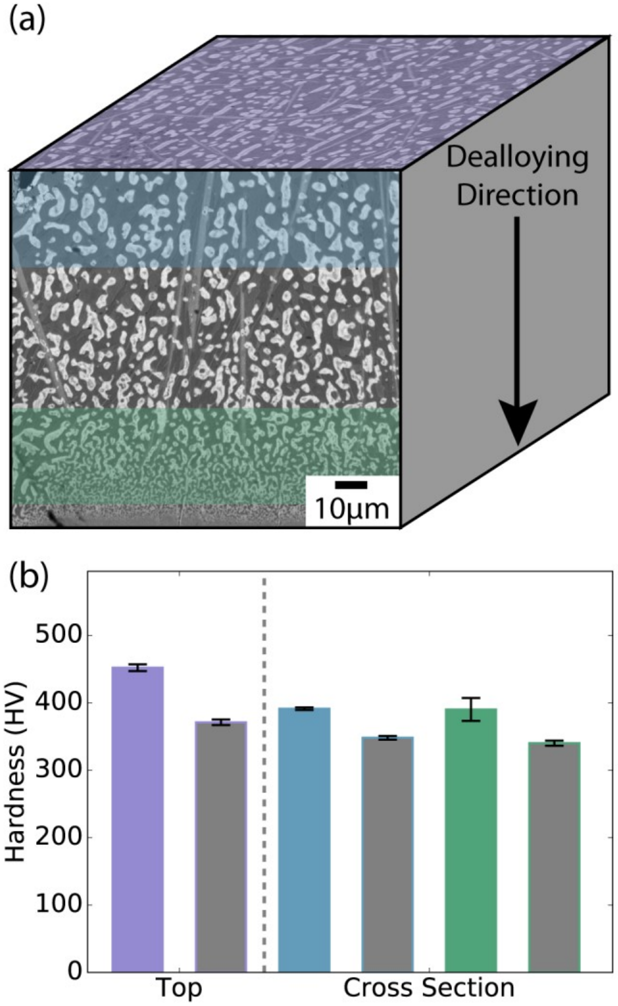

Figure 7-4: Vickers microhardness for $Nb/Nb_5Si_3/Cu$ composite tested by indenting a surface perpendicular to the dealloying direction and parallel to the original sample surface (purple) and areas with different ligament sizes in the cross section parallel to the dealloying direction (blue, green) with a comparison to a non-silicide-containing control samples (hardness in gray) showing strength and anisotropy enhanced by the presence of silicide.

indentations were made in the direction of plate growth. By applying this method to other material systems, a variety of anisotropic properties can be engineered in LMD composites via formation of secondary phases during dealloying. Some candidates include carbides or borides for enhanced strength and toughness and refractory semiconductors to add electronic properties to the composite. The performance of capacitors is well understood, so the path towards commercialization for this application is known to require maximizing surface area and minimizing defects in the dielectric layer to improve device performance while also streamlining the LMD manufacturing process to provide cost-effective bulk porous Nb.

7.4 Dealloyed Composites for Additive Manufacturing

In **Chapter 6** we discussed forming dealloyed coatings on Ni-based alloys by LMD where a eutectic melt at the interface between coating and substrate provides the liquid phase for dealloying. This method of dealloying where all the components are solid until heating to form the final structure has promise as a method for metal additive manufacturing as well. The coating was formed using plasma spray to apply material to a surface that was reacted to form the final microstructure. This process is fundamentally additive, since the material that forms the coating was not initially present in the system. By applying alternate layers of substrate and coating alloys, a bulk material similar to the coating could be formed. However, alternately plasma spraying layers of Ti alloy and Ni alloy and heat treating would be limiting geometrically and time consuming. Instead, a similar structure can be reached stochastically by mixing two alloy powders and heat treating to cause the dealloying reaction to occur anywhere two unlike particles come into contact. The liquid phase allows the particles the mobility to densify fully, forming a solid metal composite part rapidly. Adapting this technique to more free-form additive manufacturing allows the fabrication of parts that combine the modest processing temperatures used in this coating (several hundred degrees below the melting points of any of the main constituents) with the excellent mechanical properties exhibited.

Experimental Methods: Titanium alloy-nickel alloy composites were formed by mechanically mixing alloy powders by hand and pouring the loose mixture into a cast

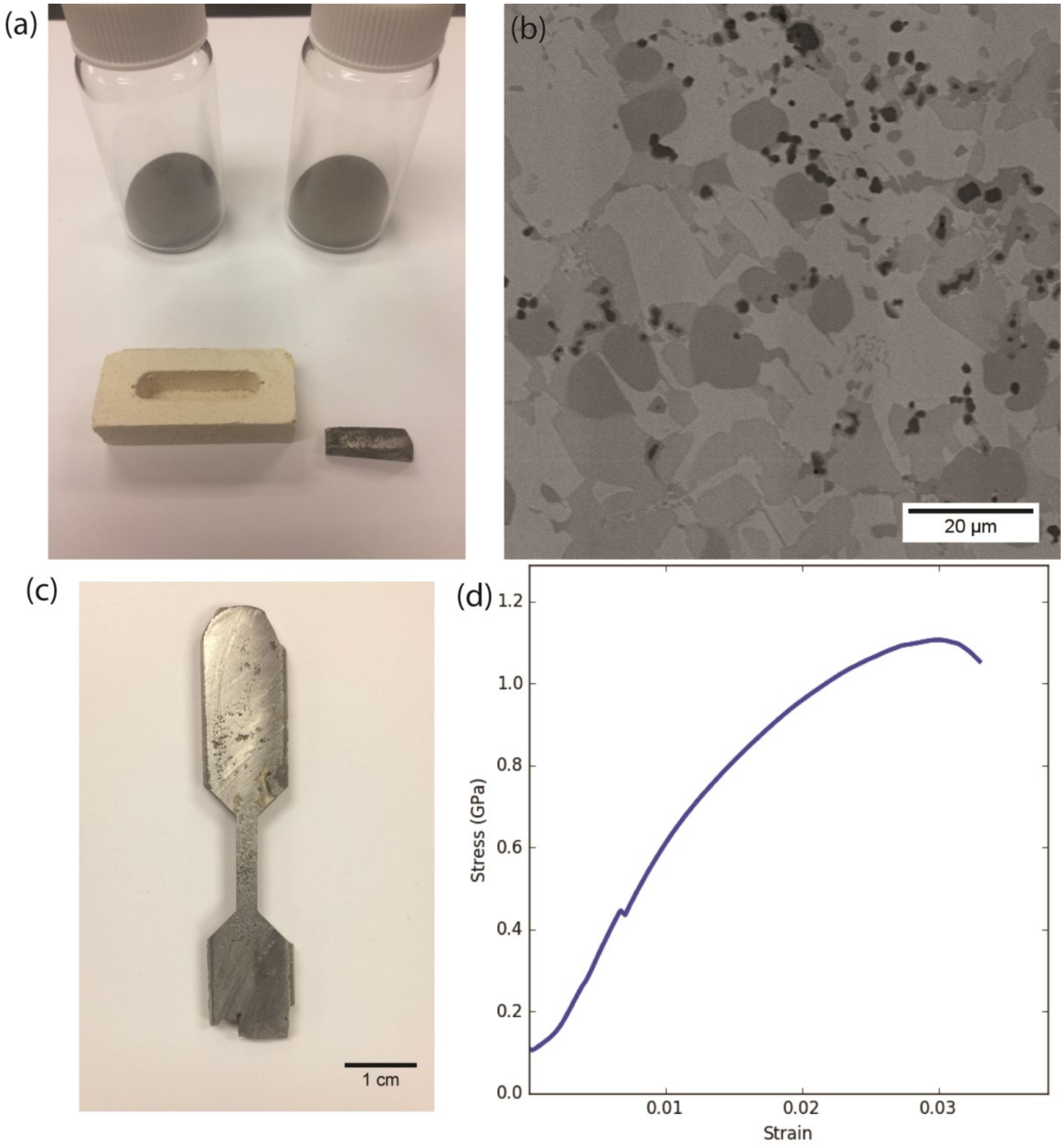

Figure 7-5: (a) Ni and Ti-Cr alloy powders and mold used to form the ingot pictured by heat treatment for 1200°C for 4 minutes. (b) Backscattered SEM image showing up to four major phases present. (c) Tensile testing sample cut from a larger reacted powder ingot using electrical discharge machining. (d) Stress-strain curve of a section of the same sample undergoing uniaxial compression, showing yielding and significant plastic deformation.

zirconia ceramic crucible. The crucible was placed into a controlled-atmosphere furnace and purged with Ar for 30 minutes, before heating rapidly to a setpoint of 1200 °C. Timing began when the furnace temperature passed 1150°C, the temperature where the reaction was known to begin. After the specified time, the power to the furnace was interrupted and the sample was removed to cool in air.

All samples were polished using methods described previously (see Experimental Methods in **Chapter 2**) and examined optically and using a JEOL JSM-6700F field emission scanning electron microscope (SEM) equipped with energy dispersive x-ray spectroscopy (EDS) and annular backscattered electron detectors.

Results and Discussion: One of the greatest challenges in metal additive manufacturing is the full densification of additive parts. For this system to densify fully, one of the starting powders must fully melt, or nearly fully melt, so the remaining solid components are able to move freely. In order to provide this freedom of motion, the nickel substrate alloy from **Chapter 6** was replaced with pure nickel powder (which was also more readily available). The Ni powder was mixed at equal mass with the same $Ti_{55}Cr_{45}$ alloy powder used for plasma spray. The powder mixture was poured into a cast zirconium oxide mold and heated at 1150 °C for 4 minutes in an argon atmosphere. Due to experimental limitations, the sample was then removed from the furnace and allowed to cool naturally in air. The result was a fully dense alloy composite ingot with the same phase behavior as the coating above. **Figure 7-5** shows a picture of the materials and the resulting composite sample, with visible oxide scale formed during cooling. An SEM micrograph of the cross section shows the same variety of phases present as in the coating, although in this case the microstructural length scale is much larger. Without the W and Mo from the coating alloy system, there is a smaller fraction of high melting point components, which acts to slow the coarsening of the structure while molten. Due to the greater Ni content in this system, the phase abundance changes somewhat, with the sample dominated by Ni-rich intermetallic domains and including smaller fractions of Cr and Ti-rich domains, in addition to small areas of almost pure Ti (the darkest phase visible in the SEM micrograph in **Figure 7-5**). However, the material retains impressive hardness, with Vickers indentation giving values up to 7.8 GPa (800 HV). Since these samples can be formed into any shape, a tensile bar was cast to measure the bulk mechanical properties more directly. However, it failed during setup before such a measurement could be made. Nevertheless, bulk compression tests were undertaken which are less sensitive to imperfections in the sample. A representative compression curve is shown in **Figure 7-5**, with an ultimate stress of more than 1 GPa measured, and 3% plastic strain before failure.

Metal additive manufacturing is still a developing field, with significant research effort going into expanding the catalog of metals and alloys compatible with additive technologies. This work demonstrates a different approach to the problem, designing the metal system specifically for additive manufacturing rather than adapting an existing formulation. By taking advantage of the local heating associated with additive manufacturing, the shape of the part and the complex composite microstructure form simultaneously. In addition to avoiding additional post-treatment steps to improve the properties, the use of a eutectic liquid lowers the required temperature for the additive process, from 1500 °C for Ni alloys and up to 1700 °C for Ti alloys down to less than 1200 °C for the composite system demonstrated here, while maintaining benefits including low density, high strength, and corrosion resistance.

7.5 Conclusions and Future Work

The international dealloying community continues to grow, with a recent MRS Bulletin issue highlighting advances and opportunities in the field of dealloying [13]. However, dealloyed materials remain confined to the laboratory because their unique properties are viewed as convenient model systems rather than opportunities for widespread application. The rapid reaction rates and stability of LMD materials makes them ideal candidates for commercial viability among the various materials dealloyed by other methods over the past several decades.

Liquid metal dealloying is a fascinating process where a homogeneous volume of material gains features with specific length scale and composition due to the interaction between thermodynamic driving forces and rate kinetics in both solid and liquid phases, and most importantly at the interface between solid and liquid. In this thesis, we have discussed several of these processes in depth, highlighting the morphological effects of solid and liquid composition as well as the unique complex composites that can be formed by understanding the liquid phase diffusion that governs the dealloying rate. Above, we have we have mentioned a few areas of opportunity for LMD materials to contribute to established or emerging technologies, as well as discussing new experimental spaces for LMD materials in semiconductor materials and shape and surface control.

To make the most of the work done by generations of researchers to understand the nuances of dealloying and dealloyed materials, the areas where dealloyed materials can have the greatest impact must be identified and pursued. I hope that the fundamental work here can serve as a platform for a new generation of multifunctional materials that take full advantage of the unique characteristics of liquid metal dealloying.

7.6 References

[1] T. Wada, J. Yamada, H. Kato, Preparation of three-dimensional nanoporous Si using dealloying by metallic melt and application as a lithium-ion rechargeable battery negative electrode, J. Power Sources. 306 (2016) 8–16. doi:10.1016/j.jpowsour.2015.11.079.

[2] T. Wada, T. Ichitsubo, K. Yubuta, H. Segawa, H. Yoshida, H. Kato, Bulk-nanoporous-silicon negative electrode with extremely high cyclability for lithium-ion batteries prepared using a top-down process, Nano Lett. 14 (2014) 4505–4510. doi:10.1021/nl501500g.

[3] B.T. Richards, B. Gaskey, B.D.A. Levin, K. Whitham, D. Muller, T. Hanrath, Direct growth of germanium and silicon nanowires on metal films, J. Mater. Chem. C. 2 (2014) 1869. doi:10.1039/c3tc31666a.

[4] D.J. Eaglesham, A.E. White, L.C. Feldman, N. Moriya, D.C. Jacobson, Equilibrium shape of Si, Phys. Rev. Lett. 70 (1993) 1643.

[5] W.W. Mullins, G.S. Rohrer, Nucleation barrier for volume-conserving shape changes of faceted crystals, J. Am. Ceram. Soc. 83 (2000) 214–216. doi:DOI 10.1111/j.1151-2916.2000.tb01173.x.

[6] T. Yano, N. Oishi, A. Komatsu, K. Koyama, Tantalum powder for sintered capacitors, (1972).

[7] N.F. Jackson, J.C. Hendy, The Use of Niobium as an Anode Material in Liquid Filled Electrolytic Capacitors, Electrocompon. Sci. Technol. 1 (1974) 27–37. doi:10.1155/APEC.1.27.

[8] J.W. Kim, T. Wada, S.G. Kim, H. Kato, Sub-micron porous niobium solid

electrolytic capacitor prepared by dealloying in a metallic melt, Mater. Lett. 116 (2014) 223–226. doi:10.1016/j.matlet.2013.11.036.

[9] A. Misra, J.P. Hirth, R.G. Hoagland, Length-scale-dependent deformation mechanisms in incoherent metallic multilayered composites, Acta Mater. 53 (2005) 4817–4824. doi:10.1016/j.actamat.2005.06.025.

[10] I. McCue, S. Ryan, K. Hemker, X. Xu, N. Li, M. Chen, J. Erlebacher, Size Effects in the Mechanical Properties of Bulk Bicontinuous Ta/Cu Nanocomposites Made by Liquid Metal Dealloying, Adv. Eng. Mater. 18 (2016) 46–50. doi:10.1002/adem.201500219.

[11] I. McCue, B. Gaskey, B. Crawford, J. Erlebacher, Local heterogeneity in the mechanical properties of bicontinuous composites made by liquid metal dealloying, Appl. Phys. Lett. 109 (2016). doi:10.1063/1.4971776.

[12] N.S. Stoloff, C.T. Liu, S.C. Deevi, Emerging applications of intermetallics, Intermetallics. 8 (2000) 1313–1320. doi:10.1016/S0966-9795(00)00077-7.

[13] J. Weissmüller, K. Sieradzki, Dealloyed nanoporous materials with interface-controlled behavior, MRS Bull. 43 (2018) 14–19. doi:10.1557/mrs.2017.299.

Curriculum Vitae

Bernard Gaskey was born in Pennsylvania, USA. *August 1991*

Education

Master of Science *August 2015*
Johns Hopkins University, Department of Materials Science and Engineering

Bachelor of Science *cum laude* *May 2013*
Cornell University, Department of Chemical and Biomolecular Engineering

Awards

Donald S. Rodbell Graduate Student Award	*September 2015*
Paul V. Renoff Fellowship	*September 2013*
Cornell Engineering Dean's List (x6)	*May 2013*
Arkema Inc. Foundation Scholarship	*May 2009*

Research Experience

Graduate Resarch Assistant – Erlebacher Group *September 2013-present*
Johns Hopkins University, Department of Materials Science and Engineering

Microscopy Intern – Analytical Group *June 2013- September 2013*
Arkema, King of Prussia, PA

Undergraduate Research Assistant – Hanrath Group *January 2011-May 2013*
Cornell University, Department of Chemical and Biomolecular Engineering

Chemical Lab and Operations Engineering Intern June 2010-August 2011
AE Polysilicon, Fairless Hills, PA

Publications

Benn, E., **Gaskey, B.**, & Erlebacher, J. (2017). Suppression of Hydrogen Evolution by Oxygen Reduction in Nanoporous Electrocatalysts. *Journal of the American Chemical Society*.

McCue, I., **Gaskey, B.**, Crawford, B., & Erlebacher, J. (2016). “Local heterogeneity in the mechanical properties of bicontinuous composites made by liquid metal dealloying.” *Applied Physics Letters*, *109*, 231901.

McCue, I., **Gaskey, B.**, Geslin, P. A., Karma, A., & Erlebacher, J. (2016). “Kinetics and morphological evolution of liquid metal dealloying.” *Acta Materialia*, *115*, 10-23.

McCue, I., Benn, E., **Gaskey, B.**, & Erlebacher, J. (2016). “Dealloying and Dealloyed Materials.” *Annual Review of Materials Research*, 46, 263-286.

Geslin, P. A., McCue, I., **Gaskey, B.**, Erlebacher, J., & Karma, A. (2015). “Topology-generating interfacial pattern formation during liquid metal dealloying.” *Nature Communications*, 6.

Richards, B. T., **Gaskey, B.**, Levin, B. D., Whitham, K., Muller, D., & Hanrath, T. (2014). “Direct growth of germanium and silicon nanowires on metal films.” *Journal of Materials Chemistry C*, 2(10), 1869-1878.

Moore, D. T., **Gaskey, B.**, Robbins, A., & Hanrath, T. (2014). “A detailed balance analysis of conversion efficiencies limits for nanocrystal solar cells— Relating the shape of the excitonic peak to conversion efficiencies.” *Journal of Applied Physics*, 115(5), 054313.

Patents

Erlebacher, J. and **Gaskey, B.**, Johns Hopkins University, 2017. “Method of carbon dioxide-free hydrogen production from hydrocarbon decomposition over metal salts.” U.S. Patent 9,776,860.

Presentations

Presenting authors underlined.

B. Gaskey, J. Erlebacher. “Silicide-strengthened Composites Fabricated via Liquid Metal Dealloying.” *Physical Metallurgy Gordon Research Conference*. Biddeford, Maine. 24 July 2017. Poster.

B. Gaskey, I. McCue, J. Erlebacher. “Functional Composites by Liquid Metal Dealloying.” *Materials Research Society Fall Meeting*. Boston, Massachusetts. 2 December 2016.

B. Gaskey, I. McCue, M. Brupbacher, J. Erlebacher. “Self-Organized Bicontinuous Intermetallic Coatings.” *Materials Research Society Fall Meeting*. Boston, Massachusetts. 1 December 2016.

B. Gaskey, I. McCue, J. Erlebacher. “Anomalous Faceting in the Dealloying of Silicon Alloys.” *Second International Symposium on Nanoporous Materials by Alloy Corrosion*. Lake Bostal, Germany. 26 September 2016.

B. Gaskey, J. Erlebacher. “Fabricating Next-Generation Dealloyed Materials.” Johns Hopkins University Department of Materials Science and Engineering. Baltimore, Maryland. 14 September 2016.

I. McCue, **B. Gaskey**, B. Crawford, S. Ryan, K. Hemker, J. Erlebacher, “Bulk Bicontinuous Ta/Cu Nanocomposites Made by Liquid Metal Dealloying: Structure and Mechanical Properties.” *Materials Research Society Fall Meeting*. Boston, Massachusetts. 2 December 2015.

I. McCue, **B. Gaskey**, P.-A. Geslin, A. Karma, J. Erlebacher, “Kinetics of Morphological Evolution during Liquid Metal Dealloying” *Materials Research Society Fall Meeting*. Boston, Massachusetts. 2 December 2015.

G. Moeller, **B. Gaskey**, W. Wu. “Scratch Visibility Analysis of Polymer Samples with an Optical Microscope.” *ANTEC 2014*. Las Vegas, Nevada. 28 April 2014.

B. Richards, **B. Gaskey**, K. Whitham, T. Hanrath. “Scalable Solar Cell Architectures Comprised of Germanium Nanowires Sensitized by Lead Salt Nanocrystals.” *Materials Research Society Fall Meeting*. Boston, Massachusetts. 26 November 2012. Poster.

T. Hanrath, B. Richards, **B. Gaskey**. “Growth of Nanowires On Bulk Metal Foils: Opportunities and Challenges towards High-Throughput, Catalyst-Free Nanowire Production.” *American Institute of Chemical Engineers Annual Meeting*. Pittsburgh, Pennsylvania. 1 November 2012.